Movement strategies of a multi-mode bacterial swimmer

Zahra Alirezaeizanjani

Dissertation
zur Erlangung des akademischen Grades,
“doctor rerum naturalium”
(Dr. rer. nat.)
in der Wissenschaftsdisziplin
Zellbiologie

eingereicht an der
Mathematisch-Naturwissenschaftlichen Fakultät
Institut für Biochemie und Biologie
Universität Potsdam

Potsdam,
13.08.2020

Hauptbetreuer:	Prof. Dr. Carsten Beta
Weitere Gutachter:	Prof. Dr. Damien Faivre
	Prof. Dr. Stefan Klumpp

https://doi.org/10.25932/publishup-47580
https://nbn-resolving.org/urn:nbn:de:kobv:517-opus4-475806

I would like to dedicate this thesis to my loving family …

Declaration

I hereby declare that except where specific reference is made to the work of others, the contents of this dissertation are original and have not been submitted in whole or in part for consideration for any other degree or qualification in this, or any other University. This dissertation is the result of my own work and includes nothing which is the outcome of work done in collaboration, except where specifically indicated in the text.

Zahra Alirezaeizanjani
Potsdam,
28.02.2020

Acknowledgements

During the journey of Ph.D., a great many people, including my family members, my friends, and colleagues, have contributed to accomplish this huge task. I owe thanks to a very special person, my husband, Mahdi for his endless love, support and understanding during my pursuit of Ph.D. degree, that made the completion of the thesis possible. He was (and is) always beside me during the happy and hard moments that motivated me to pursue success. I would like to express my sincere gratitude to my supervisor Carsten Beta who accepted me as his Ph.D. student and offered me his guidance and support to examine the unexplored with confidence and enthusiasm. I greatly appreciate the support received from Robert Großmann during the challenging times. Some of the findings and interpretations in this thesis would not have been obtained without his support. Special thanks are to my friend and lab-mate Veronika Pfeifer for her invaluable help for the bacterial samples preparation. I also wish to express my acknowledgment to Holger Stark and Maximilian Seyrich for the pleasant and effective collaboration and discussion. I am extremely thankful to my colleagues especially Kirsten Sachse, who bring happiness and warmness to the group. Finally, I acknowledge the people, who mean a lot to me, my parents and my sister Zohre, who were willing to support any decision I made.

Abstract

Bacteria are one of the most widespread kinds of microorganisms that play essential roles in many biological and ecological processes. Bacteria live either as independent individuals or in organized communities. At the level of single cells, interactions between bacteria, their neighbors, and the surrounding physical and chemical environment are the foundations of microbial processes. Modern microscopy imaging techniques provide attractive and promising means to study the impact of these interactions on the dynamics of bacteria. The aim of this dissertation is to deepen our understanding four fundamental bacterial processes – single-cell motility, chemotaxis, bacterial interactions with environmental constraints, and their communication with neighbors – through a live cell imaging technique. By exploring these processes, we expanded our knowledge on so far unexplained mechanisms of bacterial interactions.

Firstly, we studied the motility of the soil bacterium *Pseudomonas putida* (*P. putida*), which swims through flagella propulsion, and has a complex, multi-mode swimming tactic. It was recently reported that *P. putida* exhibits several distinct swimming modes – the flagella can push and pull the cell body or wrap around it. Using a new combined phase-contrast and fluorescence imaging set-up, the swimming mode (push, pull, or wrapped) of each run phase was automatically recorded, which provided the full swimming statistics of the multi-mode swimmer. Furthermore, the investigation of cell interactions with a solid boundary illustrated an asymmetry for the different swimming modes; in contrast to the push and pull modes, the curvature of runs in wrapped mode was not affected by the solid boundary. This finding suggested that having a multi-mode swimming strategy may provide further versatility to react to environmental constraints.

Then we determined how *P. putida* navigates toward chemoattractants, i.e. its chemotaxis strategies. We found that individual run modes show distinct chemotactic responses in nutrition gradients. In particular, *P. putida* cells exhibited an asymmetry in their chemotactic responsiveness; the wrapped mode (slow swimming mode) was affected by the chemoattractant, whereas the push mode (fast swimming mode) was not. These results can be seen as a starting point to understand more complex chemotaxis strategies of multi-mode swimmers going beyond the well-known paradigm of *Escherichia coli*, that exhibits only one swimming mode.

Finally we considered the cell dynamics in a dense population. Besides physical interactions with their neighbors, cells communicate their activities and orchestrate their population behaviors via quorum-sensing. Molecules that are secreted to the surrounding by the bacterial cells, act as signals and regulate the cell population behaviour. We studied *P. putida*'s motility in a dense population by exposing the cells to environments with different concentrations of chemical signals. We found that higher amounts of chemical signals in the surrounding influenced the single-cell behaviourr, suggesting that cell-cell communications may also affect the flagellar dynamics.

In summary, this dissertation studies the dynamics of a bacterium with a multi-mode swimming tactic and how it is affected by the surrounding environment using microscopy imaging. The detailed description of the bacterial motility in fundamental bacterial processes can provide new insights into the ecology of microorganisms.

Table of contents

List of figures

List of tables

Chapter 1

Introduction

Bacteria play prominent roles in the world, in many respects. They are remarkably diverse and live everywhere on earth, from the deepest parts of the ocean to the inside of human intestines. However, they have in common amazing properties. They are mostly single cells, and have evolved remarkable flexibility to interact with changes in physicochemical conditions. Chemical, thermal, and mechanical signals, as well as electric and magnetic fields, can be sensed by bacteria [1]. They manipulate their behavior in response to these cues and propagate all over the earth [2]. They have a wide variety of shapes and different size, from 0.5 to 4 µm in width and from 2 to 50 µm in length [3]. They also exhibit social communications through their signaling pathways inside the cells and their secreted chemicals.

Cell motility has crucial functions in a broad range of cellular activities. Most bacteria are motile and have various mechanisms to mediate motility. [4]. Bacterial swimming through flagella propulsion is one of the most widespread forms of cellular locomotion, that plays an essential role in many biological processes such as the infections spreading or formation of biofilms [2]. They propel themselves by rotating helical flagella, that are attached to their cell bodies. During continuous rotation of the flagellar motors, cells propagate in straight "runs". Any interruption of the flagella (either bundle or single flagellum) rotation harmony brings the cell into the "event", by which the cell changes its direction of motion. This interruption events can be "tumble", "stop", "reversal", or "flick". Throughout the "tumble", the flagella bundle falls apart as a result of changing motor rotation of at least one of the flagellar, e.g. peritrichous *Escherichia coli* [5]. In some bacterial species, e.g. monotrichous *Rhodobacter sphaeroides* [6], the periodic pausing of the motor rotation helps the cell to change the direction. Finally, the monotrichous *Vibrio alginolyticus* cells redirect either with “reversal” (through the reversal of the motor rotation direction), or “flick” (through the buckling instability of the flagellum hook) [7, 8].

The bacterial species of our interest *Pseudomonas putida* (*P. putida*) is a soil bacterium and has both capability to support the corps and to protect the plant from different pathogens. They degrade a wide variety of chemicals (many natural and artificial compound) in soil [9] and establish mutual relationships with the plant by feeding on root exudates and releasing siderophores, antibiotics and biosurfactants [10]. They can sense chemical gradients and respond to them using flagella or pili coupled to a chemosensory system [11]. In terms of flagellation, they have a bunch of flagella inserted the pole of cell to form a tuft [12]. The chemosensory system of *P. putida* is more complex than *E. coli*. However, the canonical chemotaxis system in *P. putida* is expected to be similar with *E. coli* [11]. One of the preliminary studies to understand the *P. putida* swimming tactic showed that the cells swam in the straight “run” and occasionally changed the swimming direction either with “turn” or “stop” [13]. Moreover, the swimming speed of the “run” phase can be altered by the factor of two on average when the cell reverses the direction of the motion [14]. Detailed observations using high-speed video microscopy of fluorescently tagged flagella revealed the significant information of the flagella dynamics [15]. Counterclockwise (CCW) rotation of the flagella establish the bundle that pushes the cell forward; clockwise (CW), it pulls it backward. Furthermore, it is revealed that the CW rotation establishes another distinct run state; wrapped mode with the covered flagella bundle around the cell body while it swims in a corkscrew motion (also found in three different bacterial species [16–18]). These features make *P. putida* a valuable model system to better understand the swimming tactic of multi-mode swimmers.

In this thesis, we capture the dynamic nature of *P. putida* with a multi-mode swimming strategy using live imaging techniques. We develop a new framework to investigate the influence of flagellar bundle configuration on fundamental processes such as cell motility, chemotaxis, and bacterial communication. We start with an introduction that gives a review of the whole biological and physical phenomena involved in the bacterial motility in general. In chapter 2, we present a review of selected contributions to advance our knowledge of the fundamental biological and physical features in bacterial motility and chemotaxis from single cells to collective motion.

In chapter 3, we explain our new established digital imaging set-up which broadly utilized to reveal the *P. putida* dynamics. Besides the economic privilege of the novel high-speed microscopy, it captures the images with adequate resolution to visualize the flagella dynamics of every single cell body displacement and reorientation. The temporal/spatial resolution of the set-up can be more beneficial for the statistical reliability of the bacterial dynamics. Moreover, the image processing techniques and the data analysis approach will be elucidated in this chapter. The imaging set-up, together with the image processing and data analyzing approaches, founded a baseline for the experimental and theoretical findings.

In chapter 4, the quantitative description of the motility pattern of *P. putida* is clarified. The noticeable aspect of this study originates in the reliable quantitative information of *P. putida* dynamics with different flagella configurations. The new established microscopy set-up enables us to reveal the full swimming statistics of a multi-mode swimmer, including the transition rates between the different run states.

In chapter 5, we present the analysis of *P. putida* swimming near the solid boundary by taking advantage of the set-up introduced in Chapter 3. We found out that the hydrodynamic interaction of bacteria with a solid boundary could influence push mode; The bacterial cells during push mode moved in a circle, close to the solid boundary. However, the wrapped flagellar bundle did not display any interaction with the surface.

In chapter 6, we display the responses of *E. coli* and *P. putida* to the gradient of nutrition. Together with my collaborators, we proposed the robust methodology to describe *E. coli* dynamics in a nutrition gradient. Furthermore, we discovered the asymmetry of the chemotaxis response of *P. putida*'s different run modes. In a joint attempt with our collaborator Robert Grossman, we developed an active particle model of multi-mode swimming to better understand the influence of this asymmetry on the chemotactic motion of the bacteria in the long-time limit.

Finally, we address the bacterial motility in the crowded environment. In this project, a detailed analysis of the population-scale swimming statistics was performed to study the influence of cell density on bacterial cell motility.

Chapter 2

General introduction

2.1 Motility by means of flagella

2.1.1 Structural features

Bacteria can swim in aqueous environments by means of the flagella. Typically each flagellum contains a complex rotary nano-machine and a passive filament of up to 10 µm length, and 40 nm diameter. The flagellum of gram-negative bacteria, e.g. *E. coli*, consists of three parts: the complex basal body, the hook, and the filament (Fig. 2.1).

The basal body is embedded in the cell wall and consists of a set of protein disks that bridges three layers of the cell envelope, termed as MS, P, and L ring [19]. The L and P rings are located within the outer membrane and the peptidoglycan layer, respectively [20, 21]. The inner-membrane spanning MS ring is made of a single protein FliF. The switch complex c-ring is located beneath of MS-ring and comprises FliG, FliM, and FliN. It is equipped with an active system to export the components of the hook and the filament structures used to assemble them [4]. This part of the basal body has a rotary motor function. The flagellar motor components are the stator (stationary element) and the rotor (rotating element). The power that drives the flagella rotation is provided by a transmembrane electrochemical gradient through the stators (MotA/MotB in Fig. 2.1). The electrochemical energy is converted into torque via the interaction of the stator and rotor. The flux of ions across the stator drive conformational changes [23, 24]. These conformational transitions induces the interactions between MotA of the stator and the rotor protein FliG [25, 26], and finally can whirl the rotor in either a counterclockwise (CCW) or clockwise (CW) direction (as seen from behind).

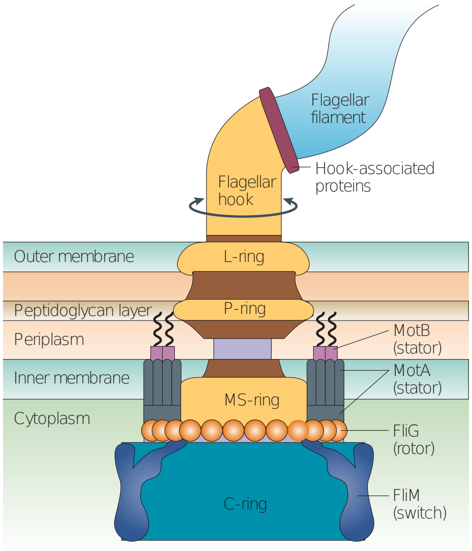

Fig. 2.1 The bacterial flagellum of *E. coli* contains three parts: a complex basal body, a hook, and a filament. Many bacteria swim through liquids by using filaments propelled by a rotary motor. The core of the motor is the basal body. The basal body spans three layers of the cell envelope: outer membrane, peptidoglycan cell wall, and cytoplasmic membrane. The proton flow through roughly eleven force-generating units (MotAB complexes) generates force to rotate the flagella. Taken from [22].

The second part of the flagellum is the hook. It is a short flexible cylindrical structure with a 50-100 nm length and ~ 20 nm thickness [27]. The specific physical properties of the hook are vital for bacteria motility. Researchers in Ref. [28] confirmed that changes in the stiffness of the *E. coli* hook caused a loss of bundle formation during swimming. Furthermore, a buckling instability of the hook is the key factor for the reorientation of monotrichous marine bacterium *Vibrio alginolyticus* [8].

The third component of the bacterial flagellum is a helical polymer filament, with $\sim$ 20 nm diameter. Both hook and filament are tubular structures made of protofilaments. The flagellar hook protein E (FlgE) and flagellin (FliC) are the bulding blocks of the hook and filament, respectively. Eleven protofilaments are self-assembled to form the tubular structures [29, 30].

2.1.2 Polymorphic transition

The flageller filament is a rigid structure but can transform between distinct polymorphic shapes [31–33]. Many factors influence the shape of the filaments such as the sequence of the flagellin, the pH, ionic strength, and torsional load [23]. The protofilaments have two conformation states, which is called L and R-types (R and L refer to the twist direction). The

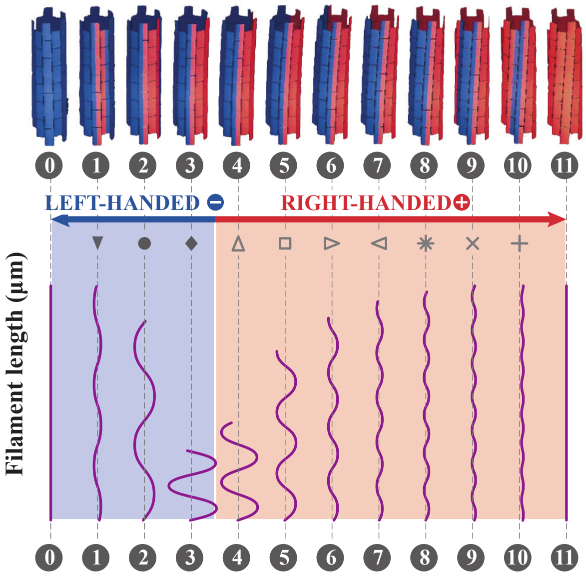

Fig. 2.2 The scheme of the 12 polymorphic shapes of bacterial flagellar filaments. Number 0 and 11 are the straight filaments. The rest of them are true helices. Among the non-straight shapes, 3 are left handed (numbers 1-3). Polymorphic number 2 is called normal filament. Of the 7 non-straight right-handed polymorphic shapes, the semicoiled (number 4), and the curly (number 5) are the polymorphic transitions while the flagella bundle is disassembled. Adapted from [34].

electron cryomicroscopy and X-ray diffraction studies of filaments indicated that there are two conformations of the filaments helix (number 0 and 11 in figure 2.2); The filaments can twist into either right-handed helix or left-handed based on the handedness of the monomer twist. They also showed that the right-handed filaments are slightly shorter than left-handed ones with 0.8 Å difference [35]. Those straight filaments are made when all of the monomers twisted into the same direction. The ratio of the left-handed and right-handed protofilaments make the various conformations. Between these two straight shapes, 10 helical filaments polymorphic states are possible which are molecularly and mechanically stable [31, 36].

The flagellar filaments of free swimming cells showed the precise dynamics of polymorphic transitions in different bacteria species. *E. coli* during the "run" state has the filaments with the "normal" polymorphic shape (number 2 in figure 2.2). Both "semicoiled" (number 4 in figure 2.2), and "curly" (number 5 in figure 2.2) are the forms in the "tumble" state. The transformation of "normal", "semicoiled", "curly", and eventually back to "normal" is more likely used by wild-type swimming bacteria [37]. The monotrichous bacterium *Rhodobacter sphaeroides* utilizes a much simpler flagellar polymorphism. As same as *E. coli*, the left-handed "normal" form is used for bacteria to swim forward. For the reorientation, bacteria switch off the motor and stop. The flagellum form the coiled conformation during a stop (number 3 in figure 2.2) [38, 39].

2.1.3 Energy source and dynamics

The flagellar motors are powered by ion flows moving from the outside to the inside of a bacterial cells. In fact, the stators in the flagellar motor act as selective ion channels. The coupling ions of the stator can vary in bacterial species. Some of the bacteria like *Vibrio* species are Na^+-driven type, and bacteria such as *E. coli* are H^+-driven type. The driving force for a single ion passing through the cytoplasmic membrane is ion-motive force (IMF). The IMF contains two components: an electric voltage and a chemical gradient across the membrane. It can be defined as:

$$IMF = V_m + k_B T/q \ln(C_i/C_o), \tag{2.1}$$

where V_m is the electrical potential (inside minus outside) which is defined as free energy per unit charge, q is the charge, C_i and C_o are internal and external concentrations of the coupling ion, respectively. With a typical physiological IMF of around $-150mV$, the free energy of a single ion passage through the cell membrane is $\sim 6\ k_B T$ [40].

As mentioned earlier, each flageller motor contains two parts, the stator and the rotor. Each rotor is surrounded by up to 11 stators units and each stator can be an independent force-generating unit [41, 42]. The ion flow across the channel causes conformational changes in the stator, which work on the rotor to drive rotation. Furthermore, the stator ring system is a highly dynamic complex and can be either incorporated into or dissociated from the rotor in response to ions concentration alternation and different levels of viscous drag [43–48]. This exchangeable ability of the stators between motors and a membrane-bound pool might regulate the motor rotation behavior.

The biochemical/physical and structural characterization of the stator is hindered by the membrane-embedded nature of it. For that reason, the detailed mechanochemical cycle of the flagellar motor mechanism is still unknown. The best biological probe candidate to understand the mechanochemical cycle of torque generation is the relationship between torque and rotational speed [49]. Measurements of this relationship have been determined in different bacterial species with smooth-swimming (CCW rotating) via various methods and over a wide range of loads [50–56]. In all these cases there is a plateau of nearly uniform torque up to particular low speeds, then a sharp shifts into a near-linear reduction in torque at high speeds [40]. The torque-speed plot for *E. coli* with only CW rotation showed quite different behavior; There is no plateau regime, motor torqued decreased linearly with speed

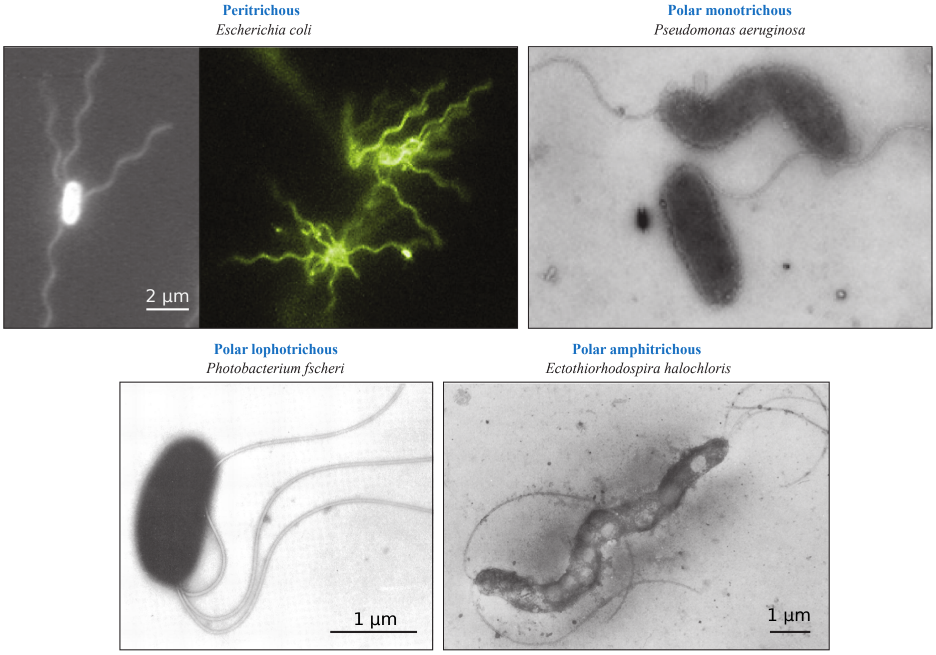

Fig. 2.3 Flagella arrangement in different bacteria species. (a) Peritrichous *Escherichia coli*. (b) Polar monotrichous *Pseudomonas aeruginosa*. (c) Polar lophotrichous *Photobacterium fischeri*. (d) Polar amphitrichous *Ectothiorhodospira halochloris*. Adapted from [34].

[57]. The researchers speculated that higher speed of the swimmer (while the motors rotate CCW) improve the ability of cells to perceive variations in local concentrations of chemicals. The torque-speed relation is a critical test of any theoretical rotational motor model.

2.1.4 Arrangement of flagella

The arrangement of the flagella on the cell body of different bacteria species is various (figure 2.3). The peritrichous bacteria are covered by multiple flagella distributed randomly at various positions on the cell body. The peritrichous flagellated *E. coli* is chosen as a model organism to study the cell motility and chemotaxis. Flagellated monotrichous bacteria possess a single flagellum at the cell pole. The lophotrichous bacteria, e.g. *P. putida*, have multiple flagella located the same spot on their body. Amphitrichous bacteria with a single flagellum on each of the two opposite ends.

2.1.5 Swimming tactics

Our understanding of bacterial locomotion has long been shaped by the knowledge on *E. coli*. The peritrichous *E. coli* have four to eight helical flagella contributed from random points on its cell body [2]. Each flagellum is powered by a bidirectional rotary motor. The swimming pattern of *E. coli* is ‘run-and-tumble”. During the “run” episode, all the flagellar motors rotate CCW (as seen from behind). Because of hydrodynamic interactions, all the flagella are assembled as a helical bundle. The flagellar bundle propels the cell body in a nearly smooth path at $\sim 30\,\mu\mathrm{m/s}$. When at least one flagellum changes its rotational direction (CCW to CW), the bundle falls apart. During this episode (also known as “tumble”), the cell changes the direction randomly. Other bacterial species have different swimming tactics rather than the classic “run- and-tumble”. The common behavior of all of the species is that they have a longer episode, a “run”, which bacteria swim relatively long in a smooth path. The “run” episode is interrupted by the short unstable phase, an “event”, that makes the cell to randomly choose a new direction to explore better the environment. The monotrichous *V. alginolyticus* has two sets of events: The first “event”, reversal, is the result of changing the rotation direction of the flagellum motor. When the flagellum rotates CCW, it pushes the cell body forward. In contrast, if the motor rotation direction changes to CW, the flagellum pulls the cell body backward. The reorientation angle for the reversal is around $\sim 180°$. The second “event” is called flick. Bacteria in the forward swimming reorient roughly $\sim 90°$ through a buckling instability of the flagellum hook [7, 8]. But this is not the same for all of the bacteria with monotrichous flagellation. The monotrichous *Rhodobacter sphaeroides* represents another motility tactic. During the “run” state of *Rhodobacter sphaeroides*, the flagellum rotates CW and drives the cell forward. The runs are interrupted by periodic motor stops. Rotational diffusion during the stop event serves as a mechanism of reorientation. In this phase, the flagellum filament also displays polymorphism (forms a relaxed coiled shape) [6].

2.2 Life at low Reynolds number

2.2.1 Swimming at low Reynolds number

The microorganisms, such as bacteria, encounter some constraints when swimming in the aqueous environment. The behavior of bacteria in the water is affected by those physical constraints. The most important of the constraints are imposed by the laws of low Reynolds number flows [58]. Swimming movement involves the interaction between the body of the swimmer and the induced flow in the environment. To bacteria, water appears as a laminar flow with sever viscous drag many orders of magnitude stronger than inertial force. In fact, bacteria are dealing with fluids in the low Reynolds number regime. The Reynolds number of a particle moving at the velocity of v through a fluid is defined by the ratio of two expressions; the inertial forces and the viscous forces. It is defined as a single dimensionless scaling parameter

$$Re = \frac{\text{inertial force}}{\text{viscous force}} = \frac{Lv\rho}{\eta}, \tag{2.2}$$

where L is the size of particle, ρ is the density of fluid, and η is its dynamic viscosity. To understand this number better, if we try to swim through honey, we will experience a Reynolds number of $Re \sim 10^{-3}$ while bacteria may feel $Re \sim 10^{-5}$ when they swim through water [59].

For small Reynolds numbers $Re < 1$, the Stokes equation describes the characteristics of the flow regime,

$$\nabla p = \eta \nabla^2 U, \tag{2.3}$$

when U is the velocity vector field, and p is the pressure scalar field.

Since inertia is absent at low Reynolds number, any non-zero resultant force acting on an object gives rise to infinite acceleration. Accordingly, the total net force and torque will be at all times zero. For a freely swimming *E. coli*, the thrust generated by the helical flagella balances the viscous drag of the cell. Also the torque applied by the flagellar motors on the filaments is balanced by the counter-rotation of the cell body. As soon as the driving force stops, this condition enforces the cell to decelerate immediately and brings it to a stop. Another interpretation of the Reynolds number is the ratio of the hydrodynamic relaxation time $\tau_{relax} \sim L^2\rho/\eta$ and the time required to travel the distance L, $\tau_{transl} \sim L/v$. This ratio also produces the equation 2.2. For an *E. coli* of size 1 µs swimming through water at a speed of $10\,\mu\text{m/s}$, $\tau_{relax} = 1\,\mu\text{s}$, and $\tau_{transl} = 0.1\,\text{s}$. Imagine *E. coli* stops swimming; it will then decelerate according to Newton's law in $0.1\,\mu\text{s}$ and eventually stops. In the other way, a fluid element needs $0.1\,\mu\text{s}$ to be in mechanical equilibrium with its surrounding and bacteria reach the steady-state motion almost instantaneously.

The time-reversibility of flows, which are described by the time-independent Stokes equation, is another feature of the low Reynolds number regime. If a swimmer executes geometrically reciprocal motion (identical shape changes in back and forth motion) at low Reynolds number in a Newtonian fluid, the net displacement must be zero [58, 60]. In order to produce a net displacement, locomotion generally requires non-reciprocal motion. Microswimmers such as bacteria break the time-reversal symmetry using wave-like deformation of the flagella, or the rotation of helical filaments.

The flagellar propulsion is one of many tactics used by bacteria that live at low Reynolds number. Propulsion by flagellar rotation can be illustrated via resistive force theory (RFT) [62]. In this theory the motion of a single flagellum is modeled as a wave moving through a viscous fluid producing net propulsion [61, 63]. RFT basically splits the flagellum into short

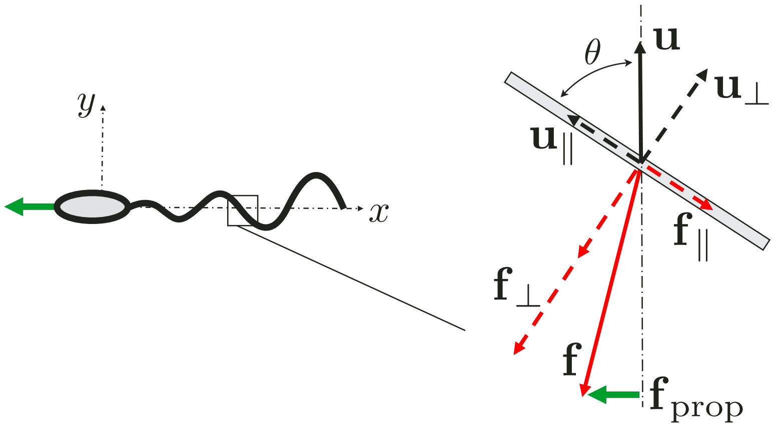

Fig. 2.4 Drag based flagellar propulsion model: based on resistive force theory, the flagellum is split into short linear segments. The individual segment is propelled with the velocity u. The rod feels local drag by the surrounding fluid. A net propulsion force is generated by means of the drag anisotropy. Taken from [61].

linear segments (2.4). Each segment moves with a velocity $\vec{u}$ at an angle θ. The velocity can be split into two components, $u_\perp = u\sin\theta$ and , $u_\| = u\cos\theta$ with $u = |\vec{u}|$. Therefore the drag per unit length components are defined as: $f_\perp = \zeta_\perp u_\perp = \zeta_\perp u \sin\theta$ and $f_\| = \zeta_\| u_\| = \zeta_\| u \cos\theta$. $\zeta_\perp$ and $\zeta_\|$ are the corresponding drag coefficients (typically $\zeta_\perp/\zeta_\| \approx 2$). This means that the viscous drag on a segment moving perpendicular to its principal axis is approximately two times larger than the one for parallel movement. The propulsive force is defined as

$$F_{prop} = 2(\zeta_\| - \zeta_\perp)u\sin\theta.\cos\theta e_x \tag{2.4}$$

In order to produce a net propulsion, both the filament velocity $\vec{u}$ and its angle θ must vary periodically in time. For instance, if $\vec{u} \to -\vec{u}$ and $\theta \to \pi - \theta$, the sign of the propulsive force is constant; in contrast, periodically changing only $\vec{u} \to -\vec{u}$ with constant θ leads to zero average force.

2.2.2 Swimming near surfaces

A physical boundary, e.g. swimming close to a solid wall, strongly affects bacterial dynamics. The boundaries induce a couple of different affects. One is changing from straight to circular motion when viewed from above the surface. This behavior was observed experimentally for the “pusher” swimmer *E. coli* [65, 66]. When the bacteria are exposed to the boundary surface from one side, they experience a net lateral drag force near the surface which induces a torque acting on the cell [64].

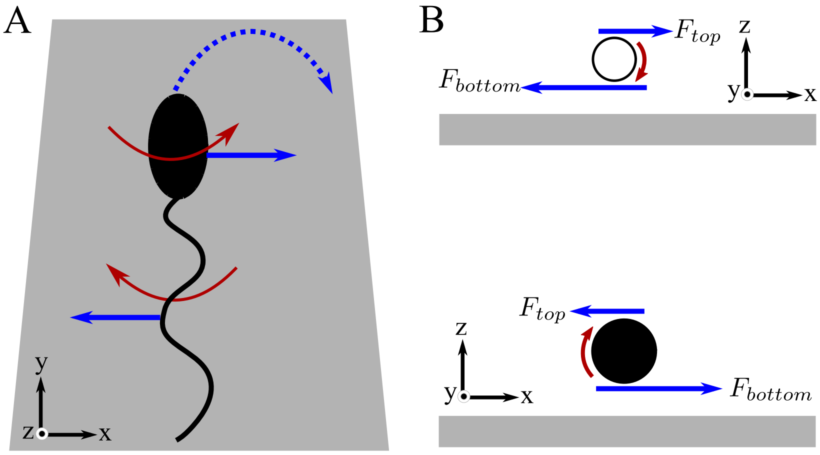

Fig. 2.5 Circular swimming of a bacterial cell near surface. (A) Hydrodynamic effects on the bacteria swimming near the surface boundary induce a torque on the cell to induce circular swimming (dashed blue arrow). The cell body and the flagellar filament rotate in opposite directions, red arrows. The flagella are subject to a force to their left and the cell body to its right, blue arrows. (B) Spatial distribution of the drag forces on the top and bottom of both cell body and flagella. Adapted from [64].

As a result of swimming near boundary surfaces, the drag force symmetry acting on the top and bottom of both flagella and cell body is broken, see Fig. 2.5B. As mentioned in section 2.2.1, flagellar propulsion is balanced by a counterrotation of the cell body (red arrows in Fig. 2.5A). The cell body experiences a hydrodynamic force at a right angle with respect to its direction of motion. In the case of *E. coli*, the cell body rotates CW. Similarly, the flagella are subject to a force in the opposite direction as the cell (blue arrows in Fig. 2.5A). The surface-induced torque is the net effect of these two forces turning the entire cell (dashed arrow in Fig. 2.5A). For *E. coli* with the right-handed helix, this causes the cell trajectories to turn CW.

2.3 Theory of active Brownian motion

The random motion of the microscopic particles was reported for the first time by Robert Brown in 1827 [67]. The theoretical descriptions of random motion, “Brownian motion”, were given by Einstein in 1905 and Smoluchowski in 1906 using a probabilistic approach [68, 69]. Later on, Langevin, in 1908, rephrased the phenomena in terms of stochastic differential equations [70]. Authors in Ref. [71] described a comprehensive review of the motion of the active particles using Brownian dynamics. When a spherical microscopic particle glides in a liquid solvent, it shows erratic movements due to thermal agitation from collisions with the surrounding fluid molecules. This random motion is called “Brownian motion", in honor of Robert Brown. Based on the Stokes-Einstein relation, the diffusion coefficient D depends on the temperature and viscosity of the fluid and the size of the particles. By tracking a spherical Brownian particle with radius R at times regularly separated by a fixed interval Δt, the translational diffusion coefficient D_t, is given by

$$D_t = \frac{k_B T}{\gamma_t}, \tag{2.5}$$

where k_B is the Boltzmann's constant, and T is temperature. $\gamma_t = 6\pi\eta R$ is the friction coefficient of the particle, where η is the viscosity of the suspending medium and R is the sphere's radius.

The Brownian particle also experiences random reorientation, which is defined by the rotational diffusion coefficient D_r:

$$D_r = \frac{k_B T}{\gamma_r}, \tag{2.6}$$

where D_r is proportional to the rotational friction coefficient $\gamma_r = 8\pi\eta R^3$.

The reason of random motions lies in the particle interactions with the fluid molecules, which are affected by the temperature. The Brownian particle experiences a force and a torque as a result of the collisions with the fluid molecules that disturb its motion (thermal noise). Langevin equations describe the translational dynamics of a particle in a fluid environment which is defined by

$$m\mathbf{a} = -\gamma\mathbf{v} + \mathbf{F}_{th}, \tag{2.7}$$

where $-\gamma\mathbf{v}$ is the viscous friction force of the fluid and $\mathbf{F}_{th}$ is the stochastic thermal force.

Since the mass of Brownian particle is small, inertia can be neglected. Indeed, the relaxation time of Brownian particle $\tau_{rel} = m/\gamma_t\mathbf{v}$, is the order of magnitude of micro-second, which is several orders of magnitude below the time intervals of images captured via a standard CMOS camera. By dropping the inertial term $m\mathbf{a}$, the Eq. 2.7 is simplified to the overdamped Langevin equation:

$$\gamma\mathbf{v} = \mathbf{F}_{th}. \tag{2.8}$$

In fact, the overdamped Langevin equation is adequate to obtain the relevant measurable physical characteristics of any system where $\Delta T \gg \tau_{rel}$.

The bacteria are active particles with the ability to propel themselves. Because of their natural habitat, aqua environment, they are subject to two forces; The viscous force that acts opposite to their velocity and the thermal noise generated by the rapid collisions of the fluid molecules around the cells. Let us consider that self-propelled particle, bacteria, with a constant speed v along a given orientation direction in 2D. The motion in two dimensions is described by a set of Langevin equation with three variables:

$$\begin{cases} \frac{d}{dt}x(t) = v\cos\theta(t) + \sqrt{2D_t}\mathbf{W_x}, \\ \frac{d}{dt}y(t) = v\sin\theta(t) + \sqrt{2D_t}\mathbf{W_y}, \\ \frac{d}{dt}\theta(t) = \theta + \sqrt{2D_r}\mathbf{W}_\theta, \\ \end{cases} \tag{2.9}$$

where $\mathbf{W_x}$, $\mathbf{W_y}$, and $\mathbf{W}_\theta$ indicate independent Gaussian white noise processes. In fact, these stochastic differential equations describe the dynamics of microorganisms.

In order to describe the microscopic system characteristic in 2D motion, one quantity is the mean square displacement (MSD)

$$\mathrm{MSD}(t) = \left\langle (x(t_1+t) - x(t_1))^2 + (y(t_1+t) - y(t_1))^2 \right\rangle, \tag{2.10}$$

the $\left\langle ... \right\rangle$ indicates averages over all initial times t and the possible trajectories. The MSD provides a lot of insights about the dynamics of a system. In fact, the MSD $\sim t^\alpha$ where α is the anomaly parameter. For $\alpha = 1$ the underlying process corresponds to a pure diffusion [72]. The process is called subdiffusive when $\alpha < 1$ or superdiffusive when $\alpha > 1$.

The trajectory of an active Brownian particle govered by Eq. 2.9 has the MSD of

$$\mathrm{MSD}(t) = \left(4D_\mathrm{t} + v^2 t_\mathrm{r}\right) t + \frac{v^2 t_\mathrm{r}^2}{2}\left(e^{-\frac{2t}{t_\mathrm{r}}} - 1\right), \tag{2.11}$$

where $t_\mathrm{r} = 1/D_\mathrm{r}$ is the time scale for the rotational diffusion. This formula describes the transition from the ballistic regime to the diffusive regime. From Eq. 2.11, when the $t \gg t_\mathrm{r}$, the particle motion is diffusive with $\mathrm{MSD}(t) \propto t$. For $t \ll t_\mathrm{r}$, the particle motion is superdiffusive (ballistic) with $\mathrm{MSD}(t) \propto v^2 t^2$.

2.4 Chemotaxis and its implications

Another aspect of the bacterial world is to detect and process external signals from the environment with their unique internal signaling pathways. When bacteria swim in a gradient of nutrition, their strategy to reach the desirable region (or run away from the toxins) is a biased random walk, employing a temporal comparison of chemical concentrations. Essentially, the rate of reorientation is modulated to reach a desirable place. This phenomenon

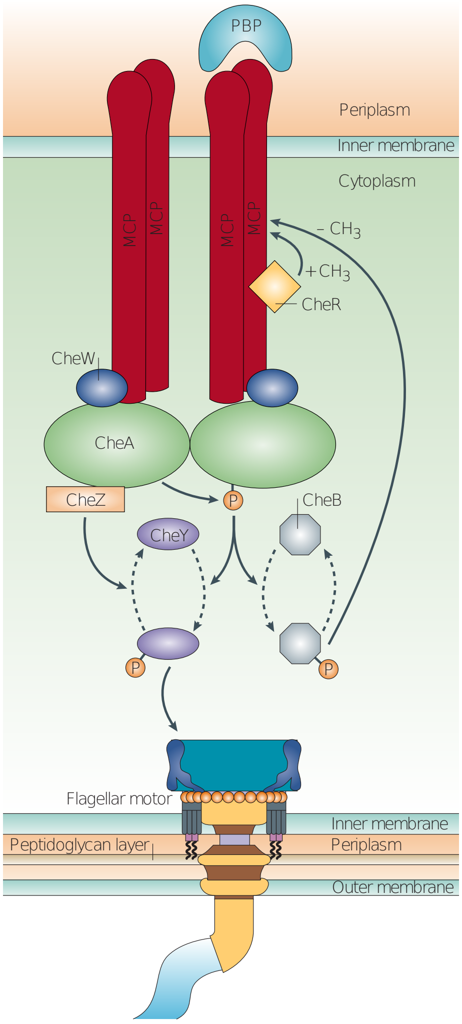

Fig. 2.6 Two dimeric MCPs are attached to the transduction units (CheA, and CheW). A decrease in attractant concentration leads to autophosphorylation of the CheA. CheA-P transfers the phosphate group either to the CheY or CheB. CheY-P diffuses in the cell and finally interacts with the flagellar motor. The interaction increases the probability of the switching to CW flagellar rotation to bring about a change in direction. CheZ dephosphorylates the CheY-P and makes the CW rotation of the flagella short enough. Meanwhile CheA-P also phosphorylates the methylesterase CheB. CheB-P compets with a CheR methyltransferase to controll the degree of methylation of glutamates in the MCPs. Taken from [22].

is called chemotaxis. The process is based on coupled flagellar rotation and the chemosensory system inside of the bacterial cell (Fig. 2.6).

2.4.1 Signaling pathways

The chemotaxis pathway of *E. coli* is a sensitive system that contains 4 units: sensor unit, transduction unit, actuator unit, and integral feedback unit [11, 22, 73].

- The sensor unit (also known as methyl-accepting chemotaxis proteins (MCPs)) is the stimuli detector in bacteria. The number of MCPs varies among bacterial species. For instance, *E. coli* has four of these MCPs while, *Pseudomonas* species have more than 25 MCPs encoded in their genomes. The MCPs contain three operational modules: transmembrane sensing module, signal conversion module, and kinase control module.
- The hub of the transduction unit in *E. coli* is a complex composed of a histidine kinase (CheA), an adaptor protein (CheW), and the kinase control module of MCPs. The transduction unit ensures modulation of CheA autokinase activity in response to ligand binding.
- The actuator module changes motor rotation through binding of a phosphorylated response regulator (CheY).
- The integral feedback unit with two enzymes (CheR, and CheB) resets the receptor signaling state to its pre-stimulus level.

A set of chemicals binds directly to the sensor unit. The information transmits across the cytoplasmic membrane and converts to a signal. That triggers the signaling pathway which directs the cell locomotion by regulating the rotational direction of the flagellar motor (Fig. 2.7). In the absence of chemoattractant, the motor shifts the equilibrium in favor of CW rotation. A specific sequence of events is involved to change the flagellar rotation:

(a) Decreasing of the chemical stimulus concentration leads to reducing the probability of binding the chemoattractant to the MCPs,

(b) Activation of CheA trans-autophosphorylation as a result of step (a) (first autophosphorylates and then transfers its phosphoryl group),

(c) Flux of CheA phosphoryl groups modulates two response regulators, CheY and CheB.

(d) The CheY-P diffuses in the cell and eventually interacts with the protein FliM, a component of the flagellar switch complex.

(e) The interaction enhances the probability of clockwise (CW) rotation, which causes random reorientation.

This signal should not be available for a long time (the mean duration of tumbles in *E. coli* is about 0.1 s). Therefore, CheY-P can be dephosphorylated vi the phosphatase CheZ quickly. The phosphatase CheZ ensures a short duration in CW rotation so that CheY-P levels closely reflect CheA activity. Decreasing the chemoattractant concentration is not the only way to enhance CheA autophosphorylation activation. The CheA autophosphorylation is induced by MCP methylation as well. The CheB-P results in an increased demethylation of the MCPs. Eventually, demethylated MCPs have a lower capability to CheA autophosphorylation so that the system adapts to the new chemoattractant concentration. With increasing the chemoattractant concentration, autophosphorylation of CheA is inhibited. Thus, CheY–P concentration is reduced, and therefore flagellar CCW rotation is firmly preferred.

Swimming of the bacteria up the gradient of chemoattractant requires a primitive type of memory to modify their behavior accordingly, to either remain in the swimming path or to reorient [75, 76]. The adaptation system provides the memory, which is a combination of several specific glutamyl residues on the kinase control module of MCPs, methyltransferase CheR, and methylesterase CheB. CheR is always active and is responsible for methylation of glutamyl residues. CheB is only active when phosphorylated by CheA and responsible for removing the methyl group. CheR preferentially enhances receptor activity by methylation, whereas CheB preferentially diminishes their activity. Besides, the CheA-mediated phosphorylation of CheB increases its methylesterase activity. In isotropic medium, these two feedbacks enable the system to adapt to the environment stimulation. The kinase activity of MCPs is adjusted to produce intermediate levels of CheY-P. The intermediate level of CheY-P generates a random sequence of runs and tumbles and allows the bacteria a random exploration of the environment. Increased attractant binding to receptors inhibits CheA activity and the concentration of CheY-P decreases. As a result, the bacteria swim in a favorable direction for a longer time. Changes in the rate of receptor methylation occur slower than the phosphorylation–dephosphorylation steps. This delay in adaptation functions as a memory. Finally, CheR resets the kinase activity back to the ground state after stimulation [77].

2.4.2 Gradient sensing

The microorganisms can adopt two strategies to sense the gradients of a chemical attractant/repellent: temporal and spatial sensing. The spatial sensing is the measurement of a spatial gradient directly across the cell extension, which allows the cell to turn in the appropriate direction. It is commonly assumed that bacteria are too small to exhibit spatial

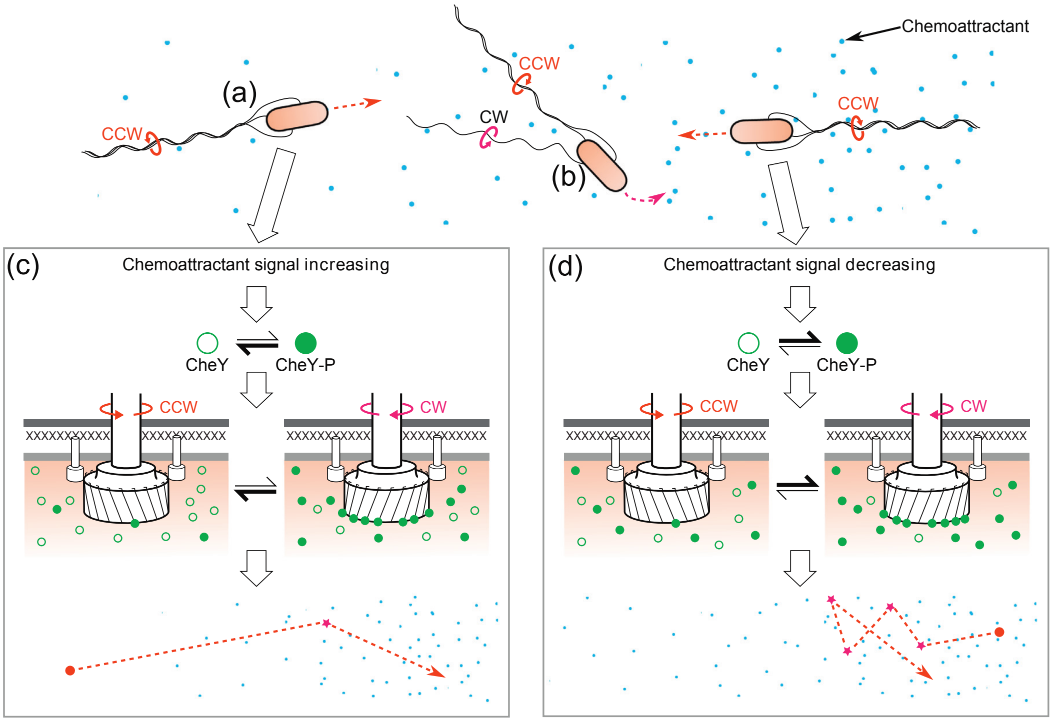

Fig. 2.7 Motor rotation and chemotaxis. The well-known bacteria *E. coli* has a "run-and-tumble" swimming strategy. (a) When all of the flagella rotate CCW in the "run" mode, the flagellar bundle propels the cell. (b) If at least one of the flagellar rotate CW, the cell tumbles and reorients randomly. (d,c) CheY-P controls the falgellar motor switching: (d) swimming downward the chemoattractant increases the probability of the CheY-P interaction with the motor because of the deficiency in the chemoattractant. The cell makes more tumbles to change the direction. (c) Swimming toward the gradient increases binding of chemoattractant to MCPs which suppresses the phosphorylation of CheY. The cells prolong runs to navigate towards higher amounts of chemoattractant. Taken from [74].

sensing of a chemical [80, 81]. In temporal sensing, the cell compares the intensity of the receptor signal at different times along its swimming track and modulates the probability of changing its direction.

E. coli analyses concentration measurements using temporal sensing and produces run-biasing decisions (longer runs toward the favourable direction). The chemotactic response function $K(t)$ quantitatively describes how bacteria make the comparison process. The experimental measurement of the chemotacic response function was done in Ref. [78] (Fig. 2.8). The single flagellum of cells had been attached to the substance. The cells were exposed to a short chemoattractant (aspartate) pulse applied at $t = 0$. The chemotactic response, obtained by measuring the fraction of time that the motors spins CCW, was probed over time. At $t = 0$, $K(t)$ approached to the maximum response within about 0.2 s, returns to

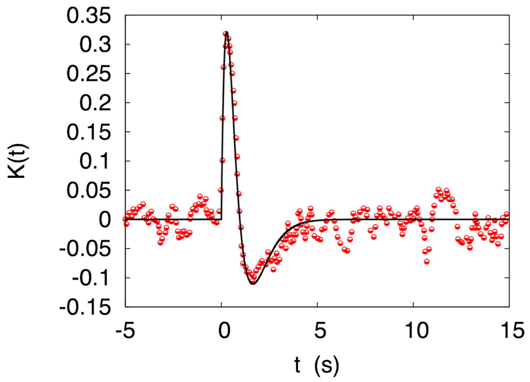

Fig. 2.8 The experimental chemotactic response function $K(t)$ to attractant (aspartate) measured using the tethered cells [78]. $K(t)$ was determined by measuring the bias of the fraction of time that a flagellum rotated CCW, averaged over several cells. The cells were exposed to a chemoattractant pulse applied at the time 0 s. They showed an instant response, then adapted to the signal within 3 s. The response gradually returned to the default levels with constant chemoattractant concentration background. Taken from [79].

the baseline within about 1 s, and remains below the baseline for 3 s (adaptation). Finally the response relaxes to the baseline, which indicates that the cell loses the memory of the past chemoattractant concentration. The experiment showed that the short-term memory of 4 s is used by cells to determine the level of chemoattractant experienced in the recent past. The response function curve has a universal feature, which is that the positive and negative lobes of response have equal areas; the integral of the response function is close to zero, i.e., $\int_0^\infty K(t)dt \approx 0$.

2.4.3 Model of chemotaxis

The experimental response function sets the stage for a couple of models to describe the biased random walk in a non-uniform distribution of chemoattractants [79, 82–86]. The models describe the chemotaxis in terms of modified mean run time as a result of chemoattractant concentration previously sensed. One can suppose the cell changes the mean run time τ linearly in response to the chemoattractant, according to

$$\tau = \tau_0(1 - Q(t)), \tag{2.12}$$

where τ_0 is the mean run time in the absence of chemoattractants. The memory of the cell is determined by the bias term Q. Mathematical models use a kernel representation of Q

$$Q(t) = \int_\infty^t K(t-t'), c(t')dt' \tag{2.13}$$

where $c(t')$ is the chemoattractant concentration experienced by the cell at time t' along its past trajectory, and $K(t)$ is the cell's response function which has a two-lobe shape with equal areas, i.e. zero integral function. These properties of $K(t)$ are consistent with the experimental curve (Fig. 2.8).

2.5 Collective motion

In most natural environments, bacterial cells construct architecturally complicated communities known as biofilms. The biofilms are surface associated structures with extracellular polymeric substance (EPS) scaffold. The biofilm development is a multi-stage process that is controlled by multiple genetic pathways [87, 88]. These stages have been classified as (i) planktonic, (ii) early attachment, (iii) microcolony formation, (iv) biofilm maturation, and (v) detachment and return to the planktonic mode. The free swimmers explore the environment in planktonic phase. The cell-surface interaction initiates with a weak contact to the surface (reversible stage), which is followed by a more stable surface association (irreversible stage). Besides the chemical molecules involved in the cell attachment, a variety of bacterial surface structures may engage in this process, e.g. flagella , pili and lipopolysaccharides. The attached cells divide and create microcolonies. Afterward, further adaptation is essential for bacteria to adjust themselves to the dictated circumstances by the biofilm. During the maturation phase, the surface-attached bacterial cells achieve two main properties, increasing

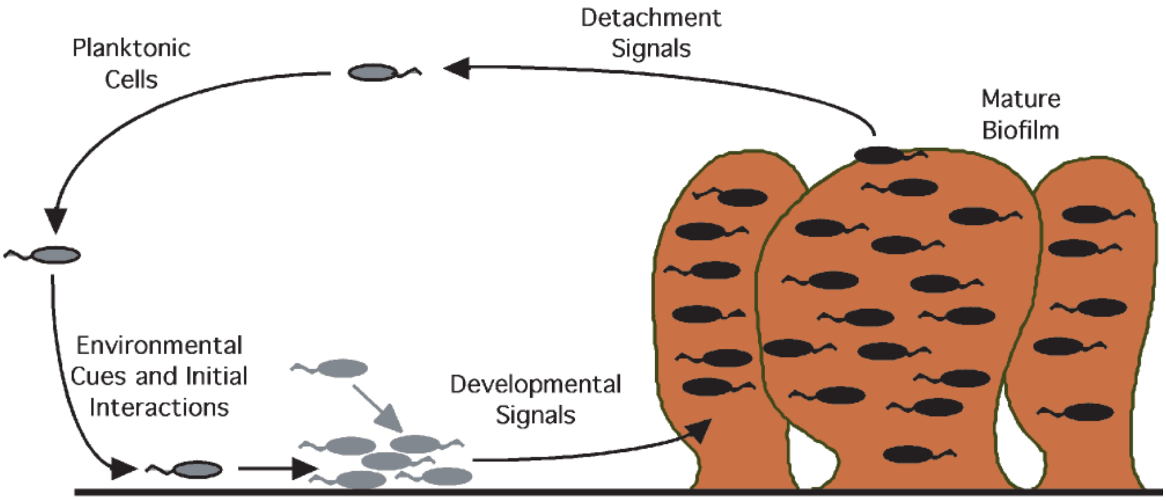

Fig. 2.9 Scheme of biofilm development. Five stages have been operationally identified in biofilm development as (i) planktonic, (ii) solid surface attachment, (iii) microcolony formation, (iv) colony maturation and (v) dispersal. Adapted from [87].

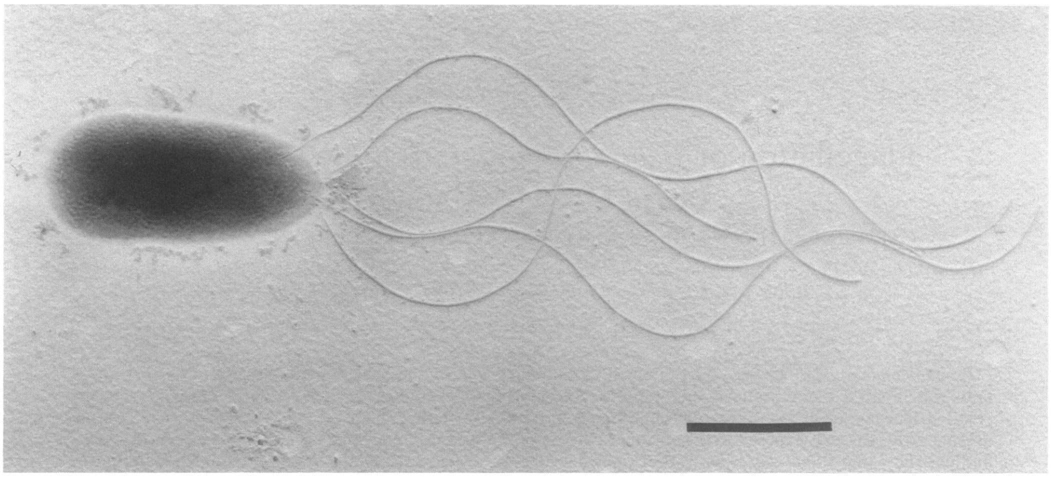

Fig. 2.10 Electron microscopy picture of *Pseudomonas putida* PRS2000: lophotrichous *P. putida* has 3-7 flagella at one of the cell poles. Scale bar is 1 µm. Taken from [12].

the synthesis of EPS and the development of antibiotic resistance. Finally, the developmental circle is completed by returning cells to the planktonic phase.

Living in a complicated structure for bacteria requires abilities to communicate between cells. The cells continuously divide and produce extracellular signals. Those signals can act as environmental messengers for the populations. In several gram-negative bacteria, cell-cell communication mechanisms are involved in biofilm formation [89]. One of the cell-cell interaction is “Quorum sensing” by which bacteria communicate their activities and orchestrate their population behaviors. “Quorum-sensing” is a mechanism which enables bacteria to have cell-cell communication. They produce, release, detect, and respond to the accumulation of self-generated signaling molecules (so called autoinducers) through quorum-sensing process [90]. The signaling molecules are produced continuously by the bacteria. An increase in the bacterial population density causes accumulation of autoinducers. When the concentration of the autoinducers reaches a particular threshold (the “quorum”), a signal transduction cascade is activated in the population and induces a coordinated change in gene expression.

In gram-negative bacteria, there are some common characteristics in quorum-sensing systems (reviewed in [91]). Acyl-homoserine lactones (AHLs) are the most common class of autoinducers for quorum-sensing. They can freely diffuse through the bacterial membrane. The autoinducers interact with some specific receptors that are located either at the inner membrane or in the cytoplasm. When the signals are detected by the cell, they trigger the expression of many genes related to the cell-density dependent process [92].

The biofilm colony contains both motile and sessile cells. The other challenge of being in a biofilm is the cell dynamic in a very concentrated structure. Although the investigation of this specific 3D structure is not an easy task, when the experimental resources are limited, many observation has been clarified that when the colonies were growing on wet agar surfaces, the a variety of collective motion was produced (reviewed in [93]). For instance Cisneros et al. [94] investigated the collective dynamics of *Bacillus subtilis* in densely populated suspension. The cells assembled into swimming clusters locally. The speed exploration of the cells within the clustered showed a pattern of vortices. The experimental finding, together with theoretical investigation, indicated that the transition, from a free-swimming bacterium to being a member of a biofilm, involves extensive changes in the form and the function of the cells [88]. However, these field of researches requires more examination to understand better the cell-cell interaction, which is crucial for bacterial life in their natural habitat.

2.6 *Pseudomonas putida*

Pseudomonas are gram-negetive bacteria found in soil, water, air, food, plants, and animal. Some of them interact with other organisms as facultative pathogens commensal; they can colonize their hosts without inducing infection [10, 95]. They adapt to physicochemical and nutritional niches and tolerate both endogenous and exogenous stresses. They have attracted attention as a platform for biotechnological process, since they have a remarkable metabolic and physiological robustness. *P. putida* are well-known species because of their ability to colonize soils and for their capacity to degrade a wide variety of chemicals (many natural and artificial compound) [9]. They establish mutual relationships with the plant by feeding on root exudates and releasing siderophores, antibiotics and biosurfactants [10]. They also can sense chemical gradients and respond to them using flagella or pili coupled to a chemosensory system [11]. They consume a wide range of chemicals including amino acids, aromatic compounds, organic acids, phosphate, chlorinated compounds, toluene, naphthalene, and sugars [11]. The early study of the *P. putida* flagellation (Ref. [12]) showed that *P. putida* has between three and seven flagella inserted at the pole of the cell body to form a tuft (see polar lophotrichous flagellation in Fig. 2.3C). The chemosensory system of *P. putida* is more complex than that of *E. coli*. However, the canonical chemotaxis system in *P. putida* is expected to be similar to *E. coli* [11].

The swimming pattern of *P. putida* does not show the characteristic tumbling events. Fig. 2.11 displays the motility pattern of *P. putida* with two types of the events. The cell swims in a smooth path and sharply reverses the direction of motion (Fig. 2.11A). Also during swimming, the cell occasionally stops and starts to continue the swimming path with the

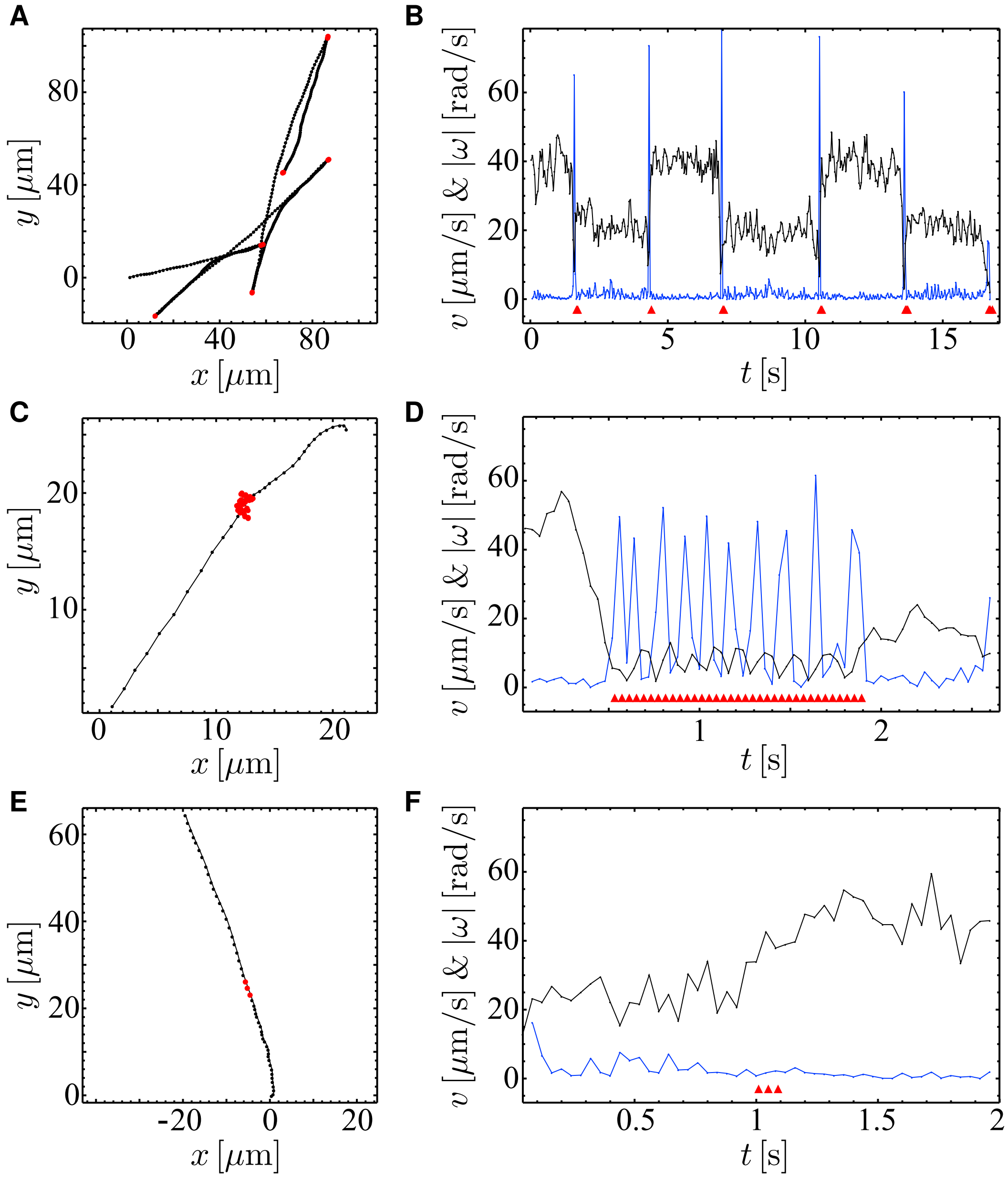

Fig. 2.11 Swimming trajectories of *P. putida*. (A) Trajectory with several reversals. (C) and (E) Trajectories with stop events. The black circles are the center of mass of bacterial cells. The red circles are the reversal and stop events. (B, D, and F) Speed and the absolute value of the angular velocity over time for the trajectories A, C, and E, respectively. Red triangles are the time points of the corresponding events. Taken from [14].

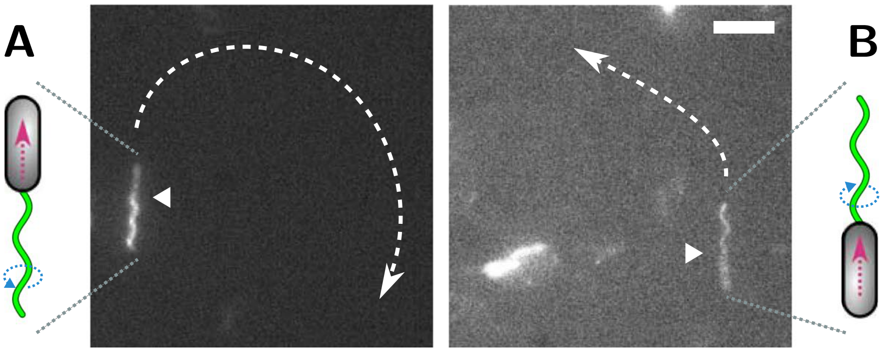

Fig. 2.12 Push and pull flagellar bundle configurations in *P. putida*. (A) and (B) are push and pull modes, respectively. The images were taken in the vicinity of a solid interface. Scale bar is 5 µm. Taken from [15].

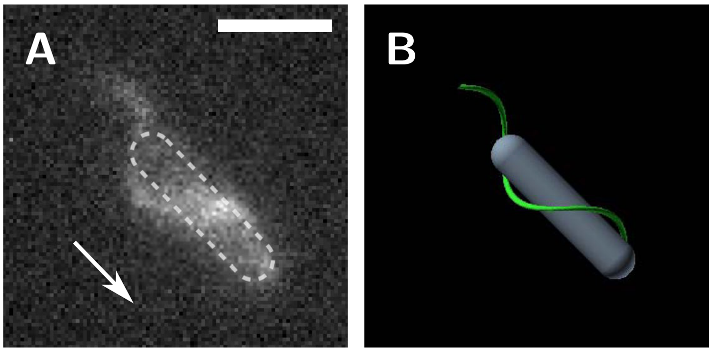

Fig. 2.13 Wrapped flagellar bundle configuration in *P. putida*. (A) Fluorescence image and (B) cartoon of the wrapped mode. The arrows indicates the swimming direction. Scale bar is 5 µm. Taken from [15].

.

more or less same directionality (Fig. 2.11C and D). Another feature of *P. putida* is that their swimming speed can change by a factor of two during reversals (Fig. 2.11B) [14]. Furthermore, several studies were addressed the cell dynamic of *P. putida* in confinement [96, 97]. The researchers in Ref. [96] showed that *P. putida* in the presence of two solid boundaries reoriented more frequently and swam faster. Moreover, *P. putida* in geometrical confinements illustrated the guided trajectories along the open spacings [97].

High-speed video microscopy revealed that the flagella motor in *P. putida* is also bidirectional [15]. During CCW rotation, bacteria swim forward (Fig. 2.12A). Interestingly, it is revealed that the CW rotation can establish two distinct run states; backward swimming (Fig. 2.12B) and wrapped swimming (flagellar bundle wrapped around the cell body while it swims) (Fig. 2.13A and B). Accordingly, *P. putida* has three run states: push, pull, and wrapped. The push state is similar to forward swimming of *E. coli*, when the cell is pushed by the flagella bundle. The pull state starts from changing the motor direction to CW, and the flagella bundle pulls the cell body. When the bundle is wrapped around the cell body, the cell swims with the cell pole ahead. The wrapping mode is a quite new swimming mode, which has been observed in different bacterial species recently [16–18].

Chapter 3

Digital imaging setup

3.1 Introduction

Optical microscopy imaging is a strong means to reveal the structural and dynamical properties of the micro-objects. Most of the key properties of high-quality images are dictated by the choice of an objective lens and the camera. The magnification and resolution of the image are defined by the objective, and the camera determines the temporal resolution of the image series. The previous investigation in our group on *P. putida* motility was done with high temporal/spatial resolution fluorescence microscopy, i.e. with 60x/100x objective and frame-rate of 100-400 frames/s (fps) [15]. The imaging set-up utilized in the study revealed interesting structural and dynamical details of *P. putida* flagella bundle status for the first time. It showed that *P. putida* has a complex swimming strategy (see section 2.6). The flagella bundle could be in push, pull, or wrapped mode during the run phase, and each has particular properties. Therefore a complete understanding of the underlying dynamics of *P. putida* requires information of bundle status and trajectories over time. There are several reasons that using high temporal/spatial resolution fluorescence microscopy for time-lapse measurement of trajectories is not beneficial. Firstly, the flagella had fluorescent markers in our study. Generally, fluorescent dyes (fluorophores) are molecules that absorb an excitation wavelength and emit a different emission wavelength. For that reason, the flagella were the sample that could be detected with fluorescence microscopy and the cell body not. Since *P. putida* has the multi-mode swimming tactic, knowing the relative spatial position of the cell pole, i.e. the cell ending with the tuft of flagella, is critical to distinguish one mode from the other (for instance, pull mode has a cell pole in the direction of the swimming path). This indicated that fluorescence imaging was not sufficient to distinguish flagella bundle configuration, especially when the cell body is not fluorescently stained. The other important feature of high temporal-spatial imaging is the size of image data. The high-speed imaging generates massive amounts of image data that makes it hard to access, analyze, and store them quickly. Furthermore, to present a comprehensive picture of the system dynamic, the numbers of analyzed swimmers define statistical accuracy of the investigation. In order to have an accurate statistical analysis, more image stacks would be generated. Therefore, processing the large amounts of high-temporal/spatial resolution images would be time-consuming.

Although the high temporal/spatial resolution microscopy is a powerful method for detection of the system dynamic within millisecond range, lower resolution could be more beneficial for extracting the information about the underlying cell swimming pattern dynamics which has a time duration with an order of the magnitude of seconds, i.e. *P. putida* has a run duration $\sim$ 1 s. For this reason, most of the studies in this field used bright-field particle tracking microscopy with lower temporal/spatial resolution, i.e. with 20x/40x objective and frame-rate of 20 fps. Decreasing the imaging resolution leads to manageable data production, which is a way to overcome data analysis difficulties and to increase trajectory statistics.

The particle tracking microscopy gives a measurement of the cell body displacement and orientation (Theves. et.al., in Ref. [14] used this method to investige the swimming pattern dynamics of *P. putida*). However, here the missing piece of the puzzle is a description of the flagella movement. We developed a novel high-speed microscopy solution applying the latest hard- and software technology that fulfills all requirements. It captured images with enough resolution to see the flagella bundle status. The image stacks had a moderate size for storing and analyzing. The novel set-up collected large amounts of cell trajectories for statistical accuracy. More importantly, for every single cell body displacement and orientation, the flagella dynamics were visualized. We established a set-up with a LED controller, which produced an alternating sequences of phase-contrast and fluorescence images. The phase-contrast images were processed to track the cell body; afterwards, fluorescence recordings were checked to determine the orientation of flagella by visual inspection.

In the following chapter, we will introduce the novel set-up, which was developed to couple the statistical analysis of the *P. putida* trajectories, and the information of the flagella bundle state. Afterwards, the image processing procedure will be explained. The image processing section will be followed by elucidation of the trajectory analysis tools, which were used to extract the statistical information of the cell population.

3.2 Combined phase–contrast and fluorescence imaging

3.2.1 Imaging set-up

The set-up consists of five devices; (1) IX71 Inverted Microscope (Olympus) equipped with 20× UPLFLN-PH objective (Olympus, Japan), (2) high-speed camera (Orca Flash 4.0, Hamamatsu), (3) a 470 nm blue LED (Prizmatix, UHP-T-LED-460), which was used to visualize the stained flagella filaments in fluorescence (F-L) imaging mode, (4) a white LED (Prizmatix, UHP-LED-White) was the light source for the phase–contrast (P-C) imaging part, and (5) LED controller Triggerscope2 (Advanced Research Consulting) (Fig. 3.1). In the following section, we will explain the sequence of devices utilized step by step to produce the image series of our interest.

(i) Signal production in camera. One of the important parts of the set-up is the manageable camera in order to achieve optimal imaging in our specific range of application. Orca Flash 4.0 has a couple of operation functions and timing outputs that control the imaging timing of an external device and camera. The maximum frame rate of the camera is 100 fps with the effective pixels of 2048 (H) × 2048 (V)[1], which means the camera requires 0.01 s for the sensor readout. During the image readout, the camera sensor was exposed to the light so as to record a frame. The frame rate in our study was 20 fps, which nicely achieved the readout time. The camera was mounted on the microscope, and has a connection to the LED controller Triggerscope2 via the Trigger input port (see inlet of Fig. 3.1). In our particular set-up, the camera become the master and managed the Triggerscope2. In an attempt to track the bacteria cell body parallel with the flagella visualization, we acquired a sequence of combined P-C and F-L images. The combined image series was P-C_1/F-L_2/P-C_3/.../F-L_N for a sequence of N images. Therefore, upon each exposure time[2], the camera output signal was produced and transferred into the Triggerscope2.

(ii) LED controller Triggerscope2 receiving signal form camera. The camera signals arrived in Triggerscope2 controller, which has an embedded Arduino board. The board is an open-source electronics microcontroller, which operates as a small computer. It is able to read the input signal –signal from camera – and turn it into an output – switch on/off the LEDs. The input signal, TTLs (Transistor-Transistor Logic) is sent out over a BNC cable (see inlet of Fig. 3.1) from camera to Triggerscope2 at each exposure.

---

[1] Image with 2048 horizontal and vertical lines.

[2] Exposure time is a period in which a camera sensor is exposed to the light.

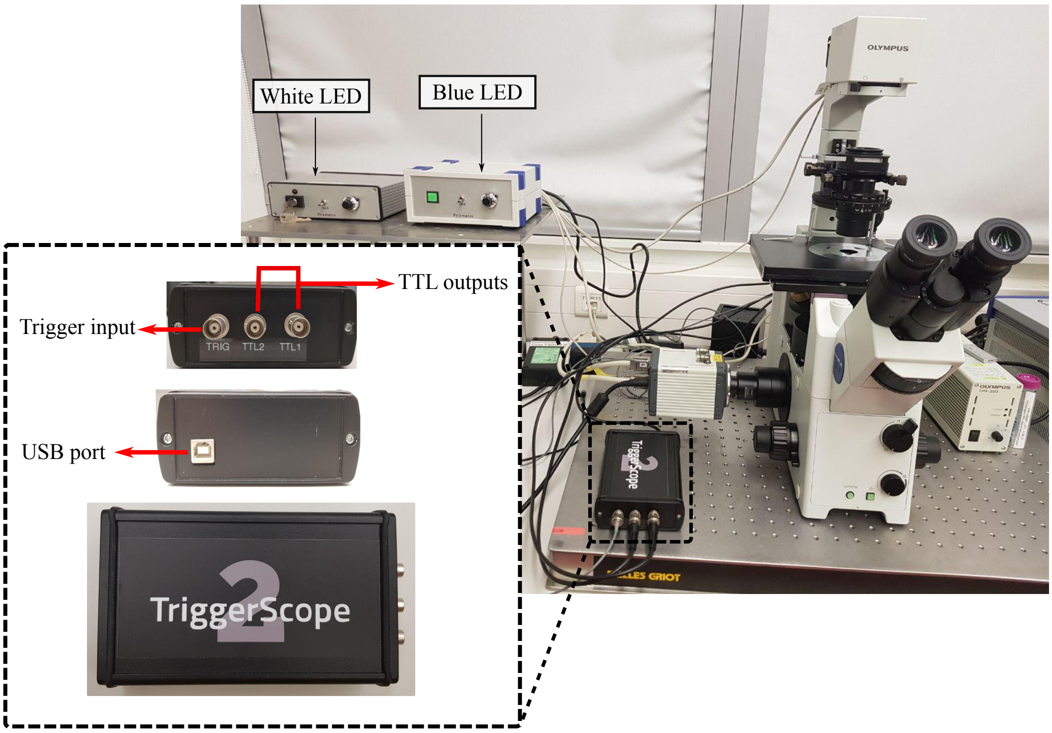

Fig. 3.1 Microscopy Set-up for the Combined Phase–Contrast and Fluorescence Imaging: The camera was mounted on the microscope on one side and linked to the LED controller Triggerscope2 on the other side. The Triggerscope2 has a USB port to connect to the PC, two TTL Channels, one Trigger Input. Two LEDs were applied for two types of imaging, Phase–Contrast and Fluorescence.

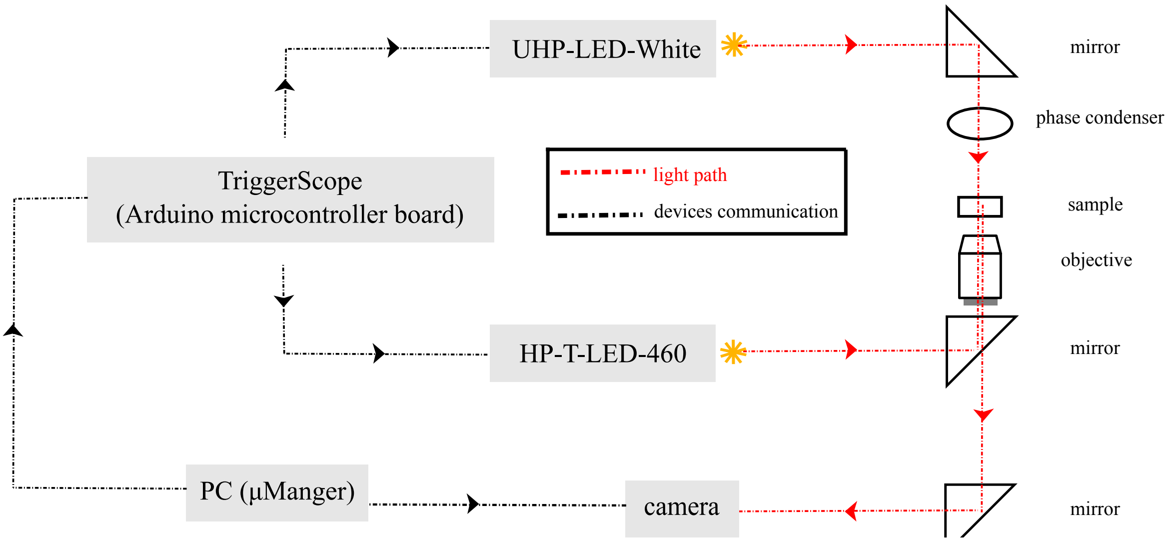

Fig. 3.2 Scheme of the microscope optical path and devices communication. The image acquisition was started by μManger. Upon each exposure time, μManger was programmed to switch On one of the LEDs via Triggerscope.

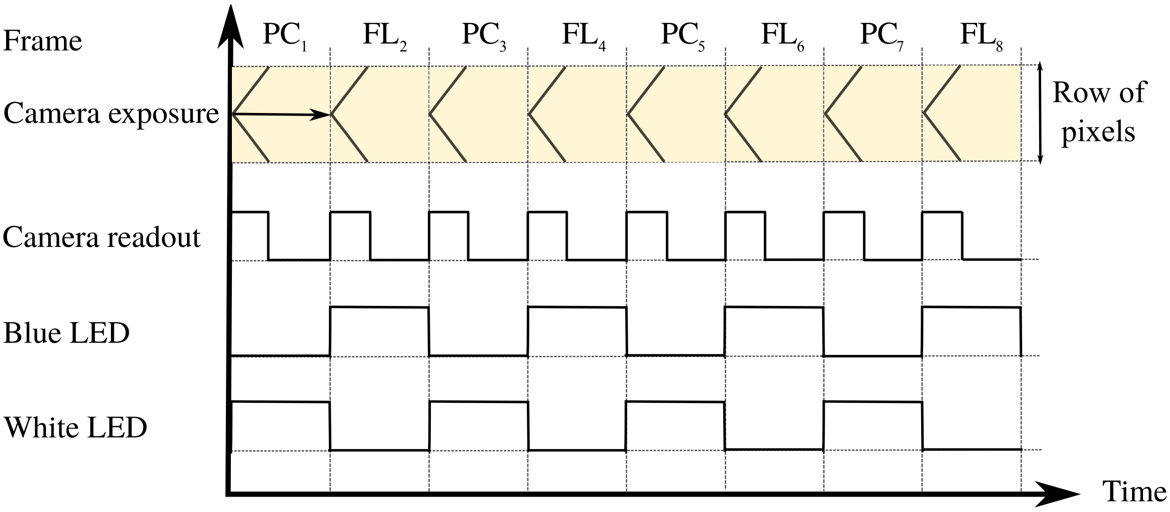

Fig. 3.3 Scheme of signal generation in devices. After exposure, the image readout of the sensor starts row after row, starting from the central row and proceeding towards the sensor top and bottom row. Readout takes around 0.01 s. Simultaneously, one of the LED receives the pulse and is set ON within the exposure; frame P-C_1 with the white LED ON. Next frame, the pulse triggers the blue LED and switches it ON.

The Triggerscope2 includes 2 TTL channels. Each was connected to a LED through a BNC cable. In each frame, one of the TTL channels must be ON[3]. When the TTL channel switches ON, it triggers the connected LED.

(iii) LEDs blinking in each frame. Both LED drivers support TTL triggering. The signal from Triggerscope2 passed through the BNC cables and arrived in the LEDs. The signals set the LEDs to the correct status. Figure 3.3 displays a chart of the synchronized signal production in the devices. The camera sensor readout should be started with the LED ON status. Triggerscope2 manages the signal transferring at a time scale $< 1\,\mathrm{ms}$, which was quite successful to have the corresponding LED ON. Due to the signal arriving at the specific LED, the corresponding images was captured:
Frame1: P-C_1/ white LED ON, blue LED OFF
Frame2: F-L_2/ white LED OFF, blue LED ON
Frame3: P-C_3/ white LED ON, blue LED OFF
$\vdots$
Frame$N$: F-L_N/ white LED OFF, blue LED ON

---

[3] LED is ON when it receives $\sim$ 5 Volts and off when voltage is $\sim$ 0 Volts.

3.2.2 Hardware synchronization

All the devices were controlled by μManger (http://www.micro-manager.org/). In fact, μManger is an open-source, cross-platform desktop application, to control a wide variety of microscope accessories, cameras, illuminators, etc. It has a central capability, Multi-Dimensional Acquisition (MDA), which sends the commands from the computer to the external devices each time a change is required. There is a specific Arduino firmware to use the board with Micro-Manager. After adding the Arduino to μManger's configuration, the camera communicates directly with the LEDs. As we mentioned before, the camera needs $\sim$ 0.01 s for image readout. When it starts, the light source should be ON. The crucial part of the set-up was to synchronize the timing between these two processes. The default Arduino firmware for Micro-Manager has been programmed in such a way that the LED turning ON and image readout was initiated simultaneously. The following steps happened in practice and can be summarized as this:
1: acquisition parameters set in the MDA provided by μManger (exposure time: 50 µs, image number: 600 frames, and image interval: 0.05 s),
2: μManger converts the parameters into the sequence of commands,
3: the camera starts acquisition in streaming mode,
4: Triggerscope2 runs the sequence of commands which is stored in its memory
5: TTL's are updated; during every exposure, one LED receives a TTL pulse and the light turns ON in its sequence of states.
For each sequence, the images were acquired at 20 fps for 30 s.

3.3 Automated image processing and cell tracking

Image processing

A custom Matlab program based on the Image Processing Toolbox (version R2015a and R2018b, The MathWorks, USA) was used to process the image sequences automatically. The software program was written by Marius Hintsche [98] and developed further by the author for the new version of image stacks produced by combined phase–contrast and fluorescence imaging. For each image sequence, a background image was calculated by pixel-wise time average projection. It was subtracted from each frame to eliminate non-motile objects and shading effects. The new set-up might have an overlapped time when both LEDs were ON for a short amount of the time. The phase-contrast frames have a different range of intensity values than the fluorescence ones. Even microsecond overlapped time could introduce some intensity artifacts in the phase-contrast images: a phase-contrast frame with intensity values from the fluorescence illumination. Due to the overlapped time when both LEDs are ON, some of the images possessed intensity values beyond the intensity range of the cell bodies and background. If the overexposure pixels remain on the phase-contrast images, the low-intensity cellular details can be lost. This artifact was fixed with an intensity substitution: overexposure pixels were replaced by the background intensity. The built-in Matlab function *imsharpen* was then applied to enhance edges of the cell bodies using unsharp masking. The unsharp mask filtering is a method that expands the high-frequency edge information in images, which is useful for segmentation. The filter operates by subtracting a smoothed version of the image from the original image to produce the edge of the particle. The smoothed image is obtained by filtering the original image with a low pass filter.

$$Img_{edge}(m,n) = Img_{original}(m,n) - Img_{smoothed}(m,n), \tag{3.1}$$

where m and n are the rows and columns of the image which is a measure of its resolution. The image size of our recording was 2048×2048. Afterwards, the highlighted edge image was added to the original image.

$$Img_{shap}(m,n) = Img_{original}(m,n) + k[Img_{edge}(m,n)], \tag{3.2}$$

where k is a scaling constant that was set with the default Matlab value, $k = 0.8$. To reduce the background noise, the Gaussian smoothing filter was applied using sigma = 2 and *imgaussfilt* (see Fig. 3.4). The putative bacterial cells are distinguished from background using the maximum entropy thresholding algorithm by Kapur et al. [99]. The threshold was calculated for each image in the sequence separately. The median of all threshold values was used to segment the whole sequence. The left panel in Fig. 3.5 is the binary image that came from segmentation. The right panel shows an image after unsharp and Gaussian filtering with the overlaid result of the segmentation process. The binary images were further processed with the morphological operations, *imopen* and *imclose* (with a disk of radius 0.3 µm) to eliminate any noise caused by segmentation. The built-in function *bwconncomp* was used to find all connected objects in the binary images. Size and centroid of the objects were determined using the *regionprops* function. Afterwards, particles with an area between 1 μm^2 to 15.6 μm^2 were considered as single bacterial cells. Finally, trajectories were obtained employing the tracking algorithms by Crocker and Grier [100].

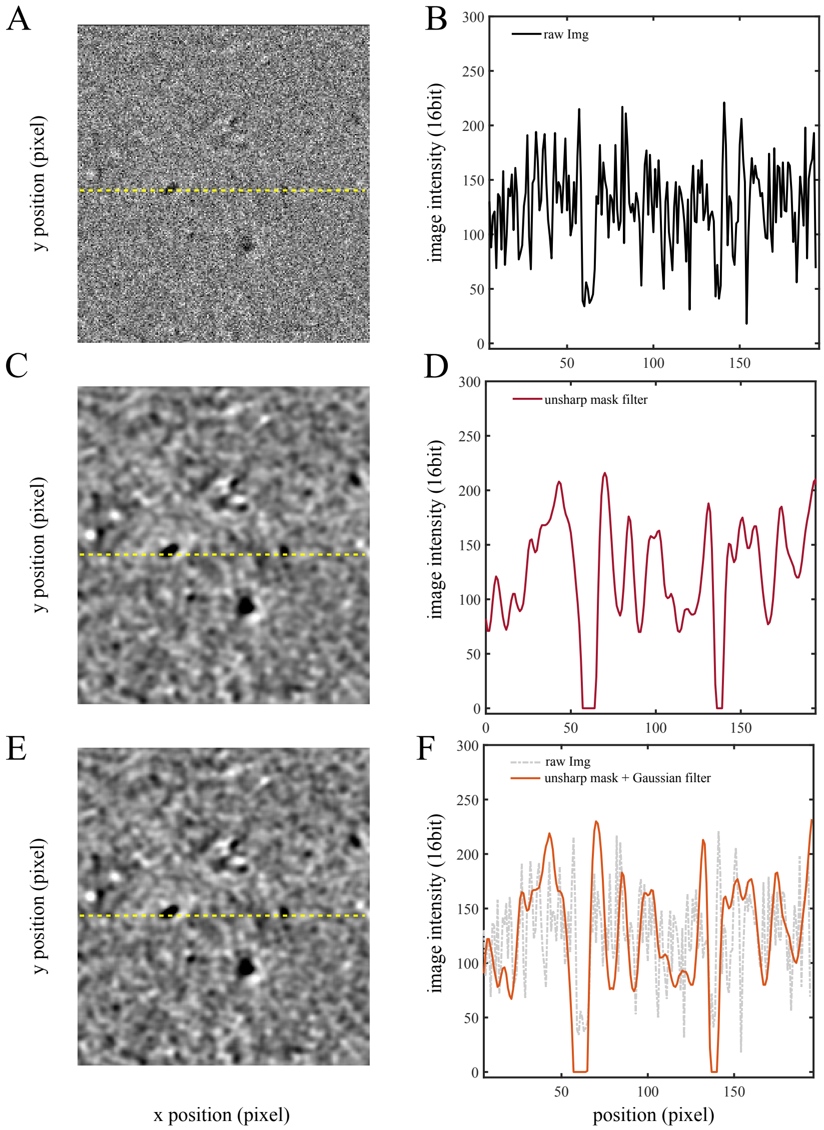

Fig. 3.4 Steps that are taken for bacterial cell detection. (A) A raw image of the phase-contrast microscopy. (B) The intensity profile along the yellow horizontal line in (A). (C) Raw image after unsharp mask filtering to enhance edges of the cell bodies (see description in the text). (D) The intensity profile along the yellow horizontal line in (D) shows the clear separation of the cell and background fluctuations. (E) Raw image after unsharp mask filtering followed by the Gaussian smoothing filter to correct for low and high frequency noise. (F) The line profile.

Analysis of cell trajectories

The Matlab particle tracking software allows us to simultaneously track several bacterial cells. More than 3000 movies of the individual 2D trajectories were extracted. Figure 3.6 is an overview of the extracted trajectories using video microscopy. The trajectories are measured individually. During image acquisition, some of the cells moved in and out of focus. For that reason the length of the tracks varied over the video microscopy period. The trajectories were stored in an array that looks like that:

index i	time j	x	y
1	189	1400.9	1409.7
1	190	1400	1411.6
1	191	1399	1412.6
1	192	1397.9	1413

The first column is the trajectory index number i = 1, 2, 3, ...; the second is the time index j = 1, 2, 3, ...; the third and fourth columns give the corresponding center of mass (centroid) bacterial cell positions in the (x,y) imaging plane,

$$A_{ij} = (x_{ij}, y_{ij}) \tag{3.3}$$

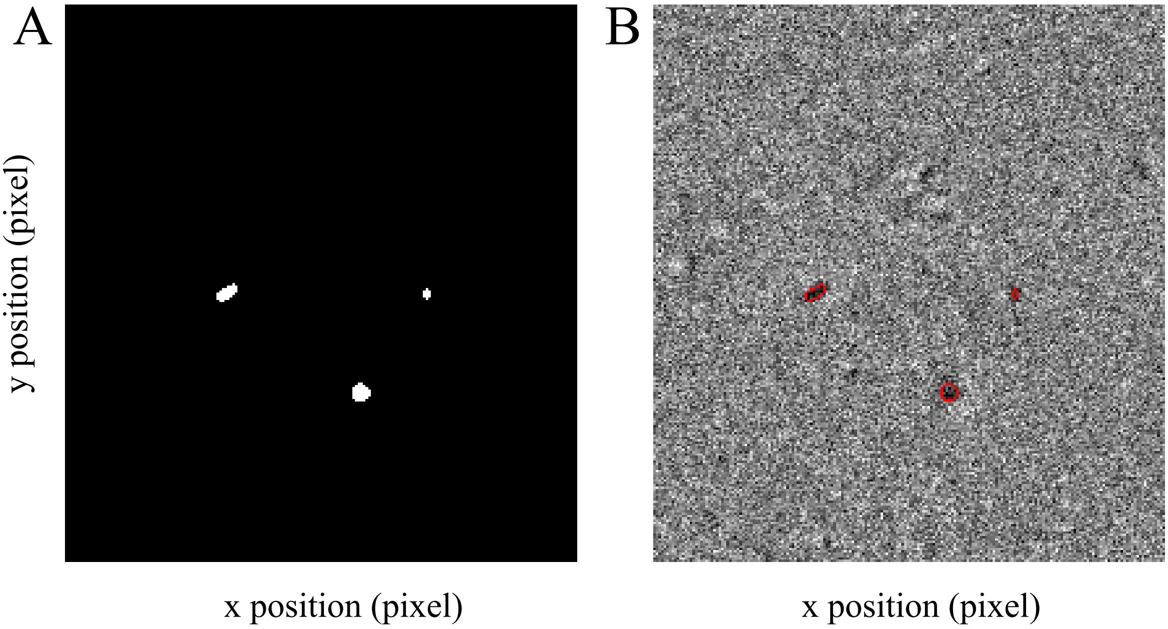

Fig. 3.5 Illustration of the segmentation result. (A) The binary image after segmentation. (B) The raw image with the red overlaid detected regions. Cells can be distinguished as black values on a gray background.

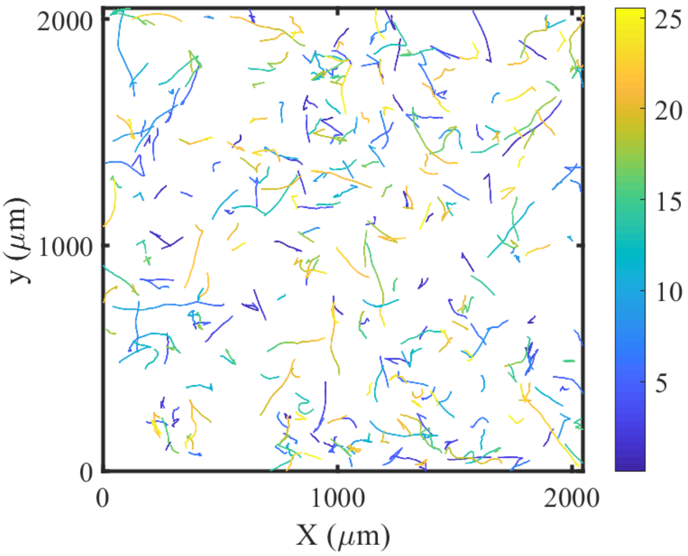

Fig. 3.6 Representative trajectories over 27 s of one of image stack. The color bar shows the time evolution of the images capturing.

of the trajectory identified i at the time j.

Eventually more information was extracted from the movie processing. Polar coordinates can be calculated from the centroid positions along the trajectory,

$$r_t = \sqrt{x_t^2 + y_t^2}, \tag{3.4}$$

$$\theta_t = tan^{-1}(\frac{y_t}{x_t}). \tag{3.5}$$

The instantaneous translational velocity and angular velocity were derived from the change in the position and direction of propagation between two subsequent time intervals, respectively,

$$v(t) = \frac{\mathbf{r}(t+\Delta\tau) - \mathbf{r}(t)}{\Delta\tau}, \tag{3.6}$$

$$\omega(t) = \frac{\theta(t+\Delta\tau) - \theta(t)}{\Delta\tau}. \tag{3.7}$$

Afterward, the curvature of the trajectories was calculated. The curavture is defined by

$$\kappa = \frac{d\theta}{ds}, \tag{3.8}$$

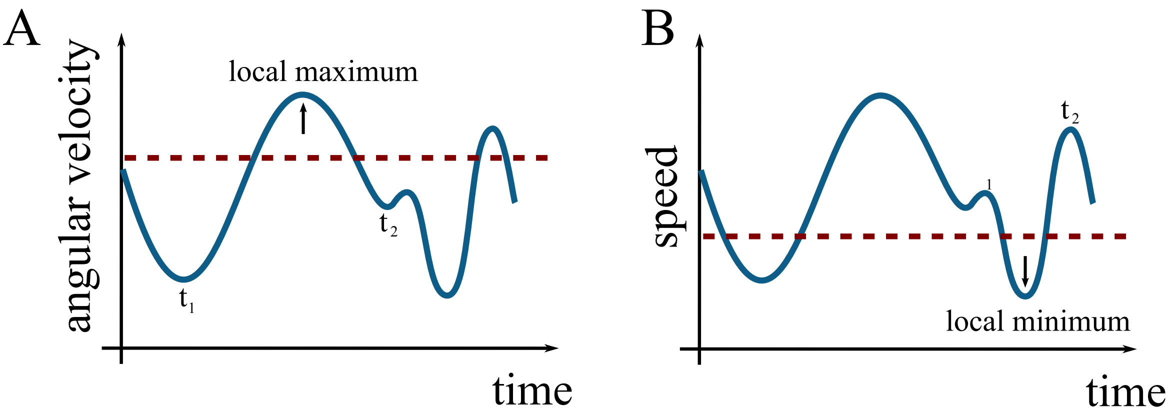

Fig. 3.7 Scheme of heuristic run-tumble analysis. (A) and (B) are the time series schemes of angular velocity and speed, respectively. The red dashed lines are defined by α and β in speed (B) and angular velocity (A), respectively.

where $ds = \sqrt{dx^2 + dy^2}$ is the displacement between two consecutive data points. For every individual track, the curvature was measured over time. The median value for each trajectory was taken, and 5% of the trajectories with the highest median curvature were filtered out, in order to dismiss the pathogenic cells, which could not form a stable the bundle [101].

3.4 Trajectory patterns classification

Heuristic run-tumble analysis

In order to categorize the run and event phases, an automatized event recognition algorithm was applied, as introduced by Masson *et al.* [102] and modified by Theves *et al.* [14]. The idea is to identify large fluctuations in the direction of motion and/or sudden drops of the speed. First, the trajectories were smoothed using a second-order Savitztky–Golay filter with a window size of 5 data points [103]. The instantaneous speed $v(t)$, direction of propagation θ, and turning rate $\omega(t)$ were evaluated on the smoothed tracks. First, we determined all local minima (maxima) of instantaneous speed v (turning rate ω) located at t_{min} (t_{max}) in the time series. Afterward, two maximum (minimum) at time $t_{1,2}$ located in the vicinity of every minimum (maximum) were determined. The depth (height) Δv ($\Delta\omega$) of the minimum (maximum) can be defined as

$$\Delta v = \max[v(t_1) - v(t_{min}), v(t_2) - v(t_{min})], \tag{3.9}$$

$$\Delta\omega = \max[|\omega(t_{max})| - |\omega(t_1)|, |\omega(t_{max})| - |\omega(t_2)|]. \tag{3.10}$$

Two threshold parameters on the speed and angular velocity were adjusted to identify events. If $\Delta v/v(t_{min}) > \alpha$, with an $\alpha = 3$, an event was detected. Its duration was set to the time for which $v(t) \leq v(t_{min}) + 0.55$. For the angular velocity, an event was detected if the total angular deviation during the time interval t_1-t_2 sufficiently exceeded the directional change because of passive rotational diffusion, i. e.,

$$\sum |\Delta\theta| \geq \beta \sqrt{D_{rot}(t_2 - t_1)}, \tag{3.11}$$

with $D_{rot} = 0.1\ rad^2/s$. In fact, D_{rot} is the rotational diffusion of a passive sphere with the radius of 1 µm., and $\beta = 0.65$. The event duration was defined around t_{max} where

$$||\omega(t_{max})| - |\omega(t)|| \leq 0.85\Delta\omega. \tag{3.12}$$

Figure 3.7 illustrates the scheme of the method. The horizontal red dashed lines defined by α and β are the parameters to categorize the data points as events. The data points with values larger (smaller) than the dash line in angular velocity (speed) time series are the events. Only one of the criteria – speed or angular velocity – is sufficient for a time point to be identified as an event (see the scheme of a trajectory with events identified by the event detection method in Fig. 3.8A). The event detection was verified by visual inspection. The same parameters were used for the experiments reported in the following chapters.

Turn angle

The heuristic run-tumble analysis provided the segments of runs and events for every trajectory. The turn angle is the change in swimming direction from the end of one run to the beginning of the next run. To determine the turn angle ψ (Fig. 3.8B), a linear regression

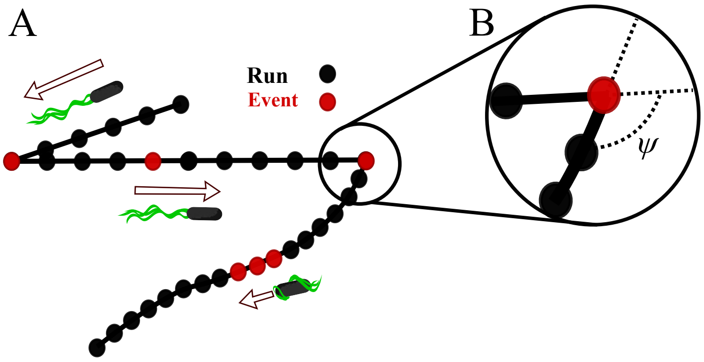

Fig. 3.8 (A) Scheme of a cell trajectory with turning events identified by the algorithm. The black circles are the cell body center of mass, and the red circles are events. (B) Turn angle definition ψ.

was performed to fit the last three data points of a run and the first three data points of the subsequent run with a vector. The turn angle was the angle within these two vectors.

3.5 Conclusion

A new high speed combined phase-contrast and fluorescence imaging set-up was established to disclose the swimming strategy of the multi-mode swimmer *P. putida*. Indeed, the combined microscopy approach was a bridge between the high speed/resolution fluorescence microscopy and the common time-lapse recordings of swimming cells with phase-contrast microscopy. The first microscopy set-up reveals the structural and dynamical details of the fluorescently tagged flagella, and the second one produces the information of bacterial cell body dynamics. Both pieces of the information were simultaneously gathered in the new set-up, which created a fully automated phase-contrast/fluorescence image series to provide the status of the cell body position relative to the flagella bundle for every single data point. This is crucial for better understanding the swimming tactics of the multi-mode swimmers like *P. putida* with different types of flagella configurations during swimming. The image stacks generated by the set-up had adequate resolution to visualize the orientation of the flagella bundle. Also, the stacks had a reasonable size to manage the processing time and to generate enough trajectories for accurate statistical analysis accuracy.

Chapter 4

Statistical analyzing of *P. putida* swimming modes

Recent research in Ref. [15] shed new light on the motility pattern of *P. putida*. The study was optimized to visualize the flagellar dynamics with a high spatial and temporal resolution. The high temporal/spatial resolution images of the flagellar bundle of *P. putida* revealed interesting information about the underlying motility pattern: *P. putida* has a complex swimming strategy composed of three run modes (push, pull, and wrapped, see Fig. 2.12 and 2.13) and two types of events (turn, and stop). The flagella of *P. putida* are driven by bidirectional rotary motors. Both CCW and CW rotations can make steady run modes. Synchronized CCW rotation of motors leads to the formation of a flagellar bundle at the rear of the cell body. As a result, the cell is pushed by the bundle. CW motor rotation enable two different flagellar bundle configurations with diverse geometrical properties. One is the pull mode; the bundle pulls the cell body. The other mode is wrapping. In this case, synchronized CW rotation of the motors again make a bundle. However, the bundle wraps around the cell body when it is swimming. Both pull and wrapping modes have the flagellated cell pole as a leading pole. The flagellar polymorphic shapes for the push and pull modes are the same. The filaments are left-handed helices of radius $0.4 \pm 0.1\,\mu\text{m}$ and pitch $2.0 \pm 0.1\,\mu\text{m}$. The wrapped mode has a more compacted left-handed polymorphic state with $0.6 \pm 0.1\,\mu\text{m}$ radius and $2.1 \pm 0.3\,\mu\text{m}$ pitch. The swimming speed of the cell is distinct for each mode. The pusher/puller swimmers have a mean speed of $25.4 \pm 0.4\,\mu\text{m/s}$, whereas the cells with wrapped flagellar bundle are slower, having with the mean speed of $15.5 \pm 0.2\,\mu\text{m/s}$ [15].

Those information are not all we know about *P. putida*. Our preliminary knowledge of *P. putida* came from the research by Theves et al. (Ref. [14]). The early investigation of the relatively long *P. putida* trajectories revealed quantitative information of the cells behaviour without the flagellar bundle visualization. This type of routine image recording have some important advantages. Besides the data size which is much smaller in comparison to high temporal/spatial resolution microscopy imaging, the relatively long trajectories with more swimming episodes enable to test modeling hypothesis.

Both experiments together gave us interesting picture of the motility pattern of *P. putida*. High temporal/spatial resolution microscopy images provide detailed information about the flagellar bundle, whereas the cell tracking images revealed statistical features of the swimming trajectories. However, there are missing pieces of the whole picture; how do the three different flagellar bundle configurations and the two types of events contribute to the environmental exploration of *P. putida*. In this chapter, we present novel aspects of *P. putida* motility which were obtained by the newly established microscopy set-up (as introduced in chapter 3). The advantage of this combined phase-contrast/fluorescence imaging is that it enables us to track the cell body and visualize the flagellar bundle simultaneously. Most of the findings presented below have been published in Ref. [104].

4.1 Materials and Methods

Cell Culture

Pseudomonas putida KT2440 FliC$_{\mathrm{S267C}}$ (*P. putida* FliC) is a genetically modified strain from the wild-type *Pseudomonas putida* KT2440 [105]. The genetic modification causes a single cysteine substitution in the flagellar filament protein as described in Ref. [15]. *P. putida* FliC from glycerol stocks stored at $-80\,^{\circ}\mathrm{C}$ was cultured in an overnight shaking culture of Luria Bertani (LB) Broth (Lennox, Sigma Aldrich). $50\,\mu$l of the cell suspension were evenly spread on a solid LB agar plate (Miller, ForMedium) and incubated overnight at $30\,^{\circ}\mathrm{C}$. The bacteria sample was collected with an inoculating loop from the plate and streaked on a new LB agar plate for single colony isolation and then incubated with the same conditions. The LB plate containing bacteria was stored at $4\,^{\circ}\mathrm{C}$ and utilized as the cell source for three weeks.

The single colony was picked up from the plate and grown in 50 ml Tryptone Broth (TB) ($10\,\mathrm{g\,l^{-1}}$ tryptone (Applichem), $5\,\mathrm{g\,l^{-1}}$ NaCl) overnight being shaken at 300 r.p.m and $30\,^{\circ}\mathrm{C}$. The overnight cells culture which contained the highly motile bacteria were directly used for further experiments.

Staining Flagellar Filaments

The cell suspension was washed free of growth medium by centrifugation (4000 rpm, 4 min, room temperature), followed by gentle resuspension of the pellet in 500 µl motility buffer with glucose (MB+) (11.2 $\mathrm{g\,l^{-1}}$ K2HPO4, 4.8 $\mathrm{g\,l^{-1}}$ KH2PO4, 3.93 $\mathrm{g\,l^{-1}}$ NaCl, 0.029 $\mathrm{g\,l^{-1}}$ EDTA and 0.5 $\mathrm{g\,l^{-1}}$ glucose; pH 7.0). The cells were then labeled with 50 µl Alexa Fluor 488 C5-maleimide dye (Life technologies) stock solution (1 ml dye, 1 ml DMSO (Prolabo)) on a rocker shaker at 40 rpm for ~30 min. The previous steps were the standard protocol to prepare the fluorescently stained flagellar bundle for *P. putida* experiments.

For the bulk experiment, the cells were sedimented and washed again carefully (2500 rpm, 1.5 min, room temperature) twice with 1 ml of MB+ to remove residual free dye. The cell suspension was filled into an ibiTreat μ-Slide Chemotaxis 3D (Ibidi, Martinsried, Germany) (Fig. 4.1). The final OD_{600} of the cell suspensions was 0.02 before filling them into the chemotaxis chamber. The μ-Slide Chemotaxis 3D has three units, and each unit consists of two large reservoirs connected to a central channel (observation area). The central observation area was filled with MB+. For the bulk assay, both reservoirs carried the cell suspension without any chemoattractant to ensure a homogeneous environment and avoid spurious drift.

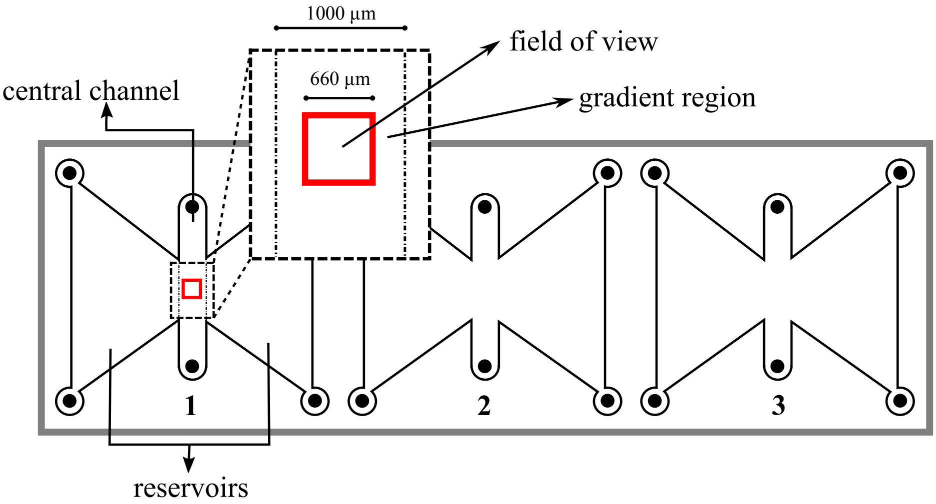

Fig. 4.1 Schematic of Ibidi μ-Slide Chemotaxis device. The chamber consists of two large reservoirs connected to a central channel. In this study, both right and left reservoirs were filled with bacterial cell suspension without chemoattractant. The video microscopy was used to visualize bacteria in the region of the field of view marked in red. Taken from [104].

4.2 Simultaneous cell tracking and visualization of flagella

The swimming behavior of a bacterium can be described by the measurement of the displacement and orientation of the cell body (as described in section 3.3). These measurements will be complemented by the information on the flagellar bundle configuration. We achieved a combination of those data with sufficient quality using the new microscopy set-up. The set-up was examined on our model organism *P. putida* in the bulk fluid of the experimental dishes with and without a chemoattractant gradient. The details of the experimental procedure, cell tracking, and the calculation of the motility statistics was described in chapter 3. In this section, we first present the main observations of the swimming pattern of *P. putida*.

In order to ensure an effective image acquisition, we need, at the one hand, a high spatial resolution to distinguish the flagellar bundle configurations clearly, and on the other hand, high enough temporal resolution. The temporal resolution is also essential for the complete picture of the run mode details without missing too much information. We tried to have a combination of good spatial-temporal resolution in our study. Since *P. putida* has the mean run time of $\tau = 1.5 \pm 0.07\,\mathrm{s}$ [14], imaging about 30 s for each image stack provided a considerable number of trajectories with more than one events. Our temporal resolution, which is 20 fps for cell tracking, is adequate to detect the run and events as well.

As described in the methods section, the image series were acquired with the alternating sequence of phase-contrast and fluorescent frames. To better comprehend the set-up, let us imagine we have a recording for 1 s with the frame rate of 20 fps. Therefore the image series contains 20 frames (Fr-1, Fr-2,..., Fr-20). All of the even frames are the fluorescent images which picture the flagellar bundle. The rest is the time series which was used for the cell tracking. In other words, we have ten frames containing the cell body (Fr-1, Fr-3, Fr-5, ..., Fr-19) with the time delay of 0.1 s. In between each odd frame, we have the information of the flagellar bundle. By aligning the linear interpolation between adjacent phase-contrast images (e.g. Fr-1 and Fr-3), and the fluorescence images (e.g. Fr-2), the details of bacterial swimming mode for each time step can be revealed. Since the flagellar bundle is a stable configuration for the whole run period, the time delay between the sequential fluorescent/phase-contrast images is negligible.

Figure 4.2a shows one exemplary trajectory of *P. putida*. The track is a representative case of *P. putida* swimming behaviour; the cell was swimming in the bulk and performed all types of swimming strategy which were illustrated before with the high speed/resolution microscopy images of Ref. [15]. The phase-contrast images contain the cell body and each data point along the track (circle markers) displays the cell body center of mass. The

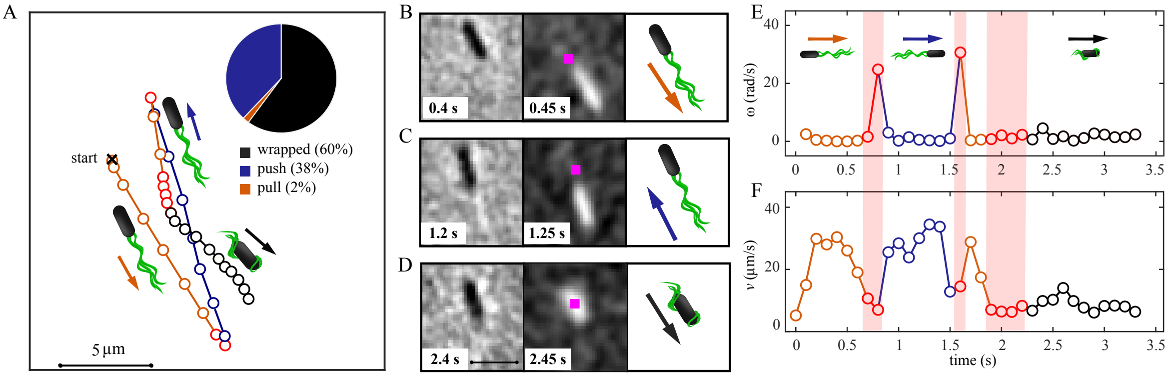

Fig. 4.2 Illustration of the combined fluorescence/phase-contrast microscopy technique enabling tracking of the multi-mode swimmer *P. putida* with simultaneous information on the conformation of the flagellar bundle. (A) A typical trajectory containing multiple changes of the flagellar conformation: cell positions displayed by circular markers at 0.1 s intervals. The three run modes are highlighted in color: pull (orange), push (blue) and wrapped (black). A schematic of the flagellar bundle configuration is placed close to the corresponding run state (not to scale). The arrows are the swimming direction. The transition events, identified by the tumble analysis (see section 3.4), are shown in red. Furthermore, the frequency of observations of the different swim modes is represented as an inset. The panels in the middle (B-D) represent the corresponding image series of phase-contrast (left) and fluorescence (middle) with the time delay of 0.05 s between two consecutive phase-contrast and fluorescence images. The three swim modes are symbolized by cartoons on the right. The phase-contrast images are utilized to track the cell body, whereas fluorescence images contain information about the state of the flagellar bundle. In the fluorescence images, the position of the cell body, obtained by linear interpolation between adjacent phase-contrast images is indicated by a pink rectangle. The first row (B) displays the cell in the pull mode with the flagellar bundle placed in front of the cell body, the second shows the push mode (C) characterized by a long tight bundle located behind the cell body and the third row (D) is the wrapped mode identified by an oval-shaped bundle covering the cell body. (E-F) Time series of rotational velocity ω (E) and swimming speed v (F) providing the basis for the automatized recognition of runs and events (same colour scheme as in A). Scale bars are 5 μm. Taken from [104].

color codes show different episodes of the swimming phases (same as the rest of the plots). Turn and stop events (marked in red), which separate individual runs, were identified by the automatized tumble recognition algorithm based on the time series of cell speed and angular velocity (see see section 3.4) [14, 102]. The algorithm categorized the tracks into runs and events. Afterwards, the flagellar bundle configuration for each run was determined by visual inspection of the fluorescent image series. For the purpose of validation of the set-up, the precise details of the flagellar bundle configuration among the three running modes should be distinguishable. The first and second columns of the panels in Fig. 4.2B-D

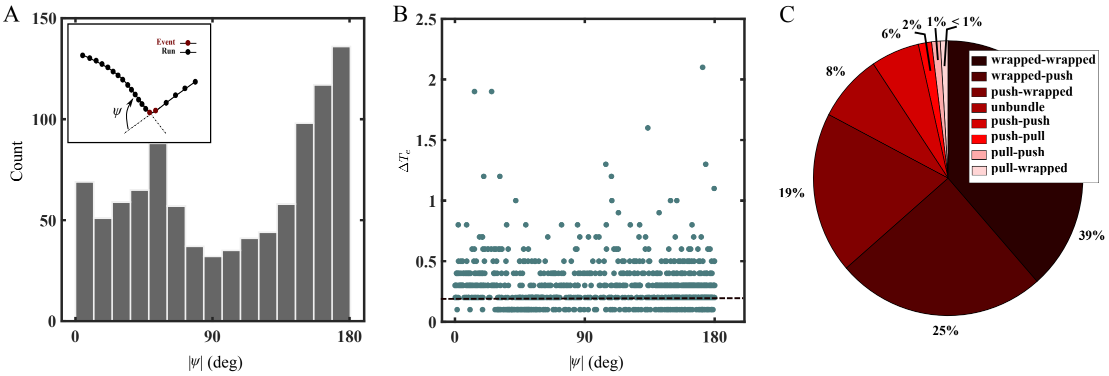

Fig. 4.3 Analysis of *P. putida* turn angle. The analysis is based on the bulk experiment. (A) The bimodal distribution of the turn angle of all events with two peaks; a narrow one $\sim 180°$ and a broad one at $\sim 60°$. (B) The event duration,Δt_e ,as a function of reorientation. The dashed line represents the median, $\langle \Delta t_e \rangle$. (C) The contribution of transition scenarios in this study.

are the snapshots of phase-contrast and fluorescent images together with the corresponding swimming mode cartoon. The second column is showing the fluorescently tagged flagella images with the interpolated center of mass of the cell body marked by a pink rectangle. The first column shows the cell body by a black oval shape which was used for tracking. The overlapped center of mass on the fluorecently labeled bundle provides us enough information about the bundle configuration. The wrapped run was detected if the cell body was covered by the bundle, which has an oval-shape with the similar dimension of the cell (Fig. 4.2D). However, the push and the pull configurations (Fig. 4.2B, and C) have longer and thinner polymorphic shape and, the cell body is located ahead/behind the bundle. The combined information provides sufficient information to distinguish the different run modes. Using those kind of information, the runs in one track were color coded to represent different bundle configuration.

The time series of speed and angular velocity displays complementary information about the run modes and events properties (Fig. 4.2E and F). The push runs were on average with the factor of two faster than the wrapped modes. Moreover, turn and stop events were distinguishable. The turn events caused the sharp spikes in the angular velocity time series combined with the drop of the swimming speed. In contrast, pausing events were the result of decreasing the speed with or without change of the motion direction.

Within the temporal and spatial resolution achieved in our study, the bundle configuration of the single cells is reliably detectable. Moreover, the noticeable number of trajectories with the bundle information provide a high statistical significance. The diagram in Fig. 4.2c, represents the fractions of each push, pull, and wrapped states, by imaging 1799 trajectories

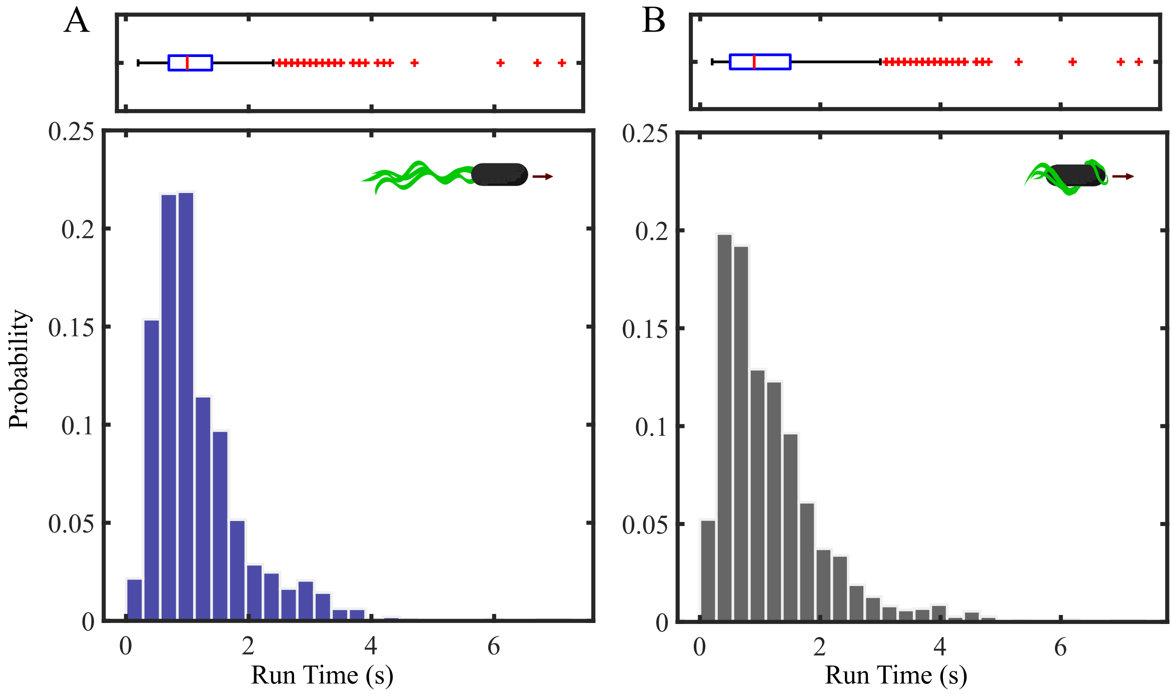

Fig. 4.4 $P(\Delta t_r)$ of (A) push runs, (B) wrapped runs together with the visual representation of key statistical values in box plots. The red line inside the boxes show the median values. The probabilities are built from (A) 969 runs for the push and (B) 1472 runs for the wrapped.

in the bulk. The majority of runs observed in this study belongs to the wrapped and pushing modes. Only a small fraction of the runs remained in the stable pulling mode.

4.3 Statistical analysis of bulk swimming

As mentioned earlier, the motility pattern of *P. putida* consists of two types of runs (push/wrap), separated by events. *P. putida* has two type of events; stop and turn. We evaluated the probability distribution of the run duration, Δt_r. The histograms in Fig. 4.4 does not show significant difference between push and wrapped run duration distributions. One useful parameter to better understand the physical features of the event is turn angle, ψ, which is the change of the direction of motion from end of one run to the beginning of the next run (inset of Fig. 4.3A). The turn angle distribution of *P. putida* has two distinguishable peaks; one at 180°and one at 60°as can be seen in the nonuniform distribution for $|\psi|$ in Fig. 4.3A. Furthermore, the events duration is typically of the order $\Delta t_e \approx 0.3\,\text{s}$, and the scatter plot in Fig. 4.3B does not show any clear correlation between the event duration and corresponding turning angle.

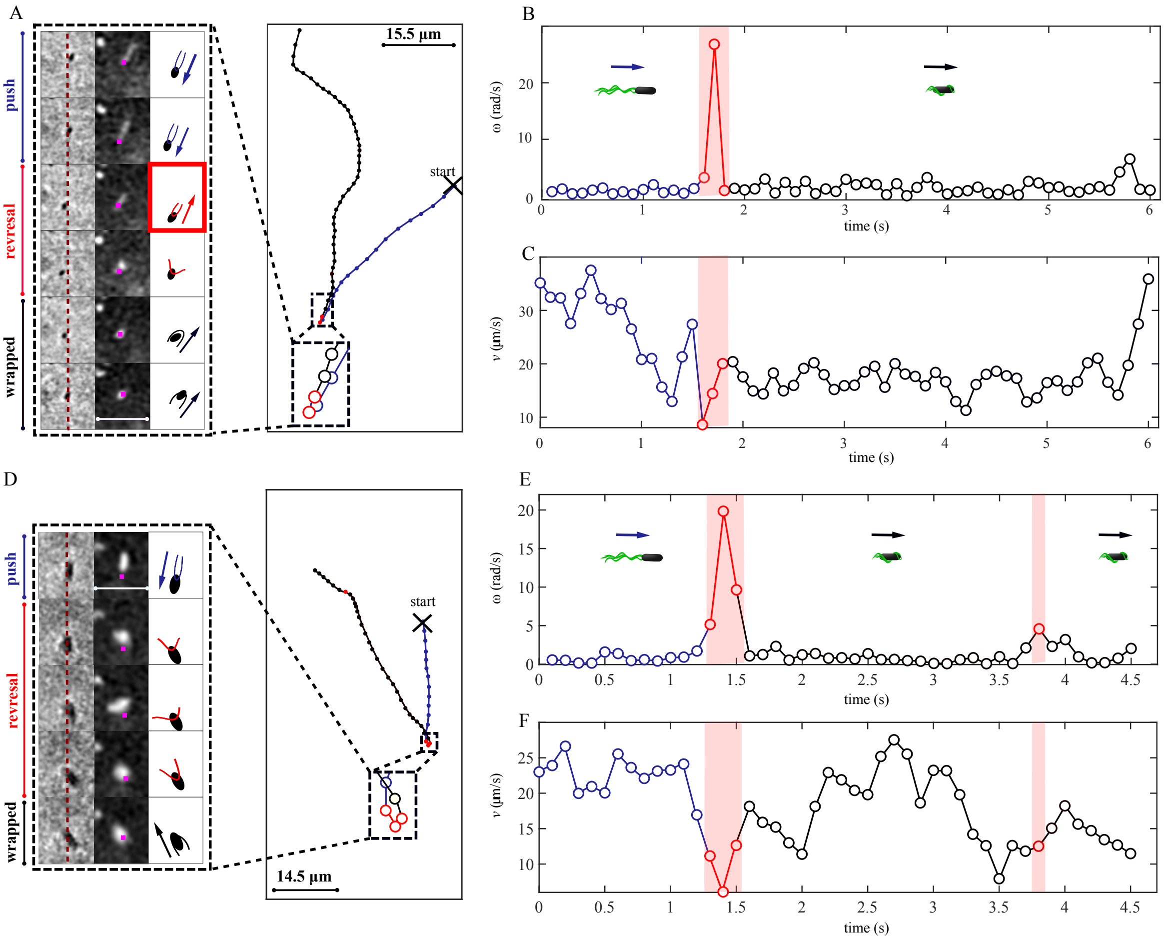

Fig. 4.5 Cell trajectory containing a reversal as a result of the push to wrapped transition. (A) Right hand panel shows the tracked cell positions. The cell swam in the push mode and after a reversal, the flagellar bundle changed to the wrapped mode. The overlapping forward and backward parts of the trajectory close to the reversal may be the result of a short intermediate pull phase, see the rectangular inset. The left hand panel displays the raw image series of the corresponding data points together with the schematic representation. The dashed dark red line provides a reference for cell position. The flagellar bundle marked by a red rectangle showed the tight and long bundle and could be the sign of the short intermediate pull mode with duration $< 0.05\,\mathrm{ms}$. (B) and (E) Time series of rotational velocity ω, and (C) and (F) swimming speed v. (D) Push to wrapped transition with a reversal reorientation. Cell trajectory contained two run modes and two events. The rectangular inset shows the selected data points included the reversal. The corresponding raw image data in the left hand panel shows the bundle transition from push to wrapped. The bacterium with the push mode swam. After the short episode of the reversal, the bundle wrapped around the cell body. During the reversal, the cell body relocated forward while the bundle deformed simultaneously. This type of trajectories presents the indication of a direct push to wrapped transition without any intermediate phase (see also Movie S3). Taken from [104].

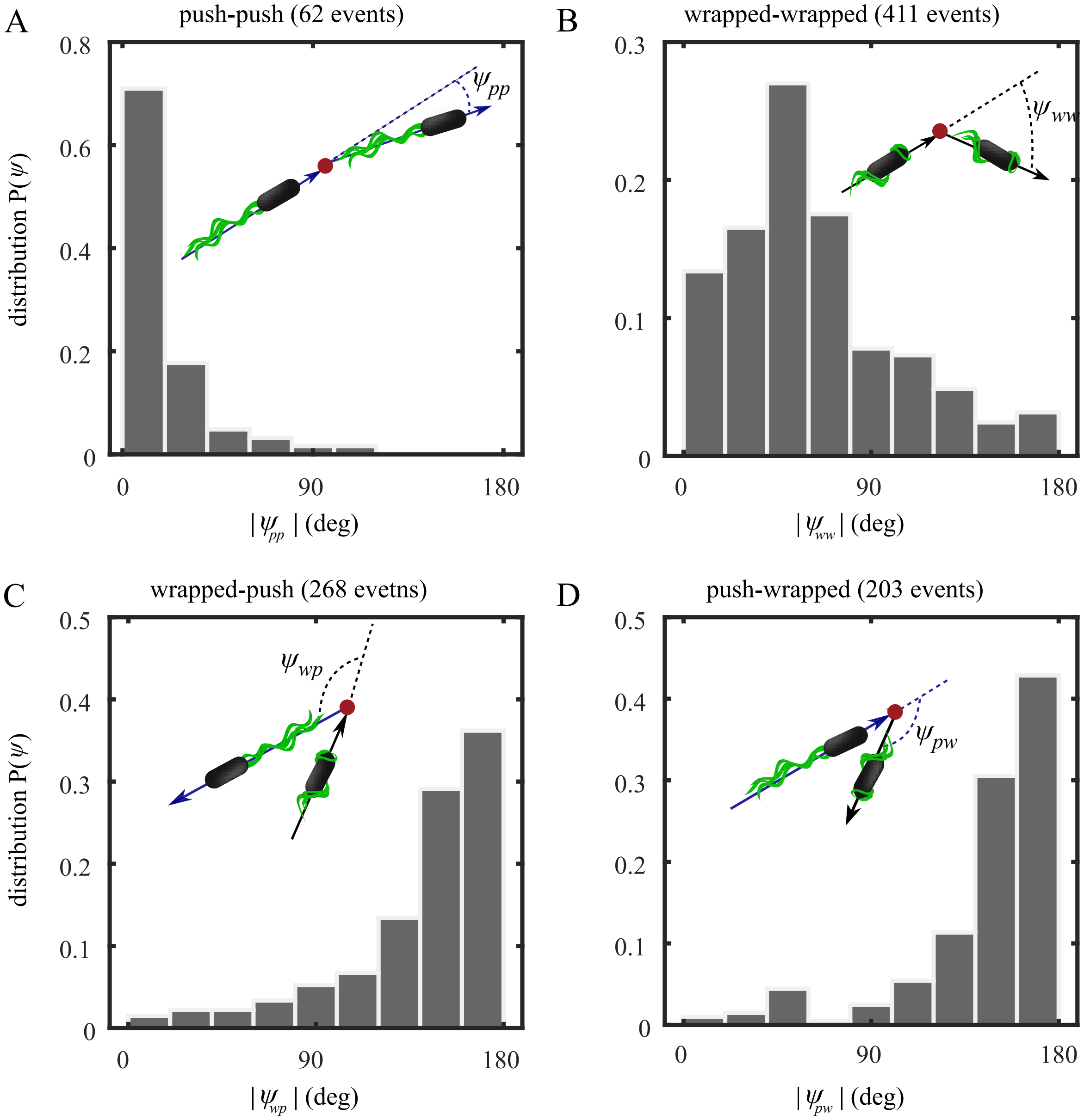

Fig. 4.6 Turn angles of transition scenarios. (A) The narrow turn angle distribution of the motor stops during push run modes. (B) The broad distribution of turn angle of wrapped swimmers with occasional stops in their swimming path. (C) and (D) The transitions from push to wrapped run modes (and vice versa) built the peak at $\sim 180°$. Taken from [104].

Knowing the state of the flagellar bundle for every single run enables us to extract separate turn angle distributions for the different transition scenarios. The pie plot shows the percentage of the all the transitions from 1067 events (Fig. 4.3C). The unbundle mode indicates the disability of the bacterial cells to establish the bundle. The transitions with unbundle title were dismissed from the statistical analysis, and refers to the transitions with at least one unbundle run. The reason of disability is unclear and could be a consequence of bacterial sample preparation. After excluding the unbundle runs, the 987 transitions were analyzed for the plots in 4.3A and B. Further investigation shows that the pull mode engaged in less than 4% of the transitions, which is predictable since 2% of the observed runs were in this mode in contrast to the earlier data presented in Ref. [15]. It has not been possible to provide definitive answer to this matter. One possibility could be that the pulling mode is a short intermediate episode of the flagella configuration transition between the push and wrapped modes, and it is covered up by the time resolution of this study. By investigation in detail, this kind of transition could be classified into two groups. One type of push to wrapped transition among the population had approximately the same overlapped parts during forward and backward with a reversal (rectangular marked area of trajectory in Fig. 4.5A). One explanation could be that this type of reversal reorientation needs the pull run mode in order to make the overlapped part. However, the stability of pulling flagellar bundles has been questioned by theoretical studies and experiments on macroscopic helical bundles [106, 107]. Besides, another type of this transition (Fig. 4.5D) did not experience the overlapped forward and backward trajectory part. That pieces of evidence held the strong clue indicating that the behavior is a result of direct transit from pushed bundle to wrapped without any intermediate phase. Also, Kinosita et al. reported the same direct transition in *Burkholderia* sp. RPE64 which has the same flagellation pattern like *P. putida* [17].

Fig. 4.6A-D displays the extracted turn angle distribution of four specific transitions. Other transitions were not considered since the sample size was not enough for statistical analysis. The turn angle distribution for the transitions between push and wrapped modes (Fig. 4.6C, and D) indicates that the bacteria switch from one to another with a reversal. As described earlier, the push bundle configuration has the unflagellated cell pole oriented in the swimming direction. In contrast, the wrapped swimmer has the flagellated pole upfront. Since the transitions between two flagellar configurations do not require any change of the cell body polarity, one can expect the reversal of the motion direction.

The histogram in Fig. 4.6A shows a narrow turn angle distribution with the mean angle, which is caused by pausing the motor rotation coupled with abandon one flagellum filament the bundle (Fig. 4.7A-C). In this case, the cell experienced brief stops when the flagellar bundle was pushing the cell body, whereas the swimming path was not changed after a stop

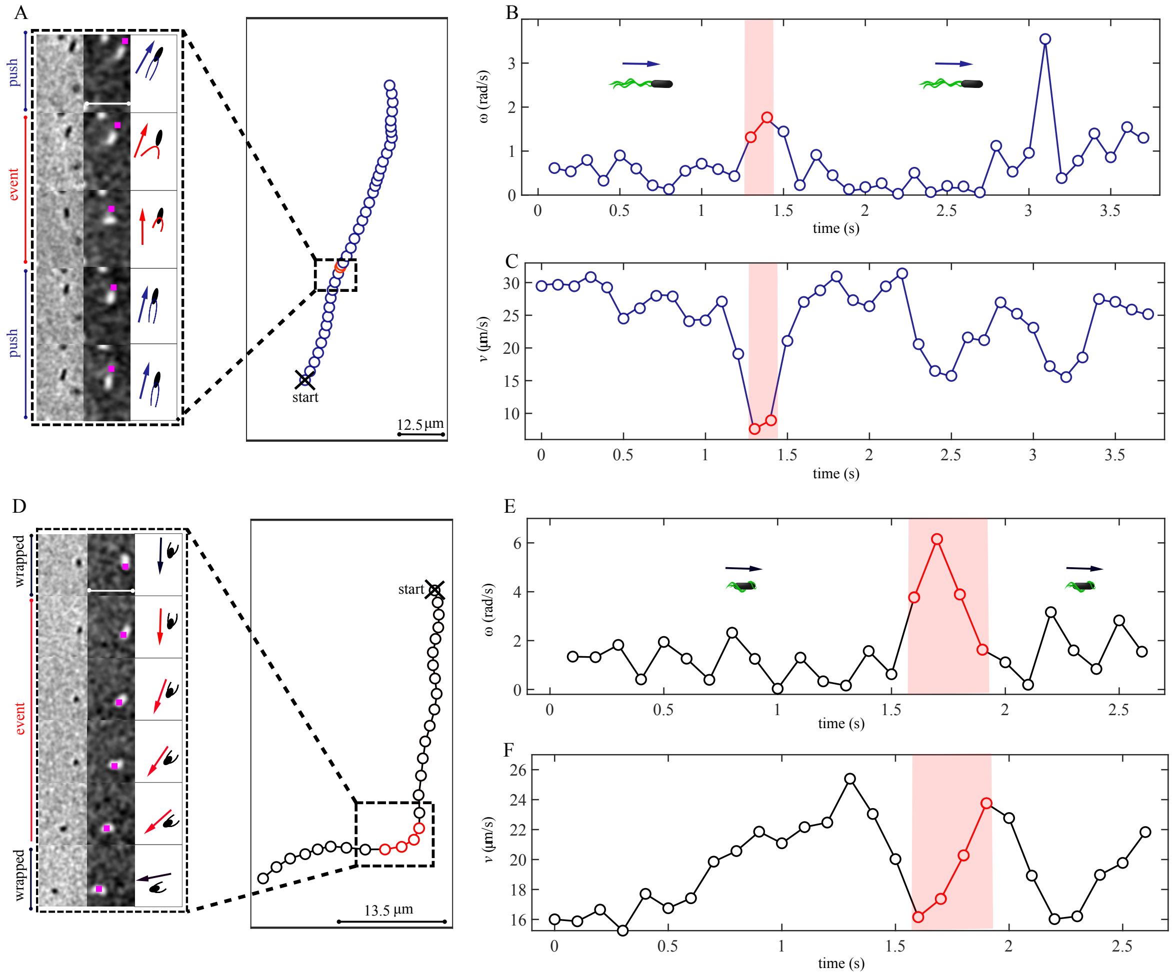

Fig. 4.7 Push and wrapped runs interruptions (A) Raw data, corresponding to the rectangular inset of the trajectory, displays the bundle transition while the motor stopped the rotation. The left handed panel indicates that the pusher cell slowed down and the bundle made the polymorphic transition for a short amount of time ($< 0.05\,\text{ms}$). After that, the flagella bundle formed and pushed the cell body for the rest of the time (see also Movie S4). (B) Rotational velocity ω of the track are in the range of $0-4\,\text{rad/s}$. (C) Corresponding speed v data of the stop event shows a abrupt slowdown, started at time 1.3 s. (D) Trajectory with a wrapped mode. Track interrupted with an event by an angle $\psi \simeq 90°$. The raw images of the selected trajectory data points suggest that although the flagellar bundle configuration did not changed, the cell reoriented (see also Movie S5). Taken from [104].

event. The bundle disassembly caused a speed drop, which was the reason corresponding data points categorized as an event (red data points on 4.7C). Leaving a filament from the coherent bundle might be the reason of this type of event. The raw image panel of Fig. 4.7A demonstrates the bundle instability during the stop phase (bundle marked in red). As previously stated, the tumble event in *E. coli* is the consequence of changing the rotation direction of at least one flagellum in the bundle (from CCW to CW). The rotation direction reversal brings the filament out of the bundle. The stop event in push mode is significantly more similar to the tumble in the sense of bundle instability. The only difference is the turn angle distributions; although the tumble event leads a broad range of turn angle distribution, by the stop events during push mode, cell reorientation was restricted with small angles due to the narrow turn angle distribution.

On the other hand, the turn event during wrapped mode could display different properties. The wrapping mode interruption made a broad range of turn angles 4.6B). Figure 4.7D-F is a trajectory example of changing the direction while the flagellar bundle configuration was in the wrapped mode. The selected raw data on the right panel does not show any altering bundle configuration (Fig. 4.7D).

We investigated the run speeds of the population which was defined by $V_r = \frac{\Delta x_r}{\Delta t_r}$. The histogram in Fig. 4.8A shows two sub-groups, one for wrapped runs and one push runs. On average, the push runs were two times faster than the wrapped runs, with the mean run speed of $< V_{r,push} >= 25.2 \pm 9.4 \mu\mathrm{m/s}$ and $< V_{r,wrap} >= 12.5 \pm 6 \mu\mathrm{m/s}$. Furthermore, the push distribution is wide and included a broad range of speeds.

4.4 Summary and discussion

The combined microscopy set-up provides a strong method to find out the characteristic swimming properties of *P. putida*. Compared to the statistical analysis of *P. putida* done by Theves. et al [14], we were able to split the analysis based on the flagellar configurations. Our results show that the push and the wrapped modes were the most observed swimming modes in the population. Moreover, the pull mode is a rare configuration which is in contrast to the observation reported in Ref. [15]. In fact, the actual purpose of Ref. [15] was to report the swimming modes of *P. putida* for the first time, rather than an actual quantitative description of motility parameters. In term of experimental set-up, the investigation in Ref. [15] was done by high temporal/spatial resolution microscopy with 60x/100x objective and frame-rate of 100-400 fps. Using the high temporal resolution feature allowed the researches in Ref. [15] to present the complete picture of *P. putida* motility tactic in term of flagellar

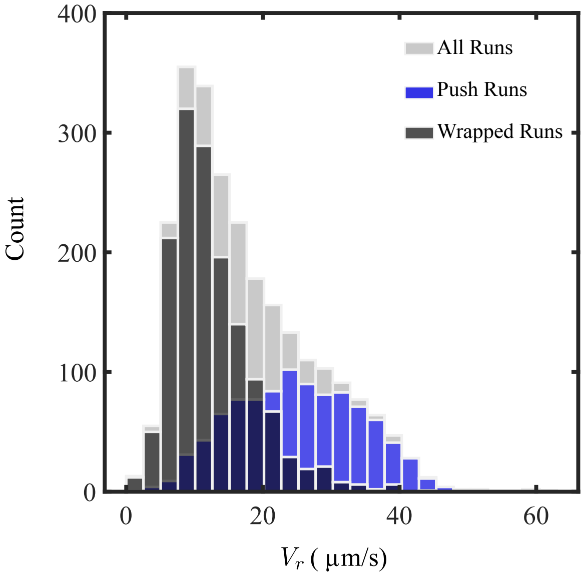

Fig. 4.8 Frequency distributions of run speed. Distributions are built from 2487 runs in total (grey histogram), 969 runs for the push sub-group, and 1472 runs for the wrapped sub-group.

bundle configuration during run modes and also the detailed description of the flagella bundle dynamics during the possible transitions, e.g. polymorphic state of flagella. However, it generated massive amounts of image data which made that impossible to track the single cells. In current study, we were able to track and analyze the cell trajectories with the automated event detection method. This indicates that the total fraction of run states in Ref. [15] could be increased by event detection, and be the explanation of observing the different percentage of run states in these two studies.

Furthermore, The bundle transition analysis illustrated that the reversals were caused by the bundle transition from wrapped to push and vice versa. Moreover, the stop event during push mode did not influence the direction of the motion; The reorientation angle in this case is $|\psi_{pp}| \sim 0°$. However, the wrapped mode interruption caused the broad reorientation angle distribution with a peak close to the $|\psi_{ww}| \sim 60°$. This might arise from the geometry of the bundle in wrapped mode.

The run speed of the push mode is two times larger than the wrapped mode on average. This suggested that *P. putida* motors structure may have various features in each mode which require more investigation. *Pseudomonas aeruginosa*, another bacterium of the *Pseudomonas* family, has more complicated motor configuration than *E. coli*. It has five different genes (motA, motB, motC, motD, and motY) which are known to be required for motor function [108]. Doyle et al. in Ref. [108] studied the contribution of those genes on the motility of *P.*

aeruginosa. The analysis of mutants showed that torque generation by MotA/B/Y or MotC/D is enough to promote motility in liquid; however, MotA/B/Y units are essential for movement in viscous environments. They suggested that the more complex torque generating system in *P. aeruginosa* is essential for a polarly flagellated bacteria to solve the problem of motility in the presence of increasing external load. While the peritrichous bacteria, such as *E. coli*, solve the problem by up-regulating the number of propellers [108]. Different properties of *P. putida* swimming modes may originate from the architecture of the motor, which requires additional studies to reveal the motor architecture in *P. putida*.

Chapter 5

Swimming near-surface

5.1 Introduction

This chapter is focused on a research conducted with *P. putida* near a solid boundary. *P. putida* is a soil bacterium and evolves in the presence of solid boundaries. Living in complex environments, such as soil, needs flexibility to pass through the micro labyrinths, in where swimming via flagella mediate motility could be a big challenge [109]. In their everyday life, *P. putida* interacts with the nearby boundaries/surfaces. Their complex swimming strategy could be affected by the boundary in various ways. Knowing *P. putida*'s swimming characteristics close to a solid surface can shed light on the hydrodynamic interactions between different flagella configurations and the boundary.

A solid surface and more commonly confinement influences the motility dynamics of flagellated swimmers significantly. The first aspect is the distance (from the surface) dependence of the swimming speed. When bacterium swims near a surface, the larger drag force causes decreasing the swimming speed [110]. The second type of surface-influence on the swimming is a circular trajectory nearby a surface (see also section 2.2.2). Swimming in the circle of *E. coli* near-surface was observed both in wild type and smooth-swimming cells (non-tumbling mutant) [66, 111]. Although wild-type cells moved away from the surface more frequently, smooth-swimming cells swam in the circle for a longer time than wild type. It shows that the tumble events is a mean to escape from hydrodynamics effect of the solid boundary. Other bacterial species are influenced by the surface differently. *V. alginolyticus* is known to switch between forward (CCW motor rotation) and backward (CW motor rotation) swimming modes. Qualitative differences between forward (push mode) and backward (pull mode) are found. The average backward swimming speed is detected 1.5 times greater

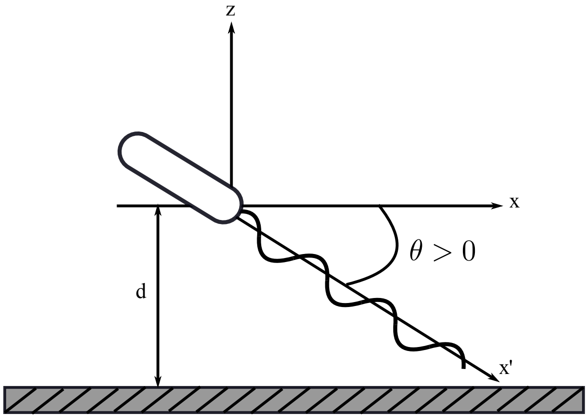

Fig. 5.1 Boundary element model of a bacterial cell at a distance (d) from a solid boundary. The coordinate systems xyz and the pitch angle, θ are shown. Taken from [114].

than the forward [112]. Also, the cell traces near the surface are composed of straight and curved sections [113]. During pull mode, the cell swam in a circular arc, while the track during push mode progressed linearly. A numerical study by Goto et al., [114] showed that the backward swimming is unstable close the solid boundary. In this study, an influential factor to the difference between the forward and backward motions was the orientation of the cell concerning the wall. The calculation were performed by changing the pitch angle θ and the distance from the wall boundary d (Fig. 5.1). When a cell swim parallel to the surface $\theta = 0$. If the cell swims with the flagellum close to the wall and the cell body away from it $\theta > 0$. Finally $\theta < 0$ is the opposite way around. The numerical calculation of the motion indicated that the forward swimmer tended to maintain a fixed distance from the wall, because its pitching motion was stable; the cell body interaction with the wall increased the pitch rate, and the flagellum interaction with the wall decreased the pitch rate (those two motions acted opposite each other, which led to the stability of the pitch motion). On the other hand, the pitch motion of the backward swimmer was unstable. It means that the backward motion was either approaching the surface (pitch angle θ is positive) or departing (pitch angle θ is negative) from it. For departing motion in backward swimmer, the cell steadily increased its distance from the wall. It swam almost in a straight line close to the wall. However, the approaching motion in backward swimmer is a circular motion, which was the consequence of the flagellum interaction with the surface. These representations may be confirmed if the pitch angle is available experimentally along with trajectory. Recent experimental studies by Ref. [115, 116] reported the pitch angle of *E. coli* near-surface. The investigation indicated that *E. coli* circulated close to the boundary with the cell body pointing to the surface (“nose-down”), in contrast to the numerical study explained above. It is still unclear why the pusher *E. coli* has a circular trajectory near the solid boundary, while *V. alginolyticus* has not. One explanation could be that the ratio of the cell body to flagellum size is an important parameter to stabilize the track close to the boundary. Here, we investigated the hydrodynamics interaction with the solid boundary in case of *P. putida* with multi flagella bundle configuration. The following section describes the experimental finding of the near-surface behavior of *P. putida*.

5.2 Materials and methods

The *Pseudomonas putida* KT 2240 $FliC_{S267C}$ strain was cultured overnight in 50 ml Tryptone Broth (TB) (10 g l^{-1} tryptone (Applichem), 5 g l^{-1} NaCl) being shaken at 300 rpm, and 30 °C. The overnight cell culture with highly motile bacteria was washed once by centrifugation (4000 rpm, 4 min, room temperature), followed by gentle resuspension of the pellet in 500 µl MB+. The cells were then labeled with Alexa Fluor 488 C5-maleimide. The fluorescent labeling was explained in chapter 4.1. 300 µl of the cell suspension was filled in a ibidi μ-Plate 96 Well (see Fig. 5.2 for the physical dimension of the well). The plate stayed for 10 minutes in a stationary position to diminish the flow drift. After that the cells were visualized in the plate using an IX71 inverted microscope equipped with a 20X UPLFLN-PH objective (both Olympus, Japan) and an Orca Flash 4.0 CMOS camera (Hamamatsu Photonics, Japan) together with TriggerScope. The image stacks were acquired at 20 fps. The field of the view was placed 5 µm above the bottom of the well. Total height of the well was 12.9 mm.

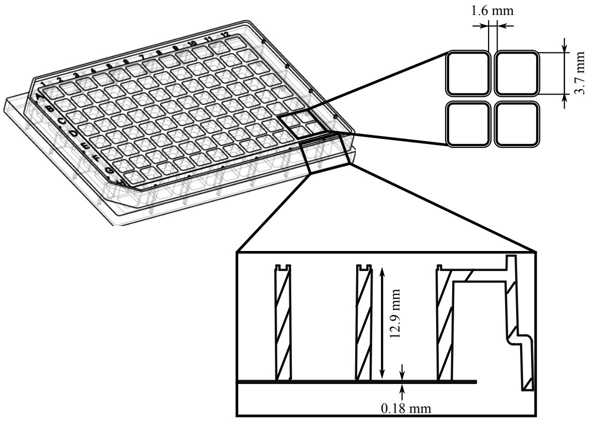

Fig. 5.2 Layout of the ibidi μ-Plate 96 Well. Each plate contains 96 wells with the dimension shown in the figure. Adapted from [117].

5.3 Experimental results

As mentioned before, the focal plane of the microscope was located 5 μm above the glass bottom of the well. The cells were monitored from below in XY plane. That is the reason we were not able to have the pitch angle of the cell. When the cells approached 5 μm above the well bottom, some of them remained in the microscope focal plane. Accordingly, 1320 trajectories were recorded at that depth and statistically analyzed. Figure 5.3 shows a typical trajectory of *P. putida* swimming pattern near-surface, which is not the same for those observed for *E. coli* [65, 66]. However, the track has a similarity with the near-surface trajectories of *V. alginolyticus*. The cell swam in a circle when the flagella bundle pushed it. After switching to the wrapped mode, the trajectory became a straight run. This implies that the near-surface hydrodynamic interaction influences two run modes differently; when the cell was in push mode, it swam in circle as a consequence of the surface-induced torque (for more detail see the 2.2.2), however the wrapped mode was not affected. Due to earlier study [15] and our finding, the stop events during push mode happen when one filament leaves the coherent bundle. In some turn events in a circular motion, this kind of bundle disassembly occurred; the push bundle was clearly dissembled. The raw images display how the flagella bundle changed their configuration in the circular part of the trajectory (Fig. 5.3A, top panel). In section 3.7, we described how the runs and events were categorized heuristically. The

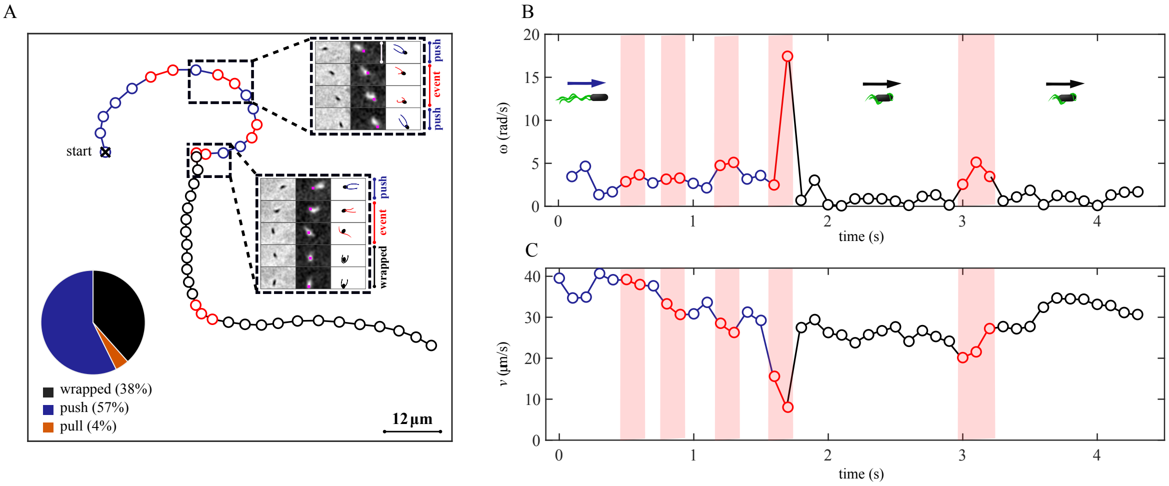

Fig. 5.3 Typical *P. putida* trajectory near-surface. (A) Cell circulated with the push bundle. The push run interrupted three time, one with the flagella bundle disassembly, the corresponding raw data are displayed in top rectangular box. Then, the flagella bundle switched to the wrapped mode. The pie chart exhibits the percentage of the runs (N=2533) which were observed in the near-surface experiment. (B) and (C) are the time series of rotational velocity ω and swimming speed v, respectively.

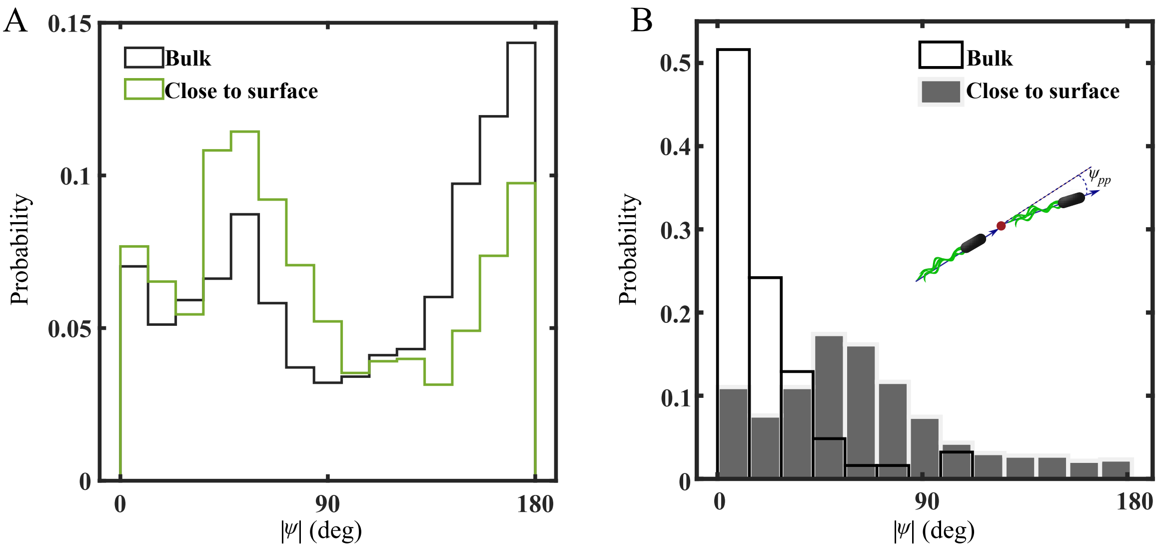

Fig. 5.4 The analysis is based on near-surface experiment. (A) Comparison of the overall turn angle distribution of the tracks near-surface in green and the bulk in black (taken from Fig. 4.3A). The green distribution was built from 1303 turn angles. (B) Turn angle distribution of the push-push transition. The distribution was built from 643 turns.

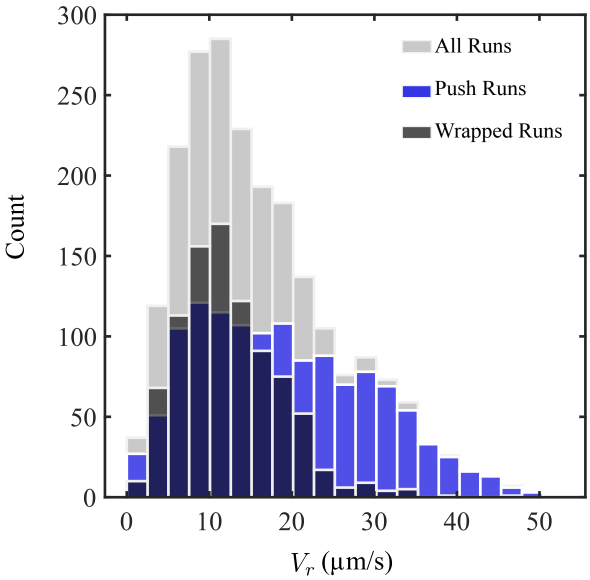

Fig. 5.5 Frequency distributions of run speed of the near-surface assay. Distributions are built from 2177 runs in total (grey histogram), 1277 runs for the push sub-group, and 900 runs for the wrapped sub-group.

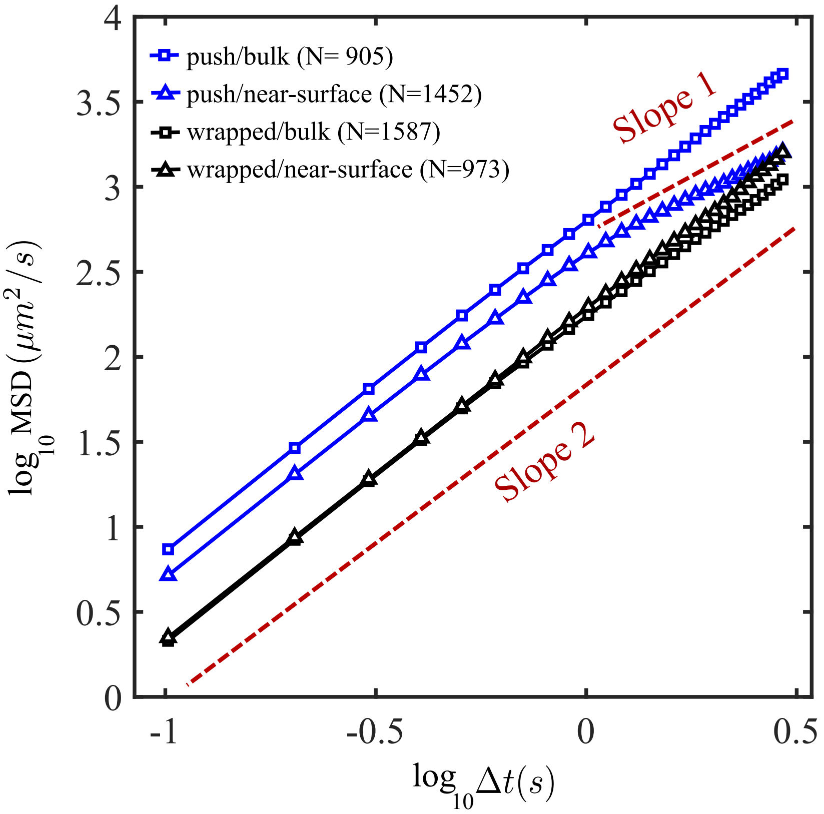

Fig. 5.6 Temporal evolution of the mean square displacement (MSD) for different run modes in bulk and near-surface experiments. The MSD for the bulk and near-surface data sets are shown by squares and triangles, respectively. Each curve includes information from at least 2000 runs.

events are identified by sudden change in speed or angular velocity. The events detected in the circular motion of the Fig. 5.3 were mainly classified based on increasing the angular velocity.

The statistical analysis overall population displays the difference between the near-surface and the bulk swimming characteristics. The turn angle distribution for the near-surface population indicates that the peak at $\sim 60°$ is more pronounced than in the bulk (Fig. 5.4). The turn angles in Fig. 5.4 were taken from all the possible transitions. The bulk turn angle distribution was adapted from Fig. 4.3A for better comparison. By looking at the turn angle distribution for all the possible transition scenarios, the only transition that had a different distribution shape than the bulk population is the push-push transition (Fig. 5.4B). Because of their similarity to the bulk analysis, the distributions for the other transitions were not shown. As described in section 2.2.2, the surface-induced torque constantly changes the swimming direction to maintain swimming path in a circle. The bulk results shows us, the

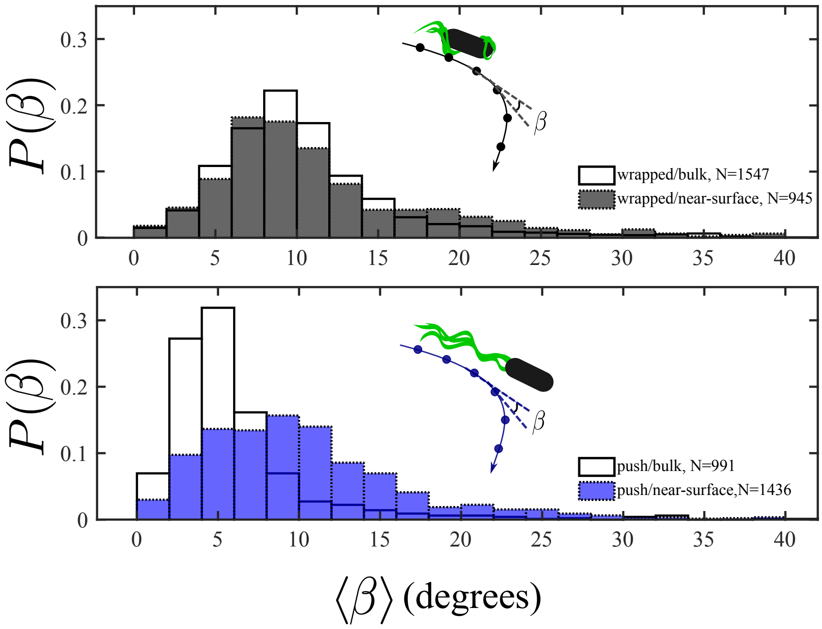

Fig. 5.7 Relative angle of motion distributions. The colorless histograms are the relative angle of motion from the bulk experiment. The blue and black histograms are from the near-surface experiment.

disassembly of the flagella bundle could not effect the straightness of the push runs. That is the reason the push-push transition on average has a turn angle $\sim 0^\circ$ in the bulk. The surface-induced torque caused the cells in push mode reoriented slightly in order to stay in the circular track. The run speed distribution shapes are similar to bulk experiment (Fig. 4.8), expect for the push runs (Fig. 5.5). The distribution of the push runs speed in Fig. 5.5A, shows that the peak is around 10 μm/s, which is reduced considerably in comparison to the bulk.

Next, we quantified the mean square displacements (MSD) of *P. putida* for the push and the wrapped run modes from tracking data, as shown in Fig. 5.6. The MSD curve of the three data set – push in bulk, wrapped in bulk, and wrapped near-surface – shows the ballistic motion with the slope of ~2. Only the push near-surface data set displays a reduction to slope ~1 at longer run times ($> 0.2\,$s). At that time scale the behavior was diffusive. The near-surface data sets indicate that the push runs randomized faster because of the circular motion.

Distribution of relative angles of motion between successive time intervals of the trajectories can probe the dynamics of the cells near-surface as well [118]. Each track contains a set of positions of the cell centre of mass X. Given these data, one can form the vectors that connect positions separated by τ steps, $V(t;\tau) = X(t+\tau) - X(t)$. The relative angle $\beta(t;\tau)$

is the angle between $V(t;\tau)$ and $V(t+\tau;\tau)$ via

$$\cos\beta(t;\tau) = \frac{V(t;\tau)\cdot V(t+\tau;\tau)}{|V(t;\tau)||V(t+\tau;\tau)|}. \tag{5.1}$$

Indeed the parameter τ is a lag time. Figure 5.7 is the β distribution for the lag time of $\tau = 0.1$, which is the time delay between two consecutive positions of the trajectories. The wrapped mode (Fig. 5.7. lower panel) has a same shape of the distribution of relative angles of motion $P(\beta)$ in both bulk and near-surface experiments. On the other hand, the distribution for the push mode in bulk (Fig. 5.7. Downer panel) shows a strong peak around $\sim 5^\circ$ which denotes straighter runs on average than the wrapped mode. However, the near-surface push run data set displays a similar distribution as calculated for the wrapped mode.

5.4 Summary and discussion

From the experiment conducted above it is evident that the different run modes interact differently with the nearby boundaries. The initial attempt was to analyze the run modes to find their hydrodynamics interaction when they faced the nearby boundary. Since the trajectories were captured in the XY plane, we were not able to check the cell and flagella bundle alignment with the surface. However, the trajectories statistical analyzes pointed out the asymmetry for different run modes. The turn angle distribution for the *P. putida* near-surface (Fig. 5.4) displays more pronounce peak around $\sim 60^\circ$. Analysing the turn angel distribution for push-push transition indicated that the peak shifted from $\sim 0^\circ$ to $\sim 60^\circ$ in near-surface boundary. However, the turn angle distribution for the other transitions was not influenced by the boundary. Furthermore, the run speed distribution of push mode demonstrated the peaks at $\sim 10\,\mu\text{m/s}$ for both push and wrapped runs near a surface, which is a considerable reduction in push mode; the push mode in bulk had a peak at $\sim 20\,\mu\text{m/s}$ as shown in Fig. 4.8A. In conclusion, the push mode, which is the faster mode in general, slowed down near-surface while the wrapped mode was not affected. The distance dependence of the cell speed was reported before [110]. The other feature of the push mode near-surface extracted from the MSD curves (Fig. 5.6). The MSD curves were calculated for the push and wrapped run modes. The runs in push mode near a surface shows a transition from ballistic to diffusive regime at times longer than 0.2 s. This behaviour were not detected for the other data sets. Eventually, the relative angle of motion distributions of consecutive data points along the runs verified that the push runs became curved near the surface boundary.

Even though we were not able to measure the pitch angle of *P. putida* near surface, the 2D trajectories revealed essential features of the cell dynamics near the boundary. Based on our experimental findings, *P. putida* also showed asymmetry for different run modes when it encountered to the surface. The push run mode was affected by the surface and made the arc part the *P. putida* trajectories. However, wrapped mode did not show any interaction with the surface. Swimming in a circle near-surface was reported earlier for *E. coli* [66, 111] and *V. alginolyticus* [113]. *E. coli* switches to the circular tracks at the whole time of runs, while *V. alginolyticus* has both straight and arc runs near the boundary. *P. putida* and *E. coli* have the arc part of trajectories when their flagella bundle pushes the cell body. In contrast, the circular motion in *V. alginolyticus* occurs when the flagellum pulls the cell body[1]. Both *P. putida* and *V. alginolyticus* are multi-mode swimmers, and just one of their run modes makes the arc part of trajectories. Those information suggested that the geometry of the bacterial cells may play an important role in this matter. Definitely, We need more theoretical study to address the question of how the same behavior, the circular motion, was established in different bacteria species with various geometry properties. Moreover, the complementary experimental investigation on the pitch angle of the push mode closes the surface will clarify the reason behind this phenomenon.

---

[1] In contrast to the *E. coli* with only one type of flagellum (H^+-driven type), *V. alginolyticus* has two types of flagella: a single polar flagellum (Fla, Na^+-driven type) and many lateral flagella (Laf, H^+-driven type). The researcher in Ref. [113] utilized two mutant strains, YM42 (Fla$^+$ Laf$^-$) and NMB102 (Fla$^-$ Laf$^+$) [119]. Ym42 strain was biased to forward swimming and did not have any lateral flagella. However, NMB102 did not have polar flagellum and was considered as the strain which was biased to backward swimming. The direction of the flagella was not visualized for all trajectories, because of the imaging techniques. For that reason, the terms forward and backward were pointed to the trajectory properties; the curve parts of the tracks were considered as backward motion and the straight parts were categorized as the forward motion.

Chapter 6

Chemotaxis

6.1 introduction

The best-understood model organism *E. coli* alternates the run duration to achieve the region with a high concentration of nutrition by increasing the probability of the longer runs toward the nutrition source and decreasing the probability of the tumbling [2]. In fact, *E. coli* modulates the CCW and CW intervals to external chemical cues. The cell increases the time duration of CCW motor rotation, run mode, to purposefully navigate toward the chemoattractants, and the motor reversal, CW rotation, causes reorientation. The chemotaxis signal transduction network inside the cell regulates the run and tumble probability. Any changes in the environment transmits into the cell with the chemotaxis signal transduction network. The information transmission yields activation/deactivation of CheY proteins. The chemoattarchtant deficiency actives CheY through phosphorylation. Consequently, CheY-P binds to flagellar motor which increases the possibility of CW rotation. Multiple flagella of *E. coli* synchronously rotate CCW in run phase, and CW rotation of at least one flagellum triggers the bundle disassembly and reorientation. Therefore, *E. coli* regulates its response to the environmental cue via controlling the likelihood of flagella rotating CCW or CW. The genes controlling chemotaxis in *E. coli* are homologous to the other bacterial species that suggest a similar core chemotaxis signal transduction network among the bacterial species (for more details see also 2.4.1).

There are plenty of single polarly flagellated bacterial species, i.e. *Shewanella putrefaciens*, *Pseudoalteromonas haloplanktis*, and *V. alginolyticus*, which have run and reverse motion. In contrast to *E. coli*, both CCW and CW motor rotation establish a persistent random walk. The chemotactic behavior of those rely on a combination of several run modes much less is known. Xie et al.'s paper [7] raises the important feature of chemotacic response of *V. alginolyticus*. In a chemically homogeneous medium, no correlation observed for the forward and backward swimming times. However, the forward and backward swimming times correlated strongly near a point source of attractant. The study indicated that *V. alginolyticus* had shorter forward swimming time in presence of chemoattractant gradients. The research suggested that one run mode, forward runs, effected more in the presence of stimuli, which may indicate the gradient sensing in multi-mode swimmers has been evolving in only one specific run mode.

This chapter primarily investigates the response of *P. putida* and *E. coli* to the gradient of nutrition. Firstly we will discuss our finding of *E. coli* chemotaxis in a combination of theoretical study. The theoretical approach introduces a stochastic model for *E. coli*'s run-and-tumble random walk. Afterwards, we will discuss our novel results of the *P. putida* chemotaxis strategy. Our model study *P. putida* is also a multi-mode swimmer with run and reverse swimming tactic. It has three run modes with various sense of motor rotation; CCW rotation of the all flagella in push mode and CW rotation of the all flagella in wrapped and pull modes. We examined *P. putida* response to stimuli using our combined phase–contrast and fluorescence imaging. The microscopy set-up enabled us to investigate individual run mode response in a linear chemoattractant gradient. Relying on *P. putida* as an example, we evaluated the role of one specific run mode in bacterial chemotaxis and, at the same time, shed light onto the chemotaxis strategies of multi-mode swimmers beyond the classical paradigm of *E. coli*. Based on the data set produced by the combined imaging set-up, we proposed an active particle model for bacteria with the multi-mode motility tactic that provided us to bridge the gap of experimental short-time observations and chemotactic motion in the long-time limit. Besides, it presented the basis for a significant evaluation of the efficiency and robustness of chemotaxis strategies of bacteria with multi-mode motility, both in bulk and in disordered environments. The findings presented in section 6.4 have been published in Ref. [104].

6.2 Material and methods

6.2.1 *E. coli* in linear gradient

Experimental set-up

*E. coli*AW405 strain was cultured overnight in liquid Tryptone Broth (TB) ($10\,\mathrm{g\,l^{-1}}$ Difco Bacto$^{\mathrm{TM}}$-Tryptone and $5\,\mathrm{g\,l^{-1}}$ NaCl) at $37\,^{\circ}\mathrm{C}$ on a rotary shaker at 300 rpm. The cell suspension was diluted 1:100 into fresh TB, and grown to mid-exponential phase (OD_{600} = 0.5). Then the bacterial suspension was washed and resuspended in MB+. Afterward, the cell suspension was divided into two fractions. One was centrifuged and resuspended in the same motility buffer (chemoattractant-free cell suspension), and the other was centrifuged and resuspended in motility buffer supplemented with the chemoattractant α-methyl-aspartate (Sigma-Aldrich, USA) in a final concentration of 0.5 mM (chemoattractant-containing cell suspension). In both cases, the final OD_{600} of the cell suspensions was 0.07 before filling them into chemotaxis chambers (Fig. 4.1).

Image analyzing and cell tracking

A custom Matlab program based on the Image Processing Toolbox (version R2015a, The MathWorks, USA) was used to process the image sequences automatically. For each image sequence, a background image was calculated by pixel-wise time average projection. It was subtracted from each frame to eliminate non-motile objects and shading effects. The built-in Matlab function *imerode* was then applied for morphological erosion (with a disk of radius 0.6 µm) to reduce the background noise. The putative bacterial cells are distinguished from background using the maximum entropy thresholding algorithm by Kapur et al. [99]. The threshold was calculated for each image in the sequence separately. The median of all threshold values was used to segment the whole sequence. The binary images were further processed with the morphological operations, *imopen* and *imclose* (with a disk of radius 0.3 µm) to eliminate any noise caused by segmentation. The built-in function *bwconncomp* was used to find all connected objects in the binary images. Size and centroid of the objects were determined using the *regionprops* function. Afterwards, particles with an area between 1 μm^2 to 15.6 μm^2 were considered as single bacterial cell. Finally, trajectories were obtained employing the tracking algorithms by Crocker and Grier [100].

To avoid tracking artifacts caused by tumble events when cells enter and leave the focal plane, the first and last 0.5 s of each track were removed. Highly curved tracks as well as tracks with a total displacement $< 10\,\mu m$ were eliminated, as they most likely result from damaged flagella.

6.2.2 *P. putida* in linear gradient

Fluorescently stained flagella of *P. putida* was prepared as described in section 4.1. Subsequently, the cell suspension was allocated into two fractions. One was centrifuged and resuspended in the MB+ as the chemoattractant-containing cell suspension, and the other in MB+ supplemented with the chemoattractant casamino acids (Amresco) in a final concentration of 7 % (wt/vol) as the chemoattractant-free cell suspension. The cell suspensions were loaded into the chamber. The recorded image stack were processed as explained in section 3.4.

Both studies, *E. coli* and *P. putida* in linear gradients, were performed in the μ-Slide Chemotaxis 3D chambers in order to maintain a stable linear gradient of the chemoattractants (Fig. 4.1). For each chemotaxis assay, the cell suspension with chemoattractant was filled into the reservoir on the right hand side and the chemoattractant-free cell suspension into the reservoir on the left hand side. The central observation area was filled with motility buffer. A stable linear chemoattractant gradient is generated by diffusion in the observation area and maintained for several hours [120].

6.3 Chemotaxis response in *E. coli*

The information about the physical properties of bacterial motion obtains form the 2D trajectories. The tracks does not have any information about the flagella, therefore each swimming phase categorizes based on some heuristic run-and-tumble recognizer methods as an alternative way [81, 102]. For instance, the method introduced by Masson et al., in Ref. [102] is founded on significant changes in the speed and angular velocity time series; when cell tumbling swimming speed decreases, and angular velocity increases (see also section 3.4). These significant changes are detected on the basis of threshold parameters by an automatized tumble recognition algorithm. All the automated tumble recognizer methods require visual inspection of the trajectories for the accuracy of the tumble detection. In this section, we focused on a joint project published in Ref. [121]. In this study, the stochastic description of *E. coli* swimming motion was investigated in the presence of uniform and gradient chemoattractant source. The theory presented novel tools to distinguish run and tumble states of the bacterial motion beyond the classical tumble recognizer which was developed by Maximilian Seyrich in the Statistical Physics of Soft Matter and Biological Systems group of Holger Stark. In this section we will first describe the theory. Afterward, the trajectories analysis using the inference method will present in the uniform buffer solution and the linear gradient of a chemoattractant.

Statistical parameter inference

We describe the dynamics of bacteria in terms of Langevin equations

$$\dot{\mathbf{r}}(t) = v(t)\mathbf{e}(t), \tag{6.1}$$

$$\dot{v}(t) = r\,[v_0 - v(t)] + \xi_{\mathrm{sp}}(t) + q(t), \tag{6.2}$$

$$\dot{\Theta}(t) = \sqrt{2D_{\mathrm{rot}}(t)}\;\xi_{\mathrm{an}}(t)\,. \tag{6.3}$$

Here, $v(t)$ is the velocity of the bacterium in two dimensions, $\mathbf{e}(t) = (\cos\Theta, \sin\Theta)$ is the unit vector, Θ is the bacterium's orientation angle with respect to the x axis.

The equation for speed $v(t)$ has contributions from three sources: drift, diffusion, and jumps. The jump initiates the tumble at time t_i via a shot-noise process [122, 123]

$$q(t) = -\sum_{i=1}^{N^{\lambda}} \eta v(t)\delta(t - t_i), \tag{6.4}$$

which is a series of N^{λ} delta spikes (number of tumble events) with amplitudes η. The tumbles follow Poisson distribution and occur randomly with tumble rate $\lambda(t)$. At the beginning of each tumble, the bacterial speed is reduced by η to $(1-\eta)v_t$. During the tumbles the track speed drops down. In equation 6.2, r is the relaxation rate after a tumble event, where the speed relaxes towards the swimming speed v_0 of the run phase. Therefore r^{-1} is the mean duration of a tumble event. ξ_{sp} is a Gaussian white noise process that accounts for rotational thermal noise due to the ambient fluid, which is determined by $\langle \xi_{\mathrm{sp}} \rangle = 0$ and $\langle \xi_{\mathrm{sp}}(s)\xi_{\mathrm{sp}}(t) \rangle = \sigma^2\delta(t-s)$. Here, σ is the white noise strength. Eventually, five parameters $\{\lambda, r, v_0, \sigma, \eta\}$ determine the stochastic speed process. These full set of parameters are inferred from the moments $m_n^V = \langle v(t)^n \rangle$ of equation 6.2, where the average is taken over all times t and all tracks in the long-time limit, and also the speed autocorrelation function for the mode $g_V(\tau) = \langle [v(t+\tau) - m_1^V][v(t) - m_1^V] \rangle = \Delta^2 v e^{-(r+\eta\lambda)\tau}$.

Table 6.1 Inferred parameters for the stochastic processes of speed and angle for *E. coli* moving in a control experiment.

Speed		**Angle**	
λ	0.83 ± 0.04 s^{-1}	λ	0.84 ± 0.02 s^{-1}
r	4.41 ± 0.3 s^{-1}	r	3.81 ± 0.3 s^{-1}
v_0	20.8 ± 0.2 μms^{-1}	D_0	0.09 ± 0.002 s^{-1}
$\sqrt{\frac{\sigma^2}{r}}$	5.11 ± 0.07 μms^{-1}	D_T	2.31 ± 0.12 s^{-1}
η	0.85 ± 0.01		

The stochastic equation for the orientation angle Θ is described by the white noise term ξ_{an}. It is characterized by $\langle \xi_{\mathrm{an}} \rangle = 0$ and $\langle \xi_{\mathrm{an}}(s) \xi_{\mathrm{an}}(t) \rangle = \delta(t-s)$. In the model, $D_{\mathrm{rot}}(t)$ alternates between two values, D_0 and D_T. D_0 is the run status thermal rotational diffusion coefficient and, D_T is an enhanced value during tumble status. Overall, four parameters, $\{\lambda, r, D_0, D_T\}$, govern the stochastic process for the orientation angle. In order to find the full sets of parameters, the steady-state probability distribution $p(|\Delta\Theta|)$ form Eq. 6.3 is determined. The moments of the absolute angular displacement $m_n^{\Delta\Theta} = \langle |\Delta\Theta|^n \rangle$ together with the autocorrelation function $g_\Theta(\tau) \approx 1 - \alpha_\Theta \tau$ with a relaxation rate α_Θ are utilised to infers the parameters to control the directional dynamics.

Results

To perform the parameter inference, the moments from experimental trajectories are calculated and, fitted with the analytical solutions. The inferred swimming parameters are the tumble rate λ, the tumble time r^{-1}, the swimming speed v_0, the strength of speed fluctuations σ, the jump height η, the thermal value for the rotational diffusion coefficient D_0, and the enhanced coefficient during tumbling D_T (see table 6.1). The method is validated by comparing the inferred swimming parameters to their values determined by a heuristic tumble recognizer. For instance, the tumble rate determined with the heuristic tumble recognizer was $\lambda = 0.84\,\mathrm{s}^{-1}$, which shows a fair agreement to those obtained regarding our method. Afterward, the experimental data of *E. coli* in the gradient was investigated. The swimming parameters depend on the orientation or swimming angle θ were determined. The experimental data was split into 8 subsets, $\theta = 0, 2\pi$ means swimming up the gradient and $\theta = \pi$ in opposite direction. Figure. 6.1A shows the tumble bias λ/r, the ratio of tumble time to run time, as a function of the orientation angle. The ratio is lower when swimming up the gradient ($\theta = 0, 2\pi$), it means that the run time is dominated. The tumble bias had a maximum value when swimming down the gradient ($\theta = \pi$) which indicates that the tumble time increased more in comparison to the run time. The curves from angle inference and speed inference were displayed in orange and blue, respectively. They show the same trends even though they are executed independently from each other. The diffusion coefficient D_T during tumble displayed the same trend; it was improved when swimming in an unfavorable direction (Fig. 6.1A), which confirms the alternative chemotaxis strategy identified in Refs. [124, 125]. Overall, the results from the method introduce an approach to describe the motility of the bacterial swimmers beyond the classical run-and-tumble analyzers.

6.4 Chemotaxis response in *P. putida*

Experimental finding

The classical representative of bacterial chemotaxis strategy is the comparison of the probabilities of observation a run that is longer than a given time t, sojourn probabilities $s(t)$. Indeed $s(t)$ is the complementary cumulative distribution function (CCDF) of runs times. In simple terms, $s(t)$ is used to realize how often a random variable (run time) is above a particular level: $\mathrm{CCDF}(t) = s(T > t) = 1 - \mathrm{CDF}(t)$, where $\mathrm{CDF}(t)$ is cumulative distribution function.

In order to calculate the sojourn probabilities $s(t)$, the runs can be categorized into two groups conditioned on the run direction. Two subsets of the data were created that contained all runs oriented up or down the gradient direction. Figure 6.2 displays the sojourn probabilities $s(t)$ of *E. coli* in a linear of α-methyl-aspartate gradient. Due to *E. coli* classical chemotaxis strategy, runs in the direction of the gradient (blue) are longer than runs in the opposite direction (red), themselves longer than control runs (black) where no chemoattractant is present. Unlike *E. coli* with only one run mode, *P. putida* has a complex swimming maneuvering combination of three different run modes and two types of events. To elucidate how *P. putida* uses its multi-mode swimming pattern to navigate towards a source of chemoattractant, we imaged bacteria in a linear casamino acid gradient. In this

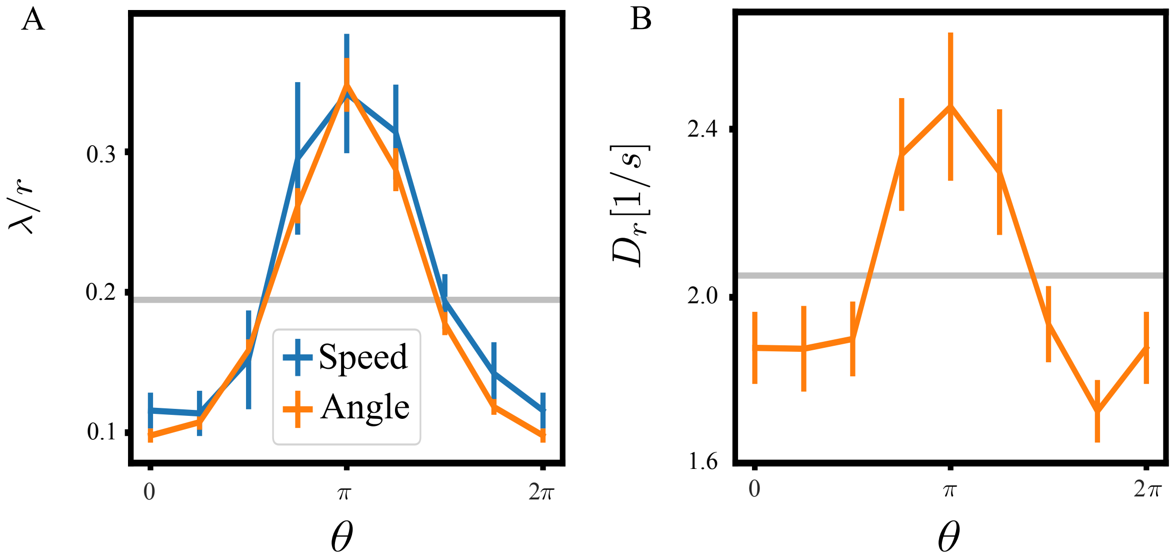

Fig. 6.1 (a) Tumble bias λ/r conditioned on the swimming angle θ. The bacterium navigates toward the gradient for $\theta = 0, 2\pi$, and backward for $\theta = \pi$. The tumble bias is determined either by angle inference in orange or speed inference in blue for *E. coli* in a linear gradient of (α-methyl-aspartate). (b) Rotational diffusion coefficient D_T during tumbling conditioned on θ. Tacken from [121].

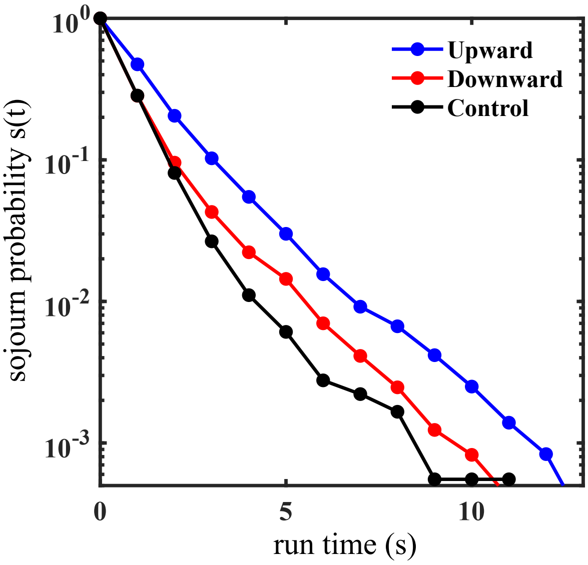

Fig. 6.2 Run-time bias of *E. coli* in a linear gradient of α-methyl-aspartate. Due to chemotaxis, runs in the direction of the gradient (blue) are longer than runs in the opposite direction (red), themselves longer than runs of control experiment (black). Each curve includes information from at least 1000 runs.

context, we classified the runs not only concerning the gradient but also based on the flagella bundle configuration. Runs in push and wrapped mode were analyzed separately (Fig. 6.3). Afterward, the sojourn probabilities $s(t)$ were determined for all four data sets (push and wrapped directed to and down the gradient). Figure 6.3 displays the results for the runs in push (A) and wrapped mode (B). The sojourn probabilities $s(t)$ were estimated based on a nonparametric maximum likelihood approach proposed in Ref. [127], which correctly takes incomplete runs into account as censored data (for more details please see appendix A). The wrapped mode demonstrated a clear run-time bias which obvious in a difference of the sojourn probabilities of up- and downgradient runs.

In other words, runs towards the chemoattractant source are longer, on average, than runs directed downward (see Fig. 6.3B). Surprisingly, run-time bias is not observed for runs in the push mode; the statistics of swimming time up and down the gradient are equal (see Fig. 6.3A). Therefore, the push and wrapped swimming modes response uniquely to the chemoattractant. Note that the push mode rotates CCW and wrapped CW [15]. Thus, the time that a flagella bundle rotates CW is affected by the chemoattractant, whereas the time of CCW rotation is not. The run-time statistics in a linear gradient compare to the control experiment revealed another feature of the *P. putida* chemotaxis strategy: while the sojourn probability of upgradient wrapped runs is identical to the control experiment, downgradient runs decrease (Fig. 6.3B). In contrast with the well-studied case of *E. coli* which extends

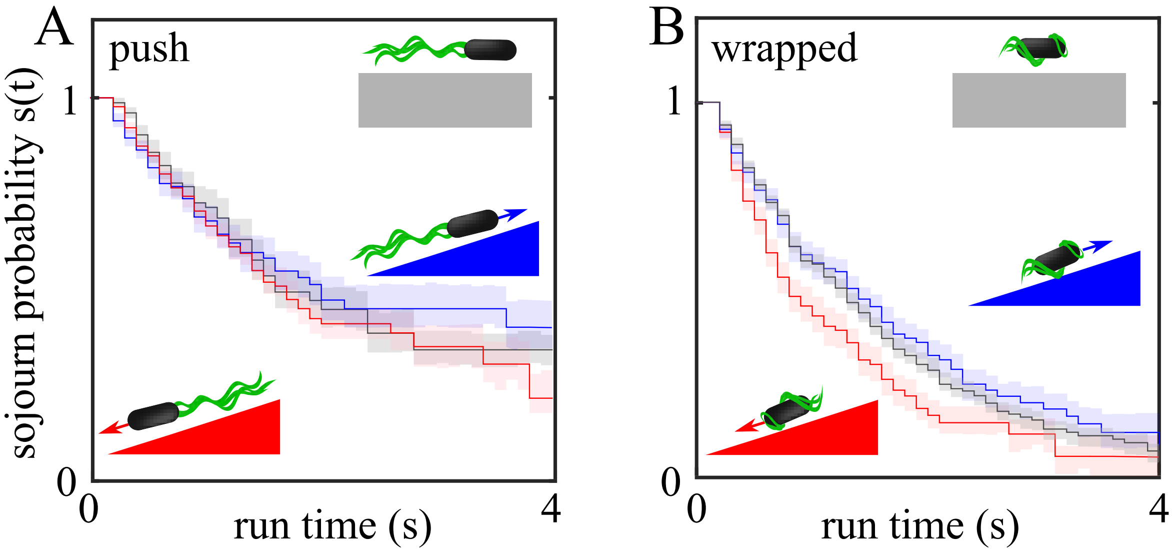

Fig. 6.3 Run-time bias of *P. putida* in a linear concentration gradient: the plots show the sojourn probabilities $s(t)$ that a run is longer than a given time t for runs in the push mode (A) and wrapped mode (B). Upgradient runs are shown in blue, downgradient runs in red. The control experiments in the absence of a gradient are plotted in gray for comparison. The error bars indicate the 1σ-interval estimated by bootstrapping [126]. The run-time bias depends on the swim mode: whereas the run-time statistics up- and downgradient is practically indistinguishable for swimming of the bacteria the push mode, there is a significant run-time bias in the wrapped mode: bacteria in the wrapped mode tend to decrease the downgradient run-time. Each curve includes information from at least 900 runs. Taken from [104].

their run duration when swimming in the direction of the chemical gradient (Fig. 6.2). The similar behavior to *P. putida* was reported for *V. alginolyticus* which displayed shorter forward swimming time in the presence of chemoattractant gradients [7], as mentioned in the introduction section 6.1.

Modeling active particles with multi-mode motility

In a joint effort with Robert Großmann, we propose an active particle model for the multi-mode swimmer *P. putida* based on the observed motility states and the statistics of the corresponding transitions between them. Theory development and modeling have been conducted by Robert Großmann. In the following, we will restate the theory to better understand the asymmetric chemotactic strategy of *P. putida*. The model demonstrates that the a given movement strategy of *P. putida* can be fully understood if the mutual interaction of the bacterial cells and disorder environment (e.g. soil) takes into account.

From the statistical analysis of the experimental data, we learned that the pull mode either is uncommon or short (duration is less than the delay between two frames, 0.1 s). Therefore,

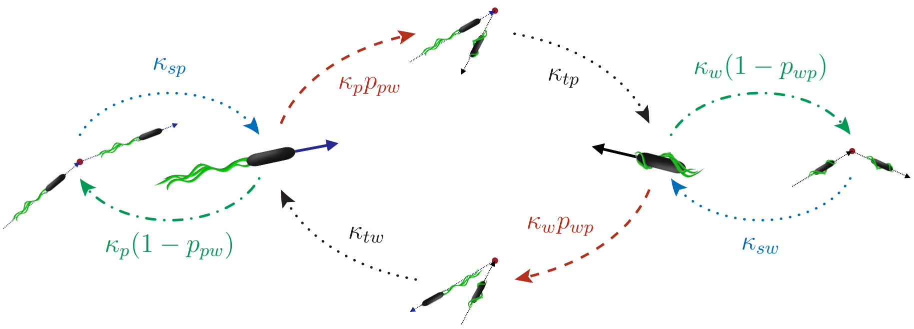

Fig. 6.4 Model representation of the motility pattern of *P. putida*: the two essential run states, push and wrap, are interrupted by stops of the flagellar driving or their reconfiguration with respect to the cell body inducing transitions from one run mode to another accompanied by turns. The mean duration of all states is parametrized by inverse transition rates that are denoted by κ_i. The parameter p_{pw} reflects the probability that the push mode is followed by the wrapped mode (and vice versa for p_{wp}). Taken from [104].

the pull mode is dismissed, and there are two essential run modes to take into account, push (p) and wrapped (w). The model included the following features:

- The swimmer has a characteristic speed, shown by v_p and v_w for push and wrapped mode, which are assumed to be approximately constant
- The persistence runs length is considered by rotational noise with the intensities D_p and D_w.
- The run, stop, and transition times are assumed to follow an exponential distribution (Poisson statistics), in a way that they are characterized by effective transition rates defined by κ_i. In fact, the rates κ_i captures the average number of events in time interval $[t, t+\Delta t]$ with the probability $\kappa_{p,w}\Delta t$ that a run ends within a time step Δt.
- The cell body does not displace spatially during stop and transitions.
- The turning events are described in terms of their probabilistic turn angle distributions (Fig. 4.6).
- The probabilities that a push (wrap) run is follow by a run in the wrapped (push) mode is defined by the parameters p_{pw} and p_{wp}.

The time evolution of bacterial dynamics in each states and the transitions between them are reflected in set of master equations. Since we assume that the run modes are distributed exponentially, the average push and wrapped run times are $\tau_p = 1/\kappa_p$ and $\tau_w = 1/\kappa_w$. In order to account the run times dependency with respect to the chemical gradient ∇c, the rates are coupled to the current direction of motion as follows:

$$\kappa_{p,w}(\mathbf{e}) = \lambda_{p,w} - \eta_{p,w}\left(\mathbf{e}\cdot\nabla c\right), \tag{6.5}$$

where the unit vector **e** denotes the direction of motion. Without a chemical gradient, the transition rates are obtained by $\lambda_{p,w}$. Here, $\eta_{p,w}$ are phenomenological parameters. These parameters could be obtained from a microscopic model for the signaling cascade which regulates flagellar motor reversals. In fact, $\eta_{p,w}$ is the response function explained in the section 2.4.3. Since we do not discuss the chemotaxis pathway in this study, $\eta_{p,w}$ considered as a parameter. When the cell swims upgradient, the corresponding transition rates decrease for $\eta_{p,w} > 0$, the cell should keep swimming in same direction instead of reorienting. From the experimental results, we observed $\eta_p \ll \eta_w$, (Fig. 6.3). Subsequently, the question raised here about weather this specific run-time bias is the optimum tactic or not for the long-time chemotactic response of multi-mode bacterium. We addressed this question by reducing the full dynamics to a Keller-Segel-type equation [128] for the particle density ρ through a mode expansion in order to derive long-term transport properties analytically,

$$\partial_t \rho \simeq -\nabla\cdot\left[\mu\left(\nabla c\right)\rho\right] + D\Delta\rho, \tag{6.6}$$

where D is the long-time diffusion coefficient and the average chemotactic drift velocity is provided by $\mathbf{v}_d = \mu\nabla c$. Here μ is the effective transport coefficients. Both μ and D

Table 6.2 The table summarizes the mean values of model parameters as they were estimated from experimental data.

model parameter	**estimated mean value**
D_p	0.03 s^{-1}
D_w	0.13 s^{-1}
v_p	25 $\mu m\mathrm{s}^{-1}$
v_w	13 $\mu m\mathrm{s}^{-1}$
λ_p	0.3 s^{-1}
λ_w	0.4 s^{-1}
p_{wp}	0.42
p_{pw}	0.75
$\langle\cos\psi\rangle_{pp}$	0.9
$\langle\cos\psi\rangle_{pw}$	-0.9
$\langle\cos\psi\rangle_{wp}$	-0.9
$\langle\cos\psi\rangle_{ww}$	0.55

are functions of the underlying motility pattern. The derivation of the effective transport properties from a descriptive model of the motility enables up to predict the chemotactic response. Here, we will discuss the chemotactic drift coefficient μ in terms of efficiency and robustness of *P. putida* chemotactic performance. Due to first order in the chemoattractant gradient ∇c, the chemotactic drift is identified with the *chemotactic responses* $\mu_{p,w}$ via

$$\mu = \mu_p \eta_p + \mu_w \eta_w. \tag{6.7}$$

μ_p (μ_w) is the *chemotactic response* due to a potential run-time bias in the push (wrapped) mode. The corresponding *chemotactic responses*, are given by

$$\mu_p = \frac{P_p}{d} \cdot \frac{v_p \mathscr{D}_w \left[1 - \Gamma_{pp}\left(1 - p_{pw}\right)\right] - v_w D_p p_{pw} \Gamma_{pw} - v_p \Gamma_{pw} \Gamma_{wp} \lambda_w p_{pw} p_{wp}}{\mathscr{D}_p \mathscr{D}_w - \Gamma_{pw} \Gamma_{wp} \lambda_p \lambda_w p_{pw} p_{wp}}, \tag{6.8a}$$

$$\mu_w = \frac{P_w}{d} \cdot \frac{v_w \mathscr{D}_p \left[1 - \Gamma_{ww}\left(1 - p_{wp}\right)\right] - v_p D_w p_{wp} \Gamma_{wp} - v_w \Gamma_{pw} \Gamma_{wp} \lambda_p p_{pw} p_{wp}}{\mathscr{D}_p \mathscr{D}_w - \Gamma_{pw} \Gamma_{wp} \lambda_p \lambda_w p_{pw} p_{wp}}. \tag{6.8b}$$

where P_p and P_w are the probabilities to find a bacterial swimmer in the push or wrapped mode in the stationary state, respectively. d is the dimension of the motion, which is two ($d = 2$) for the self-propelled motion. The indices ij correspond to a transition from state i to j. $\Gamma_{ij} = \langle \cos \psi \rangle_{ij}$ () and the effective rotational diffusion coefficients are defined by

$$\mathscr{D}_p = D_p + \lambda_p \left[1 - \Gamma_{pp}\left(1 - p_{pw}\right)\right], \tag{6.9a}$$

$$\mathscr{D}_w = D_w + \lambda_w \left[1 - \Gamma_{ww}(1 - p_{wp})\right]. \tag{6.9b}$$

Using the abbreviations introduced above, here we introduced the effective diffusion coefficient

$$D = \frac{1}{d} \cdot \left[P_p \cdot \frac{v_p^2 \mathscr{D}_w + v_p v_w \lambda_p p_{pw} \Gamma_{pw}}{\mathscr{D}_p \mathscr{D}_w - \Gamma_{pw} \Gamma_{wp} \lambda_p \lambda_w p_{pw} p_{wp}} + P_w \cdot \frac{v_w^2 \mathscr{D}_p + v_p v_w \lambda_w p_{wp} \Gamma_{wp}}{\mathscr{D}_p \mathscr{D}_w - \Gamma_{pw} \Gamma_{wp} \lambda_p \lambda_w p_{pw} p_{wp}} \right]. \tag{6.10}$$

Since the cell has one slow wrapped mode which showed the run-time bias ($\eta_w > 0$) (Fig. 6.3) and one fast push mode which is blind to the chemoattractant ($\eta_p \approx 0$), we investigated the *mixed chemotaxis strategy*. Figure 6.5 shows the response function μ_w dependency on the probability p_{wp} that a wrapped run is followed by a push run ($p_{pw} = 1 - p_{wp}$). The graph has two limits; $p_{wp} = 0$ means that the cell performs the wrapped mode interrupted by turns, and $p_{wp} = 1$ denotes the bacterium runs in the push mode interrupted by stop events. The dependence of μ_w on p_{wp} demonstrates two interesting points. Firstly the mixed chemotaxis strategy (the combination of wrapped and push runs) may lead to an optimized chemotactic

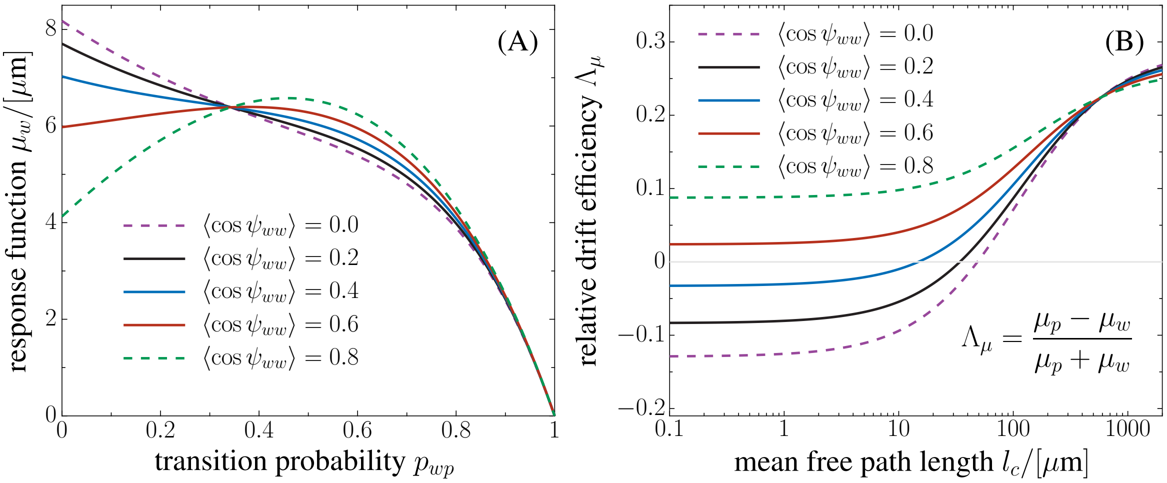

Fig. 6.5 (A) Response function μ_w as a function of the transition probability p_{wp} from the wrapped to the push mode (we set $p_{pw} = 1 - p_{wp}$). For $p_{wp} = 0$ bacteria stay in the wrapped mode and perform run-and-turn motility. In the opposite limit ($p_{wp} = 1$), they perform push runs that are occasionally interrupted by stops. The dependence of μ_w on p_{wp} is not monotonic and all curves intersect around $p_{wp} \approx 0.35$ reflecting a robust chemotactic response independent of the turn statistics $\langle\cos\psi_{ww}\rangle$. Parameters: average turn angles $\langle\cos\psi_{pp}\rangle = 0.9$, $\langle\cos\psi_{pw}\rangle = -0.9$, and $\langle\cos\psi_{wp}\rangle = -0.9$, speeds $v_p = 25\,\mu\mathrm{m/s}$ and $v_w = 13\,\mu\mathrm{m/s}$, average reorientation rates $\lambda_p = 0.3\,\mathrm{s}^{-1}$ and $\lambda_w = 0.4\,\mathrm{s}^{-1}$, rotational diffusion $D_p = 0.03\,\mathrm{s}^{-1}$ and $D_w = 0.13\,\mathrm{s}^{-1}$, spatial dimension $d = 3$. (B) Chemotaxis in heterogeneous environments. The plot shows the relative difference Λ_μ of the response functions μ_p and μ_w as a function of the mean free path length in a disordered environment. If the obstacle density is low (large mean-free path length), the faster run mode is the beneficial one. However, as collisions become more frequent – i.e. if the mean-free path is comparable to the average run times – both run modes are equally efficient. In crowded environments, where l_c is smaller than the average run length, the wrapped mode may even become the more efficient one ($\Lambda_\mu < 0$). Parameters: mean turn angles for collision with obstacles $\langle\cos\psi_c\rangle = -0.3$, $p_{pw} = 0.6$, $p_{wp} = 0.4$; other parameters as in (A). Based on data, we estimated $0.2 \leq \langle\cos\psi_{ww}\rangle \leq 0.6$ for *P. putida*, represented by solid lines in both panels. Taken from [104].

drift. Secondly, there is an intermediate value of $p_{wp} \approx 0.35$ at the intersection for all of the mean cosine of the turn angle $\langle \cos \psi_{ww} \rangle$. This exhibits a novel way of ensuring the robustness of bacterial chemotaxis; in a certain range of p_{wp} values, the drift becomes independent of the reorientation angle.

Surprisingly, *P. putida* uses the wrapped mode to do chemotaxis as the push mode would be more efficient. To address this behavior, we investigated the effect of disordered environment on *P. putida* motility. *P. putida* is a soil bacterium, and its evolutionary swimming strategy can be a reflection of the interaction between bacterium and habitat. Structurally, soil is a heterogeneous environment. We approximated the heterogeneous environment as an array of obstacles of size σ at a density ρ_o. The cell can ballistically swims on average before colliding with an obstacle. The mean free path $l_c = 1/(\rho_0 \sigma)$ is the characteristic distance between obstacles. The collision rates depend on the speed of the respective run modes, $\kappa_{p,w}^{(c)} = v_{p,w}/l_c$. The collisions are included in the active particle model, assuming that when cell collides to the obstacle it reorients by a random angle ψ_c. In this context, the relevant transport coefficients μ and D are structurally similar to Eqs. (6.8,6.10) discussed before. The rotational diffusion coefficients are renormalized by collisions with obstacles:

$$D_p \to D_p + v_p \rho_0 \sigma (1 - \Gamma_c), \tag{6.11a}$$

$$D_w \to D_w + v_w \rho_0 \sigma (1 - \Gamma_c). \tag{6.11b}$$

The mean cosine of the reorientation angle upon collisions of cell is given by $\Gamma_c = \langle \cos \psi \rangle_c$. Since the relative increase of rotational diffusion is proportional to the speed, collision is more likely to happen for the faster run mode in a given time interval. For the crowded environment $l_c \to 0$, the expressions for the transport coefficients change:

$$\mu_w \approx \frac{P_w}{d} \cdot \frac{\langle \cos \psi_{wp} \rangle p_{wp} + \langle \cos \psi_{ww} \rangle (1 - p_{wp})}{1 - \langle \cos \psi_c \rangle} \cdot l_c + \mathcal{O}\left(l_c^2\right). \tag{6.12}$$

When $l_c \to 0$, the response function is independent of speed and finally disappears. In this regime, the geometric properties determine the chemotactic drift. Consequently, ability to escape from traps is more effective than swim quickly. Figure 6.5B displays above interpretations The plot displays the relative difference in the response functions $\Lambda_\mu = (\mu_p - \mu_w)/(\mu_p + \mu_w)$ as a function of the mean free path. For the large amount of l_c (the lower amount of obstacle density), μ_p is more prominent. This situation is similar to swimming in the bulk. If l_c is smaller than the average run length, the wrapped mode may become more effective than push mode ($\Lambda_\mu < 0$).

6.5 Summary and discussion

In this chapter, we discussed the chemotaxis response of the *E. coli* in a linear gradient initially. The classical definition of the bacterial chemotaxis originated from the *E. coli* studies; the cell biases the motion in a way that to reach/avoid the source of the attractant/repellent [2]. Our experimental results also shows the same manner. Also exploring the diffusion coefficient D_T during tumble displayed an improvement in an unfavorable direction. To find the bacterial dynamic properties, extracting the run and tumble states from the trajectories is the standard approach. There are some heuristic methods based on the speed and angular velocity dynamics of the bacterial cell [14, 75, 102]. Those procedures categorize the run and tumble phases relying on fulfilling some parameters with roughly $\sim 10\%$ of detection error. We propsed the robust methodology which used to describe the swimming motion of *E. coli* in two dimensions stochastically. Two sets of overdamped Langevin equation for speed and angular dynamics were considered. The moments, distribution and autocorrelation functions of the equations provided us a detailed stochastic description of the run-and-tumble motion. Besides, a set of inferred swimming parameters were obtained. The experimental results of a heuristic tumble recognizer were in good agreement with both theoretical predictions from our model and with numerically determined functions using the inferred swimming parameters. The approach of inferring parameters is a robust method to classy run-and-tumble states without acquiring sets of threshold parameters, which are normally the foundation of heuristic tumble recognizer methods. However, additional developments will be needed for other bacteria species with different swimming strategies. In order to apply the inference method to other bacteria, for instance, *P. putida*, the Langevin equations 6.2 and 6.3 require some modifications. Furthermore, the alternating swimming speeds of *P. putida* should be considered to have an elaborate model of the speed dynamics.

Next part of the chapter was about chemotaxis study of *P. putida*. For the first time, we performed a detailed analysis of the chemotaxis strategy of a bacterial swimmer with a multi-mode swimming tactic. The soil bacterium *P. putida* exhibits run phases with pushing, pulling and wrapped filament configurations. While the pull mode can be largely neglected, the two remaining dominant run modes showed distinctly different chemotactic responses: for runs in the wrapped mode with CW rotation of the flagellar motors, a clear run-time bias was observed, whereas runs in the push mode, with CCW motor rotation, were not affected in the presence of chemoattractant gradient. We developed an active particle model of multi-mode motility to analyze the influence of this asymmetry on the chemotactic motion of the swimmers in the long-time limit. Based on our model, we could show that the presence of a non-responsive run mode may still be beneficial to ensure an efficient and robust chemotactic performance of the swimmers. Moreover, our model suggests that the lower swimming speed during the chemo-responsive wrapped mode as compared to the non-responsive push mode enhances the chemotactic efficiency in dense, crowded environments.

Chapter 7

Cell motion in dense populations

7.1 Introduction

Despite the focus on single cell motility researches in an aqueom environment, bacteria predominately live within biofilms in natural environment [129]. Biofilm is a 3D complex structure combination of bacterial cells and extracellular matrix, which forms as a developmental process [130]. Initially, the process starts with attachment of the free swimmers to the surface through cell-surface-associated adhesins. In the early biofilm formation stage, sessile cells begin to divide and generate extracellular polymeric substance (EPS). Subsequently, 3D structures develop and maturate over time. In this phase, the EPS scaffold provides a medium with heterogeneous chemical and physical microenvironments for organisms in where they have social interaction. Finally, cells leave the biofilm to re-enter the planktonic phase and float in the aqueom environment as single swimmers [130]. The sessile cells within the biofilm are able to alter their physiology and evade the destructive factors [131]. The bacterial community within the biofilm is a combination of motile and sessile populations [132]. Motile sub-populations are important for community survival. They are assumed to have roles in lots of processes, for instance, driving biofilm colony expansion, searching for food [133]. However, the physiological functions of motile sub-populations in biofilm communities are largely obscure.

Biofilm development is a result of the social group mechanism of cell communities, quorum-sensing system [91]. As we described in section 2.5, every cell individually synthesizes the autoinducers, which are either passively released or actively secreted outside of the cells. By increasing the cell density, the concentration of the autoinducers enhances in the surrounding. When the accumulation of the autoinducers reaches a threshold for detection, all the population exhibits changes in gene expression. Therefore, the quorum-sensing system enables cell populations to behave in a uniform and collective manner [91]. Our model organism, *P. putida*, is a rhizosphere-colonizing bacterium. They survive on plant roots and the soil area. Espinosa-Urgel et al. [134] studied the quorum-sensing system of *P. putida* for the first time. They characterized the expression pattern of a gene, which is involved in initial bacterial colonization of plant surfaces. The expression of a particular gene might be involved in quorum-sensing process, *ddcA*, was maximal at the beginning of stationary phase, when the density of the cells is the highest in the batch culture. The gene expression was independent of nutrient depletion, phosphate starvation, and the medium pH changes during bacterial growth in the medium. The study indicated that *P. putida* responded to population density. However, the mechanism is still unspecified. Moreover, this potential quorum-sensing system plays a role in the communication of *P. putida* with plants, a mutant strain lacking *ddcA* gene reduced their ability to colonize on the plant surface. This investigation raised a question regarding the effect of the quorum-sensing system on cell motility.

Besides the collective gene expression of the bacteria in biofilm as a result of quorum-sensing system, the cells within the biofilm display a collective motion, characterized by periodic streams [135]. One of the first evidence of the collective motion of bacteria was introduced in a paper by Adler in 1966 [136]. The *E. coli* cell suspension settled at one end of a capillary tube with a uniform concentration of the food source. Over time, the patch of bacteria traveled together to reach an area with a higher amount of nutrition concentration. The reason behind the traveling bacterial band was that the bacteria in the dense region consumed the nutrition sources. The nutrition consumption of the bacteria within the band created a chemical gradient along the tube. The study in Ref. [124] tracked the individual *E. coli* cells inside the wave while measuring the global properties of the wave. The local gradient was sensed by the single swimmers, and all the population synchronized their motion to travel as a band. The population exhibited classical chemotaxis behavior and increased their run length on average to progress in a favorable direction. Although the single-cell bacterial chemotaxis is well understood [65], there is still lack of knowledge about cell interactions effect on chemotaxis. A recent study of the effect of high cell density on chemotactic behavior of *E. coli* showed that at a higher density, the chemotactic drift strongly suppressed [137].

We investigated collective motion in two possible ways. At first, we will introduce an experimental approach to investigate the effect of cell-density on single-cell motility by implementing the method utilized in Ref. [134]. Indeed, we studied the impact of the social group mechanism on cell motility, exposing the bacteria to a medium with different concentrations of the autoinducers. To better understand the experimental set-up, we explain the growth curve model of bacteria in liquid medium. The bacterial cell density, in bulk liquid medium over time, is changed and described by the growth curve. The growth curves are obtained by measuring OD_{600} (optical density at 600 nm). The curve has the generic four-phase pattern of a standard bacterial population growth (Fig. 7.1). The first phase is the "lag" phase, when the cells have vigorous metabolic activity without division to adjust to the new environment. Afterward, the population enters the "log" (logarithmic) phase when rapid cell division occurs. The cells in the middle of the log phase are normally investigated for cell motility assays. In this phase, growth rate and death rate are equal, which might be a result of the depletion of required nutrients and/or the production of an inhibitory product. Eventually, the dying cells overcome the live cells in the "death" phase [138]. Indeed, the concentration of autoinducers should raise over time when the cells are in the log phase. When the cells reach the stationary phase, the density of the autoinducers may not change anymore. In our particular experiment, the media were generated from a cell suspension, which was grown for a couple of hours. When the cell density met different OD_{600}, the media were cleaned of cells without losing the containing chemical molecules, which were secreted into the medium by bacteria. By exposing the fresh cells to the conditioned-media, the motility of the cells was examined.

Finally, we will introduce the various aspect of collective motion in *E. coli* and *P. putida* while they formed a traveling band. In fact, we considered the influence of distinct cell swimming strategies, i.e. run-and-tumble in *E. coli* and run-reverse-screw in *P. putida*, on bacterial collective motion.

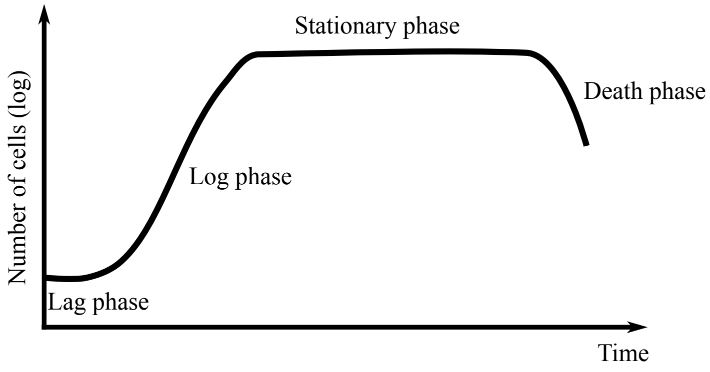

Fig. 7.1 Different phases of a bacterial growth curve in culture medium.

7.2 Material and methods

Quorum-sensing set-up

Conditioned medium preparation and bacteria cultivation

A single colony of *P. putida* KT2440 from a LB agar plate was inoculated in an overnight shaking culture (at 30 °C on a rotary shaker at 300 rpm) of 100 ml LB Broth ($10\,\mathrm{g\,l^{-1}}$ Difco Bacto$^{\mathrm{TM}}$-Tryptone, $5\,\mathrm{g\,l^{-1}}$ Difco$^{\mathrm{TM}}$ Yeast Extract and $10\,\mathrm{g\,l^{-1}}$ NaCl). The overnight cell culture was diluted into a fresh LB broth at a ratio of 1:100 with a final volume of 400 ml. Each conditioned medium (C-medium) was prepared in two steps:

- 100 ml of cell suspension was taken at a specific time after inoculation. Table. 7.1 shows the time table and the corresponding cell density, OD_{600}. For instance, the S2 medium was taken when OD_{600} was 0.56, 2 h after inoculation.
- The medium was cleaned of the cells by centrifugation for 10 min at 4400 rpm at room temperature, followed by filter-sterilizing and stored at 4 °C.

Table 7.1 Conditioned medium properties

	C2	C3	C4	C5	C6
OD_{600}	0.56	1.25	1.6	1.84	$+++^{*}$
Time(h:min)	2:00	2:20	2:30	3:15	Overnight

* For the overnight culture, the photometer could not detect the exact amount of the cell density, since it is out of the detection range.

For the cell motility analysis, 50 ml of new cell suspension was prepared and grown to their mid-exponential phase with $OD_{600} = 0.62$. The cell suspension was washed free of growth medium once by centrifugation (2400 rpm, 10 min, room temperature), followed by gentle resuspension of the pellet in 30 ml MB+. Afterward, The suspension was allocated into 6 tubes. Firstly all the tubes were centrifuged at 2400 rpm, 10 min, and then resuspended each with the corresponding C-medium, C1 (fresh LB medium), C2, C3, C4, C5, and C6. The final $\mathrm{OD}^{*}{}_{600}$ of the 6 tubes after washing was ~ 0.2; because some cells were washed out by centrifugation and resuspension during the sample preparation, $\mathrm{OD}^{*}{}_{600}$ is the exact cell density after the sample preparation. The cells were incubated for an hour to adapt to the new environmental circumstances. The samples were injected by a 10 ml syringe with a Luer tip into an ibiTreat μ-Slide VI$^{0.1}$ (Ibidi, Martinsried, Germany) (Fig. 7.2). The chambers were sealed with Luer Plugs Male (Ibidi, Martinsried, Germany) to prevent any flow within

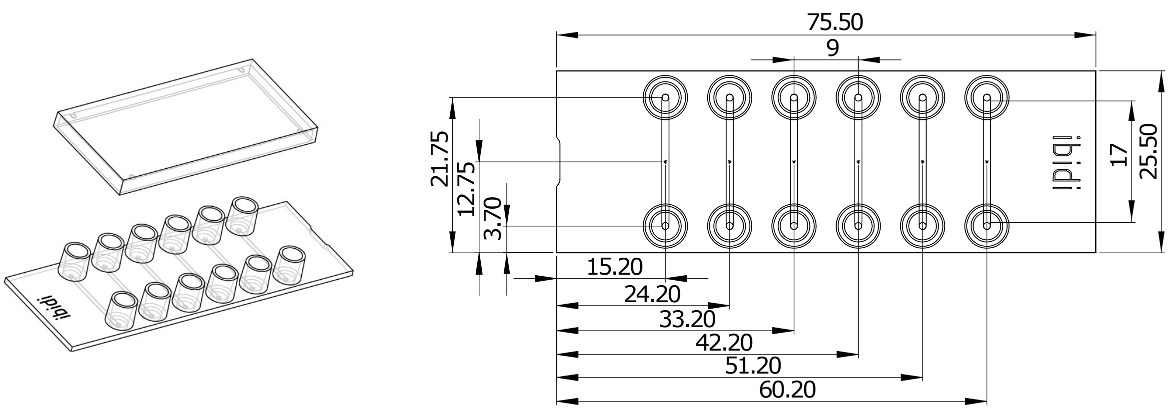

Fig. 7.2 Scheme of linear chambers μ-Slide VI$^{0.1}$. The chamber consists of 6 linear channels, each with two reservoirs. The dimensions are in millimeters. Figure was adapted from Ref. [139].

the channels. The cells were imaged at a frame rate of 20 fps and analyzed with the same procedures described in section 3.4.

Bacerial band formation

Microfabrication

The linear chambers were fabricated by standard "soft lithography" technique [140]. The mold was earlier constructed by Matthias Theves (see technical details in materials and methods section of [141]). Briefly, the channel layout was sketched using Novarm DipTrace, a CAD freeware. To generate the negative imprint (mold), contact photolithography with SU-8 2000 series photoresists (Microresist (Berlin, Germany)) was used. After a series of treatments, the master mold was ready to use for chamber preparation. Two master molds were used in this set-up. The chamber molds were rectangular shape with a length of $\sim$ 3 cm, and a widths of 1 mm. The depth of chambers were 50 and 100 µm.

The microchannels themselves were built by forming liquid PDMS together with 10% of curing agent (Sylgard 184, Dow Corning Corp., Midland, USA) against the master mold. The liquid PDMS and curing agent were mixed well together and poured on top of the master mold. All together they were located into a vacuum desiccator to remove air bubbles. Then, the PDMS was treated through heating up to 75 °C for 60 min. One hour before each experiment, the channel was cut out using a scalpel and peeled off its mold. The PDMS block was located in a plasma cleaner (Harrick Plasma PDC-002, Ithaca, USA) together with a glass coverslip. This plasma cleaning treatment developed a strong adhesion between the surfaces of the coverslip and the PDMS. Afterward, the PDMS was placed on the top of the coverslip. After chamber fabrication, one droplet of cell suspension was placed on one end and absorbed by capillarity. The channels were then sealed with a curing epoxy resin (Araldite 90s, Bostik). In order to avoid sticking the cells to the resin, the sealed chambers stayed on the bench for at least 30 min to dry out completely.

Band formation

To push all the cells to one extremity of the channel, they were centrifuged along their main axis at 65 g, for 30 min. After centrifuging, most of the bacteria were located at one end of the channels and formed the band. The chambers were imaged every 3 min over a 1 h period using 4X UPLFLNH objective (Olympus, Japan) and IX71 Inverted Microscope (Olympus, Japan).

Cell growth

E. coli AW405 strain was cultured overnight in liquid LB broth (Lennox, Sigma Aldrich) at 37° from a single colony and being shaken at (200 rpm and 37 °C. The overnight culture was diluted into the ratio of 1:100 in fresh LB broth and grown to the mid-exponential state ($OD_{600} = 0.8$). The cell suspension was filled into the chamber directly.

A single colony of *P. putida* KT2440 strain was cultured overnight in 100 ml TB ($10\,\mathrm{g\,l^{-1}}$ tryptone (Applichem), $5\,\mathrm{g\,l^{-1}}$ NaCl) in a shaking culture at 30 °C. The highly motile overnight cell suspension was directly used to produce a band in the linear chamber. The cell density was increased up to $\mathrm{OD}_{600} = 0.9$ by centrifugation to have the same initial condition for both strains.

7.3 *P. putida* dynamics in dense populations

The accumulation of autoinducers in the external medium is a function of the cell population; more cell division leads to an increase in the net concentration of autoinducers in the medium. Although the concentration of autoinducers was not measured directly in our experiment, the cell density evaluation (OD_{600}) was an indirect way to estimate the concentration of the autoinducers. An equal quantity of bacterial cells was exposed to those C-media. The bacteria in the C-media were growth for an hour, and the bacterial motility in each group was investigated. The fixed bacterial density in each sample was the advantage of the set-up by which the physical interaction, e.g. collision, was identical for all samples. Instead, the chemical profiles, i.e. autoinducers concentration, represented the cell density.

Table 7.2 Influence of C-media on the cell division

	S1	S2	S3	S4	S5	S6
$\mathrm{OD}^h{}_{600}/\mathrm{OD}^*{}_{600}$	2.3	1.74	1.83	1.13	1.25	0.9

Initially, we investigated the cell responses to the C-media in terms of cell division. *P. putida* has a doubling time of $\sim 42\,\mathrm{min}$ in LB medium [142]. The OD_{600} measurement one hour after exposing the cells to the C-media could be a measure to identify the bacterial response to the contents of the medium; in best condition, the cells might be doubled in one hour (one hour is the duration of cell incubation in C-media). The ratio of that cell density after one hour of incubation ($\mathrm{OD}^{h}{}_{600}$) to the initial cell density ($\mathrm{OD}^{*}{}_{600} \sim 0.2$, which was mentioned in section 7.2) was shown in Table 7.2. The ratio decreased from S1 to S6. The S1 was the control experiment in which the cells were inoculated into the fresh LB medium. S1 population divided once within one hour of incubation; the S1 cell had a $\mathrm{OD}^{h}{}_{600}/\mathrm{OD}^{*}{}_{600} = 2.3/1$, which means that the initial cell density was doubled. The S2 and S3 populations were inoculated to the C-media C2 and C3 which belong to the mid-exponential growth curve of *P. putida* and they showed the similar ratio. The stationary phase of *P. putida* growth curve were started at time 2:30 h:min (Table. 7.1) in when the C4 medium was prepared. That phase continued until the C5 was developed. The corresponding bacterial samples, S4 and S5, displayed the similar density ratio as well. The S6 sample was exposed to the overnight medium, C6, and its ratio of the cell density was about one.

Afterward, the transition scenarios among run states in each population (S1-S6) were considered. Because of difficulty with flagella visualization in this experiment set-up, the bundle information was not identified for each run. However, a comparison of the turn angle probability distribution to the same distribution with identified bundle configuration in Fig. 4.6 might clarify the run state contributions in their dynamics. The plots in Fig. 7.3 are absolute values of turning angle probability distribution for each sample. To classify events, the turn angles greater (less) than 90° were set as reversals (stops). Accordingly, the blue and orange bins are associated with reversal and stop, respectively. As we clarified in Fig. 4.6, the stop events are any interruption in either wrapped or push runs, and the reversals are the outcome of transitions from push to wrapped (and vice versa from wrapped to push). Even though the S1 population shows a major portion of stops, the reversal subgroup in this distribution may indicate the presence of some push-wrapped transition while the cells swam (Fig. 7.3A). The rest of the turn angle probabilities displays two clear subgroups, reversals and stops (Fig. 7.3B-F). Then we examined two transition parameters, $\kappa_{r,s}$ and $\kappa_{r,re}$, which reflect the transition rates from the run to stop and reversal, respectively. Indeed, κ_{ij} captures the average number of events (stops and reversals) in time interval $[t, t+\Delta t]$. The $\kappa_{r,s}$ and $\kappa_{r,re}$ of all populations were shown in Fig. 7.3G. The $\kappa_{r,re}$ curve shows significant changes from the S1 population to the rest. Furthermore, it has a clear plateau (from S2 to S6 populations) which underlines the fact that the reversal rate transition, $\kappa_{r,re}$, was not affected by the different C-media. Both curves displayed maximum transition rates in the

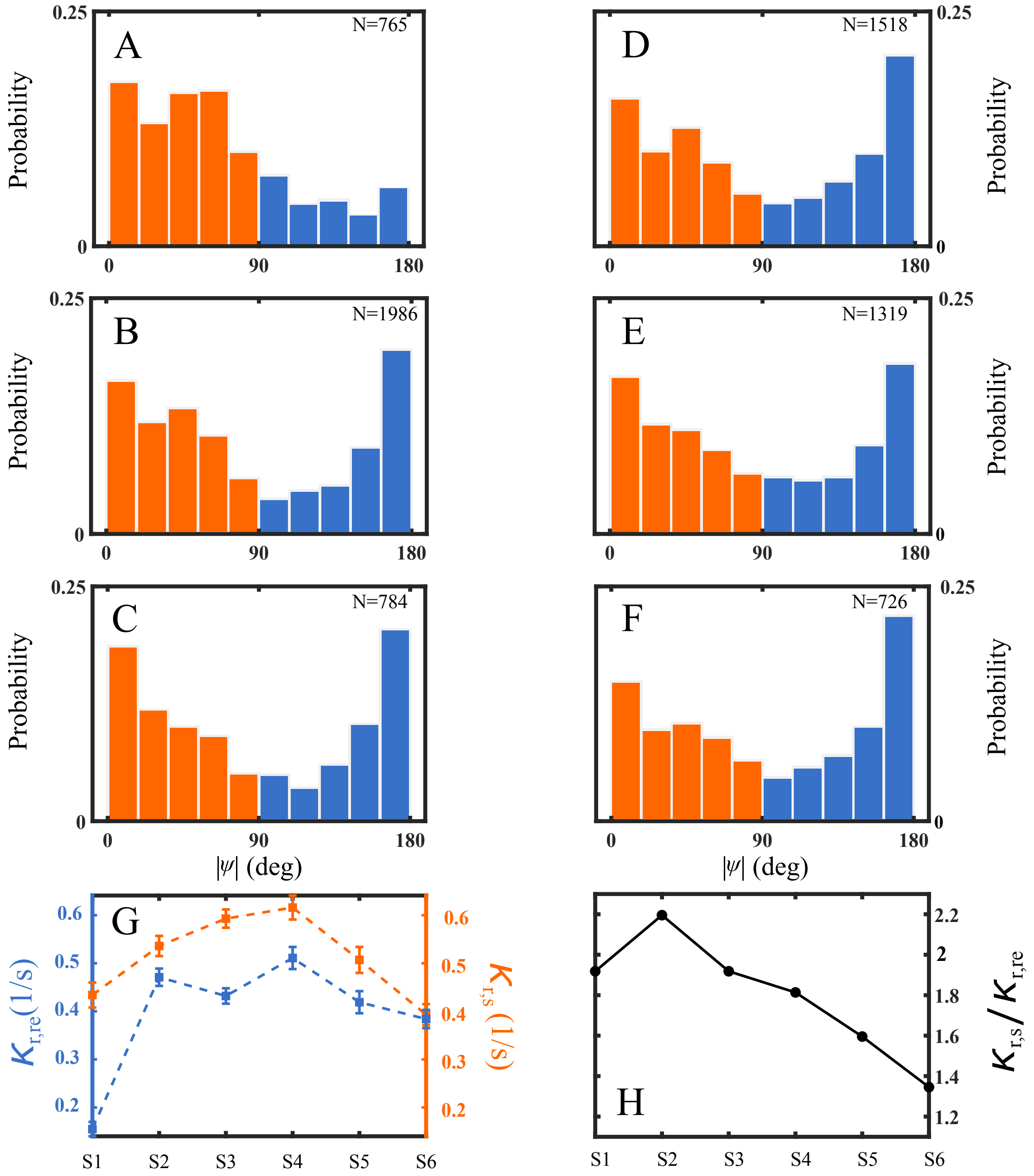

Fig. 7.3 (A-F) Turn angle distributions for S1, S2, S3, S4, S5, and S6 cell populations treated with conditioned medium. The angles greater than 90° were assigned to reversal events and marked in blue. Those less than 90° were selected as stop events and marked in orange. (G) Transition rates $\kappa_{r,s}$ and $\kappa_{r,re}$. (H) Transition rates ratio $\kappa_{r,s}/\kappa_{r,re}$.

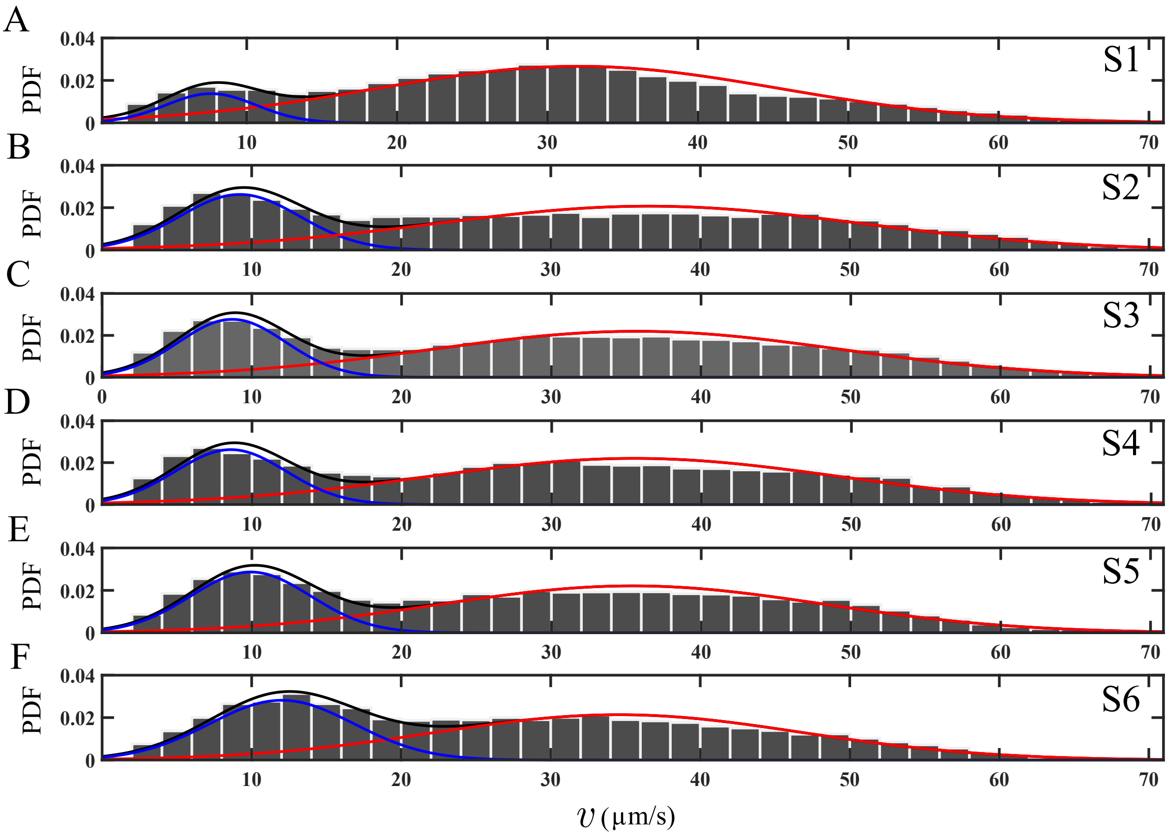

Fig. 7.4 Run speed distribution in different cell populations. The curves are deduced from the Gaussian mixture model (GMM). The blue and red subgroups are two components of the model and demonstrate wrapped and push modes, respectively. Each histogram includes information from at least 15000 data points.

S4 population. Also, the ratio of $\kappa_{r,s}/\kappa_{r,re}$ monotonically decreases over populations S2-S6, which indicated that the average number of events (stops and reversals) were becoming equal over those populations. In other words, more autoinducers in the media may drive the cells to have equal stops and reversal events on average.

One of the unique properties to distinguish push and wrapped modes was their run speeds; The run speed of wrapped mode is half of the push mode on average. In order to categorize the slow and fast swimming modes, a Gaussian mixture model (GMM) was applied to the distributions of the instantaneous velocity, v, of runs as shown in Fig. 7.4. The GMM is a probabilistic model for estimation of the probability density function. The GMM classifier are well known for their ability to model complex distributions with multiple subgroups [143], for more details see Appendix B. In fact, a mixture of Gaussians produces the distribution of subgroup characteristics in this method. All the distributions in Fig. 7.4 have two distinct peaks, one from each flagellar mode. The blue and red Gaussian fits represent the instantaneous velocities of the wrapped and push modes during run, respectively. The distribution series have one important feature; the wrapped mode peaks (blue lines) shifted to the higher velocities from fresh medium (C1) to overnight C-medium (C6). The S2-S4 populations do not show changes in the wrapped and push distributions. However, their probability of wrapped mode velocity became larger than in the S1 population, which indicated that the number of runs with the wrapped bundle might have grown. The push mode peaks (red line) slightly shifted to higher values for the S1 to S2 populations and became similar for the rest of them. Before we knew about run mode properties through the flagella bundle visualization, Theves et al., in Ref. [14] reported that upon the reversal the *P. putida* swimming speeds change by a factor of two. They examined the difference in swimming speed before v_k and after a reversal v_{k+1} divided by the sum of both speeds, $Q = v_{k+1} - v_k / v_{k+1} + v_k$. We evaluated this approach of the available data-set in Fig. 7.5. For runs with stops, $\phi < 90°$, the Q-distributions peaks are close to zero, which indicated that systematic difference between the swimming speeds before and after the turning event was not observe (Fig. 7.5A-F, left panels). However, the runs with reversal, $\phi > 90°$, had Q-distributions displaying two maxima centered around $Q = \pm 1/2$ except the S1 population (Fig. 7.5A-F, right panel). Figure 7.5 demonstrated that the angle criterion to separate reversals from stops worked well. Also, figure 7.4 and 7.5 leads us to conclude that the wrapped mode proportion in *P. putida* swimming tactic was larger in populations S2-S6 than in S1.

7.4 Collective motion, *P. putida* vs *E. coli*

In the present work, we prepared a high density region of bacteria using a microfluidics-based approach. Two microfluidic chambers were filled with *P. putida* and *E. coli* strains, respectively, and they were accumulated at one end of the micro-channel by centrifugation. The initial condition for both strains was roughly the same; *ca.* 90% of the cells were concentrated at the end of the micro-channels.

The wave traveling in *E. coli* studied was before by Saragosti et al. [124]. They reported that *E. coli* wave propagated at constant speed, $V_{\text{wave}} = 3.8 \pm \mu\text{m/s}$, along the main axis of micro-channel. The concentration profile of the wave did not changed over time of the experiment. They investigated individual trajectories within the propagating wave. The bacterial trajectories analysis indicated that the mean run length was longer in the direction of propagation. Furthermore, the directional persistence was larger compared to the opposite direction. We also examined the wave travelling of *E. coli* with our microscopy set-up. Because of the microscopy constraints, we were able to monitor $\sim 0.2\,\text{cm}$ of the micro-channel length. We fixed the field of view and monitored the wave in that region. Our

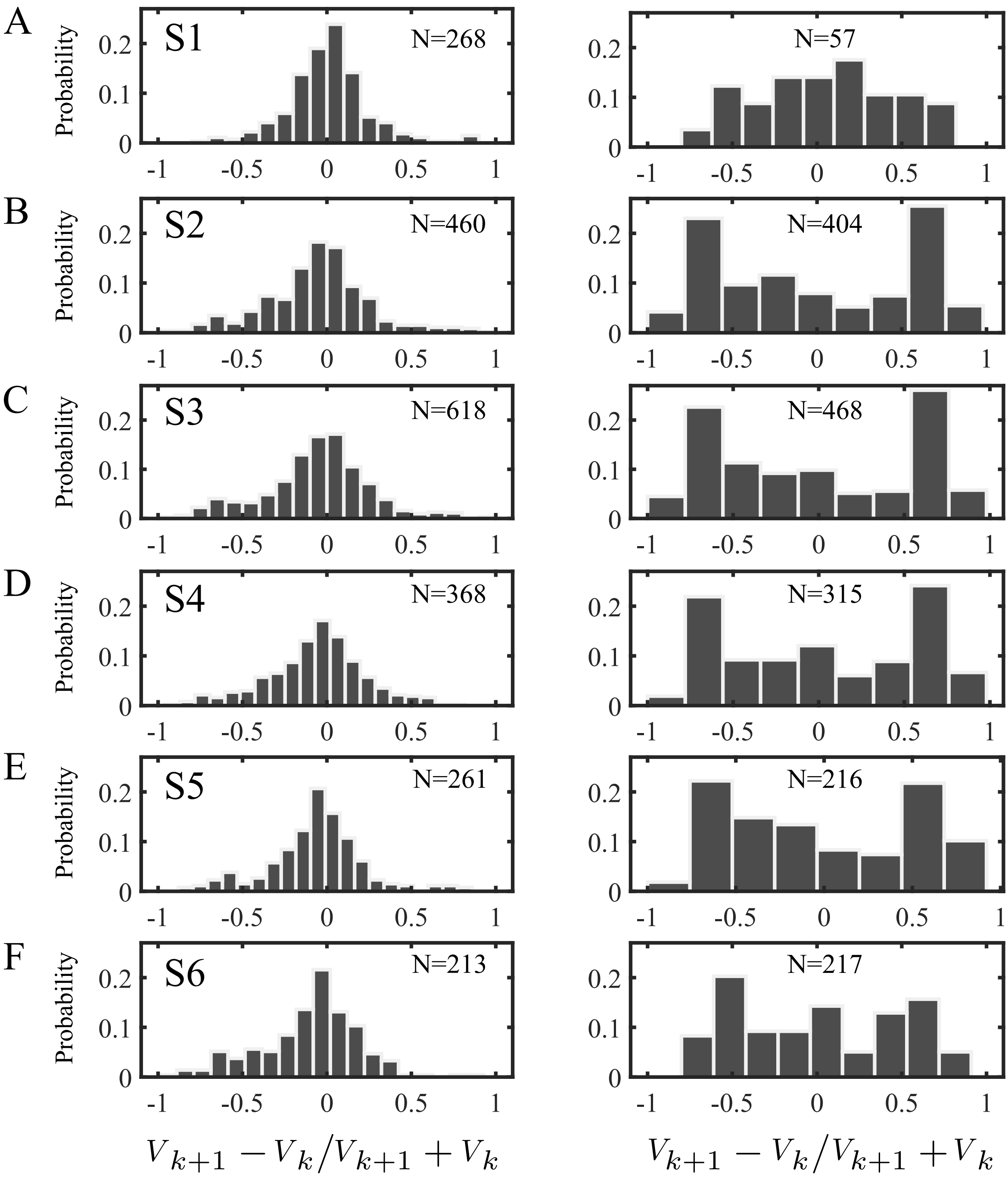

Fig. 7.5 Average speeds of two subsequent runs v_k and v_{k+1} from the cell populations S1-S6. The difference in average speed was calculated between each pair of runs and normalized by the sum of their average speed. The left panels belong to two subsequent runs interrupted by stops ($\phi < 90°$). The right panels refer to two subsequent runs interrupted by stops ($\phi > 90°$).

observation indicated that *E. coli* made the coherent band and traveled along the channel (Fig. 7.6A). The white pixel of the figure 7.6A are the bacterial cells. The yellow lines shows the approximate border of the bacterial bands (it was determined manually by an intensity threshold via ImageJ). Five concentration profiles measured at different times were superimposed in Fig. 7.6B. The concentration profiles at times 15 min and 30 min show the complete band length. The rest of the concentration profiles contain part of the band. This observation indicated that most of the *E. coli* cells synchronized their run-and-tumble motion and traveled together as a collective wave.

On the other side, we examined the same protocol for *P. putida*. The high density bacterial profile accumulated on one end of the chamber and the bacterial band dynamics were investigated over time. Fig. 7.7A displays the images of *P. putida* collective behavior in the chamber. The superimposed concentration profiles of four time intervals were depicted in Fig. 7.7B. The image frame in 0 min displays the initial location of the *P. putida* band (marked in yellow). The corresponding concentration profile shows a peak in position 150μm of the channel, and some of the single swimmers occupied the rest of the chamber. The next images display the relocation of the wave (with certain bacteria density). One apparent feature is some bacteria escaped from the high-density region as single swimmers and spread behind and front of the band. The high dense peaks for all the time series indicated that the number of the bacteria in the wave is stable over time. Simultaneously the density of the single swimmers outside of the wave increased. Although the cells could divide during imaging, increasing the cells in the background would be an effect of micro-colonies establishment on the channel surfaces (attaching the *P. putida* cells to the channel surfaces is their natural behavior we faced in everyday experiments). That was a significant difference between the collective motions in *E. coli* and *P. putida*. Although most of the cell population in *E. coli* experiment participated in a collective manner and constructed a wave, in *P. putida* case, just part of the cell population travelled along the chamber as a coherent wave.

7.5 Summary and discussion

The bacterial cells construct a complicated 3D structure, a biofilm, in their natural habitat. The high bacterial density in this structure leads to inevitable interactions among cells. These interactions can be physical or chemical. One kind of chemical interaction among the population is quorum-sensing, by which the cells communicate and exchange the information through autoinducers. We established a set-up to investigate the autoinducers' impact on *P. putida* motility. The bacterial cells were grown in a rich medium over certain amount of time. While the bacteria divided over time, the production of the autoinducers increased. The C-media were papered at different times of cell growth and cleaned of

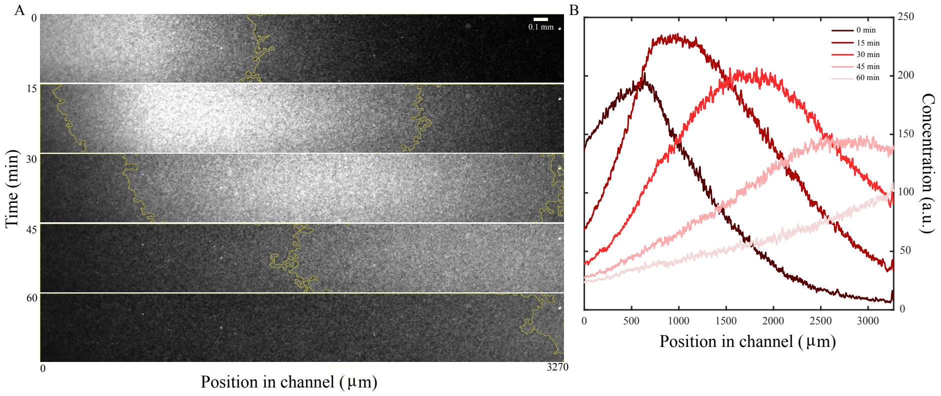

Fig. 7.6 Collective migration of *E. coli* in a PDMS channel. (A) The channel was filled with a homogeneous cell suspension followed by centrifugation to accumulate bacteria on the left end. The yellow lines displays the wave edge. The white pixels are the cells. (B) Five bacterial concentration profiles in the channel measured at different time intervals.

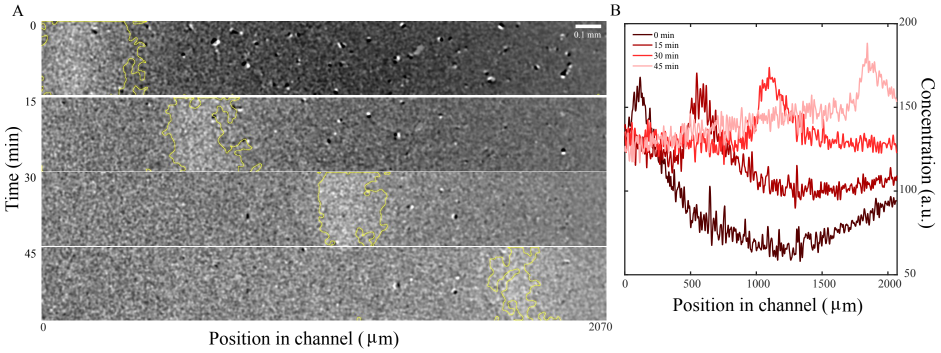

Fig. 7.7 Collective motion in *P. putida* in a PDMS channel. (A) The channel was filled with a uniform cell suspension followed by centrifugation to gather bacteria on the left end. The wave border is marked in yellow. (B) Four cell concentration profiles in the channel separated by 15 min time intervals.

cells. Therefore, each C-medium contained different autoinducer concentrations without the physical presence of the bacteria. After that, a fresh cell suspension was made and exposed to 6 different C-media. The initial cell density for all samples was same. After an hour of incubation, the cell motility under the C-media conditioned was investigated. The initial results indicated that the cell division was quite effected by C-media; The cells were grown with a higher amount of autoinducers divided less. One can argue that the cells' response to the C-media might be influenced by nutrition deficiency, which were consumed by the population while the C-media were prepared. With respect to the paper by La Rosa et al [144], we could conclude that cells within the first 12 hours of incubation had enough resources to consume. In this study, the uptake rates of amino acids and glucose in the different intervals of time of *P. putida* cell growth curve were measured through NMR analyses. The graph

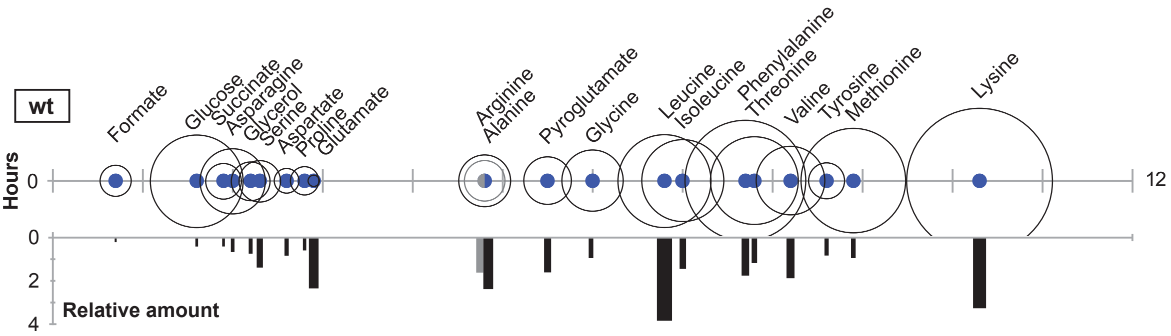

Fig. 7.8 Uptake parameters for the chemical nutrition absorbed by *P. putida*. Blue or grey dots indicate the time at which the concentration of the chemical component has decreased to 50% of the initial value, T_{50}. The circles show the time required to identify a decrease in the compound concentration from 75% to 25% of the initial value. The bar plot displays the relative amount of each compound in mM. Taken from [144].

in Fig. 7.8 represents the time points each chemoattractant was consumed in 12 hours, and also the speed of consumption of each. From hour 2 to hour 3, which was the time that the C2-C5 were papered, there were enough chemoattractants to consume. Besides, the circles displaying the speed of consumption are mostly overlapped, which indicates that at different time points in this period, the cells roughly consumed the same chemical resources. However, the C6 medium might have a deficiency in chemoattractants resources. The events dynamics revealed that except for the S1 population, the rest of the samples had two types of events (stop and reversal). However, the ratio of $\kappa_{r,s}/\kappa_{r,re}$ (transition rate from run to stop/reversal) decreased monotonically. The run speed probability distributions revealed that the wrapped mode subgroup grew from S1 to S2-S6 populations. However, the push mode subgroup did not display any deviation. The S1 samples contained lower amount of autoinducers. The bacterial cells in this medium reoriented with stop events. Corresponding run speed probability distribution suggests that most of the runs were in push mode. The run speed probability distributions for the S1-S6 samples also indicates that the wrapped mode subgroups became predominant, and the peak of the probabilities shifted to the higher values. In other words, media with higher amounts of autoinducers may affect the swimming tactic and led to an increasing abundance of runs with wrapped configuration.

The other approach we considered to study the collective motion was the traveling of high density bacterial bands in micro-channels. The bacterial bands for *P. putida* and *E. coli* were constructed by centrifugation of the channels filled with bacteria. Although the *E. coli* cells displayed the high density band and traveled together along the micro-channel as reported before [124], most the *P. putida* cells escaped from the high-density region of bacteria and spread along the channel. The bacteria concentration evaluation displayed that in the case of

P. putida only a few cells made a band and traveled along the micro-channel simultaneously. Resent study by Seyrich et al., in Ref. [145] presented an extensive study of the traveling waves of *E. coli* theoretically. This numerical study and theoretical modeling illustrated the effect of different parameters on the wave stability. In their model, the tumble rate λ is proportional to the chemotactic strength parameter. They showed that, for the small amount of the chemotactic strength, the pulse contains fewer bacteria, and some of the bacterial are left behind. The experimental assay of the *P. putida* wave illustrated a similar behavior. This may originate from the fact that the chemotactic response of *P. putida* relies on one swimming mode. The other fact is the concentration profiles

Appendix A

Kaplan–Meier estimator

As we discussed, the bacteria tracks contain episodes of runs and events. In fact, run sate is the time that bacteria swim between two events. In bacterial motility analysis, we always have an issue with leaving the bacteria out of the field of view. Consequently, the majority of the tracked data indicated that the runs are not complete (normally $\sim 20\%$ of runs were between two events). The survival analysis deduces the true survival time of random variable of our interest, run duration, using the incomplete observed time. The Kaplan–Meier estimator is a non-parametric statistic used to estimate the survival function, $S(t)$, from incomplete observed time by [146]

$$\hat{S}(t) = \prod_{j:T_j \leq t} \left(1 - \frac{\Delta N(T_j)}{Y(T_j)}\right),$$

where T_i is variable observed at time (T_j), and $Y(T_j)$ is the individuals known to have survived. One way to estimate the Kaplan-Meier variance $Var(\hat{S}(t))$ is the bootstrap method [126]. Specifically, bootstraping implies iteratively resampling a dataset with replacement. After forming B samples by sampling with replacement from the data, the Kaplan-Meier estimate $\hat{S}_b^*(t)$ is computed for each time t and each $B = 1, \ldots, b$. The variance estimate is

$$\widehat{Var}(\hat{S}(t)) = \frac{1}{B} \sum_{b=1}^{B} \left(\hat{S}_b^*(t) - \frac{1}{B} \sum_{c=1}^{B} \hat{S}_c^*(t) \right)^2$$

And we can estimate the standard errors given by

$$\widehat{SE}(\hat{S}(t)) = \sqrt{\widehat{Var}(\hat{S}(t))}.$$

Appendix B

Gaussian mixture model

A Gaussian mixture model (GMM) is a mixture of several Gaussian distributions [143]. For a n-dimensional component vector (or kernal) **t**, the mixture density function is described as:

$$p(\mathbf{t} \mid X) = \sum_{i=1}^{m} \alpha_i(X)\phi_i(\mathbf{t} \mid X),$$

where m is the number of components. GMM is parameterized by two sorts of values, one is mixing coefficients $\alpha_i(X)$ which can be a regarded as *prior* probability (conditioned on X) of the target vector **t**, with the constraints that $\sum_{i=1}^{m} \alpha_i(X) = 1$ so that the total probability distribution normalizes to 1, and also $0 \leqslant \alpha_i(X) \leqslant 1$. The other value is the unimodal Gaussian densities $\phi_i(t \mid X)$ which represents a conditional density of the target vector **t** for the *i*th kernal. Each Gaussian density is parameterized by the component means μ_m and variances σ_m using:

$$\phi_i(\mathbf{t} \mid X) = \frac{1}{\sigma_i^c(X)(2\pi)^{c/2}} e^{-\|\mathbf{t}-\mu_i(X)\|^2 \big/ 2\sigma_i^2(X)},$$

where c is the dimensionality of the **t**. The parameters of GMM are calculated applying the iterative expectation-maximization (EM) algorithm [147]. The algorithm starts from some initial random estimate of X, and then continues to update X until convergence is detected. Each iteration contains an E-step and a M-step. The E-step consists of calculating the expectation of the component assignments X for each data point given μ_i, σ_i, and ϕ_i. The M-step or the maximization step includes maximizing the expectations calculated in the E-step concerning the model parameters.

References

[1] Alexandre Persat, Carey D Nadell, Minyoung Kevin Kim, Francois Ingremeau, Albert Siryaporn, Knut Drescher, Ned S Wingreen, Bonnie L Bassler, Zemer Gitai, and Howard A Stone. The mechanical world of bacteria. *Cell*, 161(5):988–997, 2015.

[2] Howard C Berg. *E. coli in Motion*. Springer Science & Business Media, 2008.

[3] Raymond Nicholas Doetsch and Thomas Melbourne Cook. *Introduction to bacteria and their ecobiology*. Springer Science & Business Media, 2012.

[4] Ken F Jarrell and Mark J McBride. The surprisingly diverse ways that prokaryotes move. *Nature reviews microbiology*, 6(6):466, 2008.

[5] Howard C Berg. *Random walks in biology*. Princeton University Press, 1993.

[6] Judith P Armitage and Robert M Macnab. Unidirectional, intermittent rotation of the flagellum of rhodobacter sphaeroides. *Journal of Bacteriology*, 169(2):514–518, 1987.

[7] Li Xie, Tuba Altindal, Suddhashil Chattopadhyay, and Xiao-Lun Wu. Bacterial flagellum as a propeller and as a rudder for efficient chemotaxis. *Proceedings of the National Academy of Sciences*, 108(6):2246–2251, 2011.

[8] Kwangmin Son, Jeffrey S Guasto, and Roman Stocker. Bacteria can exploit a flagellar buckling instability to change direction. *Nature physics*, 9(8):494, 2013.

[9] Xiao Wu, Sébastien Monchy, Safiyh Taghavi, Wei Zhu, Juan Ramos, and Daniel van der Lelie. Comparative genomics and functional analysis of niche-specific adaptation in pseudomonas putida. *FEMS microbiology reviews*, 35(2):299–323, 2011.

[10] Pablo I Nikel, Esteban Martínez-García, and Víctor De Lorenzo. Biotechnological domestication of pseudomonads using synthetic biology. *Nature Reviews Microbiology*, 12(5):368, 2014.

[11] Inmaculada Sampedro, Rebecca E Parales, Tino Krell, and Jane E Hill. Pseudomonas chemotaxis. *FEMS microbiology reviews*, 39(1):17–46, 2014.

[12] Caroline S Harwood, Kathy Fosnaugh, and Marilyn Dispensa. Flagellation of pseudomonas putida and analysis of its motile behavior. *Journal of bacteriology*, 171(7):4063–4066, 1989.

[13] Kevin J Duffy and Roseanne M Ford. Turn angle and run time distributions characterize swimming behavior for pseudomonas putida. *Journal of bacteriology*, 179(4):1428–1430, 1997.

[14] Matthias Theves, Johannes Taktikos, Vasily Zaburdaev, Holger Stark, and Carsten Beta. A bacterial swimmer with two alternating speeds of propagation. *Biophys. J.*, 105(8):1915–1924, 2013.

[15] Marius Hintsche, Veronika Waljor, Robert Großmann, Marco J Kühn, Kai M Thormann, Fernando Peruani, and Carsten Beta. A polar bundle of flagella can drive bacterial swimming by pushing, pulling, or coiling around the cell body. *Scientific reports*, 7(1):16771, 2017.

[16] Marco J Kühn, Felix K Schmidt, Bruno Eckhardt, and Kai M Thormann. Bacteria exploit a polymorphic instability of the flagellar filament to escape from traps. *Proceedings of the National Academy of Sciences*, 114(24):6340–6345, 2017.

[17] Yoshiaki Kinosita, Yoshitomo Kikuchi, Nagisa Mikami, Daisuke Nakane, and Takayuki Nishizaka. Unforeseen swimming and gliding mode of an insect gut symbiont, burkholderia sp. rpe64, with wrapping of the flagella around its cell body. *The ISME journal*, 12(3):838, 2018.

[18] Maira A Constantino, Mehdi Jabbarzadeh, Henry C Fu, Zeli Shen, James G Fox, Freddy Haesebrouck, Sara K Linden, and Rama Bansil. Bipolar lophotrichous helicobacter suis combine extended and wrapped flagella bundles to exhibit multiple modes of motility. *Scientific reports*, 8(1):14415, 2018.

[19] ML DePamphilis and Julius Adler. Attachment of flagellar basal bodies to the cell envelope: specific attachment to the outer, lipopolysaccharide membrane and the cytoplasmic membrane. *Journal of Bacteriology*, 105(1):396–407, 1971.

[20] Michio Homma, Yoshibumi Komeda, Tetsuo Iino, and Robert M Macnab. The flafix gene product of salmonella typhimurium is a flagellar basal body component with a signal peptide for export. *Journal of bacteriology*, 169(4):1493–1498, 1987.

[21] Gary J Schoenhals and Robert M Macnab. Physiological and biochemical analyses of flgh, a lipoprotein forming the outer membrane l ring of the flagellar basal body of salmonella typhimurium. *Journal of bacteriology*, 178(14):4200–4207, 1996.

[22] George H Wadhams and Judith P Armitage. Making sense of it all: bacterial chemotaxis. *Nature reviews Molecular cell biology*, 5(12):1024, 2004.

[23] Howard C Berg. The rotary motor of bacterial flagella. *Annual review of biochemistry*, 72(1):19–54, 2003.

[24] Seiji Kojima and David F Blair. Conformational change in the stator of the bacterial flagellar motor. *Biochemistry*, 40(43):13041–13050, 2001.

[25] Scott A Lloyd and David F Blair. Charged residues of the rotor protein flig essential for torque generation in the flagellar motor of escherichia coli. *Journal of molecular biology*, 266(4):733–744, 1997.

[26] Jiadong Zhou, Scott A Lloyd, and David F Blair. Electrostatic interactions between rotor and stator in the bacterial flagellar motor. *Proceedings of the National Academy of Sciences*, 95(11):6436–6441, 1998.

[27] Takanori Hirano, Shigeru Yamaguchi, Kenji Oosawa, and S-l Aizawa. Roles of flik and flhb in determination of flagellar hook length in salmonella typhimurium. *Journal of bacteriology*, 176(17):5439–5449, 1994.

[28] Mostyn T Brown, Bradley C Steel, Claudio Silvestrin, David A Wilkinson, Nicolas J Delalez, Craig N Lumb, Boguslaw Obara, Judith P Armitage, and Richard M Berry. Flagellar hook flexibility is essential for bundle formation in swimming escherichia coli cells. *Journal of bacteriology*, 194(13):3495–3501, 2012.

[29] Yuko Mimori, Ichiro Yamashita, Kazuyoshi Murata, Yoshinori Fujiyoshi, Koji Yonekura, Chikashi Toyoshima, and Keiichi Namba. The structure of the r-type straight flagellar filament ofsalmonellaat 9 å resolution by electron cryomicroscopy. *Journal of molecular biology*, 249(1):69–87, 1995.

[30] David Gene Morgan, Cameron Owen, Linda A Melanson, and David J DeRosier. Structure of bacterial flagellar filaments at 11 å resolution: packing of the α-helices. *Journal of molecular biology*, 249(1):88–110, 1995.

[31] CR Calldine. Change of waveform in bacterial flagella: the role of mechanics at the molecular level. *Journal of molecular biology*, 118(4):457–479, 1978.

[32] Keiichi Namba and Ferenc Vonderviszt. Molecular architecture of bacterial flagellum. *Quarterly reviews of biophysics*, 30(1):1–65, 1997.

[33] Kazuya Hasegawa, Hirofumi Suzuki, Ferenc Vonderviszt, Yuko Mimori-Kiyosue, Keiichi Namba, et al. Structure and switching of bacterial flagellar filaments studied by x-ray fiber diffraction. *Nature structural biology*, 5(2):125, 1998.

[34] Eric Lauga. Bacterial hydrodynamics. *Annual Review of Fluid Mechanics*, 48:105–130, 2016.

[35] Ritsu Kamiya, Sho Asakura, katsuzo Wakabayashi, and Keiichi Namba. Transition of bacterial flagella from helical to straight forms with different subunit arrangements. *Journal of molecular biology*, 131(4):725–742, 1979.

[36] Srikanth V Srigiriraju and Thomas R Powers. Model for polymorphic transitions in bacterial flagella. *Physical Review E*, 73(1):011902, 2006.

[37] Linda Turner, William S Ryu, and Howard C Berg. Real-time imaging of fluorescent flagellar filaments. *Journal of bacteriology*, 182(10):2793–2801, 2000.

[38] Judith P Armitage, Thomas P Pitta, Margot A-S Vigeant, Helen L Packer, and Roseanne M Ford. Transformations in flagellar structure of rhodobacter sphaeroides and possible relationship to changes in swimming speed. *Journal of Bacteriology*, 181(16):4825–4833, 1999.

[39] Deepan SH Shah, Tania Perehinec, Susan M Stevens, Shin-Ichi Aizawa, and R Elizabeth Sockett. The flagellar filament of rhodobacter sphaeroides: ph-induced polymorphic transitions and analysis of the flic gene. *Journal of bacteriology*, 182(18):5218–5224, 2000.

[40] Yoshiyuki Sowa and Richard M Berry. Bacterial flagellar motor. *Quarterly reviews of biophysics*, 41(2):103–132, 2008.

[41] Steven M Block and Howard C Berg. Successive incorporation of force-generating units in the bacterial rotary motor. *Nature*, 309(5967):470, 1984.

[42] Stuart W Reid, Mark C Leake, Jennifer H Chandler, Chien-Jung Lo, Judith P Armitage, and Richard M Berry. The maximum number of torque-generating units in the flagellar motor of escherichia coli is at least 11. *Proceedings of the National Academy of Sciences*, 103(21):8066–8071, 2006.

[43] Mark C Leake, Jennifer H Chandler, George H Wadhams, Fan Bai, Richard M Berry, and Judith P Armitage. Stoichiometry and turnover in single, functioning membrane protein complexes. *Nature*, 443(7109):355, 2006.

[44] Hajime Fukuoka, Tomoyuki Wada, Seiji Kojima, Akihiko Ishijima, and Michio Homma. Sodium-dependent dynamic assembly of membrane complexes in sodium-driven flagellar motors. *Molecular microbiology*, 71(4):825–835, 2009.

[45] Anja Paulick, Andrea Koerdt, Jürgen Lassak, Stuart Huntley, Ina Wilms, Franz Narberhaus, and Kai M Thormann. Two different stator systems drive a single polar flagellum in shewanella oneidensis mr-1. *Molecular microbiology*, 71(4):836–850, 2009.

[46] Pushkar P Lele, Basarab G Hosu, and Howard C Berg. Dynamics of mechanosensing in the bacterial flagellar motor. *Proceedings of the National Academy of Sciences*, 110(29):11839–11844, 2013.

[47] Murray J Tipping, Nicolas J Delalez, Ren Lim, Richard M Berry, and Judith P Armitage. Load-dependent assembly of the bacterial flagellar motor. *MBio*, 4(4):e00551–13, 2013.

[48] Yong-Suk Che, Shuichi Nakamura, Yusuke V Morimoto, Nobunori Kami-ike, Keiichi Namba, and Tohru Minamino. Load-sensitive coupling of proton translocation and torque generation in the bacterial flagellar motor. *Molecular microbiology*, 91(1):175–184, 2014.

[49] Jianhua Xing, Fan Bai, Richard Berry, and George Oster. Torque–speed relationship of the bacterial flagellar motor. *Proceedings of the National Academy of Sciences*, 103(5):1260–1265, 2006.

[50] Howard C Berg and Linda Turner. Torque generated by the flagellar motor of escherichia coli. *Biophysical journal*, 65(5):2201–2216, 1993.

[51] Richard M Berry and Howard C Berg. Absence of a barrier to backwards rotation of the bacterial flagellar motor demonstrated with optical tweezers. *Proceedings of the National Academy of Sciences*, 94(26):14433–14437, 1997.

[52] Richard M Berry and Howard C Berg. Torque generated by the flagellar motor of escherichia coli while driven backward. *Biophysical Journal*, 76(1):580–587, 1999.

[53] Xiaobing Chen and Howard C Berg. Solvent-isotope and ph effects on flagellar rotation in escherichia coli. *Biophysical journal*, 78(5):2280–2284, 2000.

[54] Yoshiyuki Sowa, Hiroyuki Hotta, Michio Homma, and Akihiko Ishijima. Torque–speed relationship of the na+-driven flagellar motor of vibrio alginolyticus. *Journal of molecular biology*, 327(5):1043–1051, 2003.

[55] Yuichi Inoue, Chien-Jung Lo, Hajime Fukuoka, Hiroto Takahashi, Yoshiyuki Sowa, Teuta Pilizota, George H Wadhams, Michio Homma, Richard M Berry, and Akihiko Ishijima. Torque–speed relationships of na+-driven chimeric flagellar motors in escherichia coli. *Journal of molecular biology*, 376(5):1251–1259, 2008.

[56] Guanglai Li and Jay X Tang. Low flagellar motor torque and high swimming efficiency of caulobacter crescentus swarmer cells. *Biophysical journal*, 91(7):2726–2734, 2006.

[57] Junhua Yuan, Karen A Fahrner, Linda Turner, and Howard C Berg. Asymmetry in the clockwise and counterclockwise rotation of the bacterial flagellar motor. *Proceedings of the National Academy of Sciences*, 107(29):12846–12849, 2010.

[58] Edward M Purcell. Life at low reynolds number. *American journal of physics*, 45(1):3–11, 1977.

[59] Netta Cohen and Jordan H Boyle. Swimming at low reynolds number: a beginners guide to undulatory locomotion. *Contemporary Physics*, 51(2):103–123, 2010.

[60] Eric Lauga. Life around the scallop theorem. *Soft Matter*, 7(7):3060–3065, 2011.

[61] Eric Lauga and Thomas R Powers. The hydrodynamics of swimming microorganisms. *Reports on Progress in Physics*, 72(9):096601, 2009.

[62] GJ Hancock. The self-propulsion of microscopic organisms through liquids. *Proceedings of the Royal Society of London. Series A. Mathematical and Physical Sciences*, 217(1128):96–121, 1953.

[63] Martin Li. *Experimental study of swimming flagellated bacteria and their collective behaviour in concentrated suspensions*. PhD thesis, The University of Edinburgh, 2010.

[64] Eric Lauga, Willow R DiLuzio, George M Whitesides, and Howard A Stone. Swimming in circles: motion of bacteria near solid boundaries. *Biophysical journal*, 90(2):400–412, 2006.

[65] Howard C Berg and Linda Turner. Chemotaxis of bacteria in glass capillary arrays. escherichia coli, motility, microchannel plate, and light scattering. *Biophysical Journal*, 58(4):919–930, 1990.

[66] Paul D Frymier, Roseanne M Ford, Howard C Berg, and Peter T Cummings. Three-dimensional tracking of motile bacteria near a solid planar surface. *Proceedings of the National Academy of Sciences*, 92(13):6195–6199, 1995.

[67] Robert Brown. Xxvii. a brief account of microscopical observations made in the months of june, july and august 1827, on the particles contained in the pollen of plants; and on the general existence of active molecules in organic and inorganic bodies. *The Philosophical Magazine*, 4(21):161–173, 1828.

[68] Albert Einstein et al. On the motion of small particles suspended in liquids at rest required by the molecular-kinetic theory of heat. *Annalen der physik*, 17:549–560, 1905.

[69] Marian Von Smoluchowski. Zur kinetischen theorie der brownschen molekularbewegung und der suspensionen. *Annalen der physik*, 326(14):756–780, 1906.

[70] Paul Langevin. Sur la théorie du mouvement brownien. *Compt. Rendus*, 146:530–533, 1908.

[71] Agnese Callegari and Giovanni Volpe. Numerical simulations of active brownian particles. In *Flowing Matter*, pages 211–238. Springer, 2019.

[72] Hong Qian, Michael P Sheetz, and Elliot L Elson. Single particle tracking. analysis of diffusion and flow in two-dimensional systems. *Biophysical journal*, 60(4):910–921, 1991.

[73] Gerald L Hazelbauer, Joseph J Falke, and John S Parkinson. Bacterial chemoreceptors: high-performance signaling in networked arrays. *Trends in biochemical sciences*, 33(1):9–19, 2008.

[74] Samuel E Tusk, Nicolas J Delalez, and Richard M Berry. Subunit exchange in protein complexes. *Journal of molecular biology*, 2018.

[75] Howard C Berg and Douglas A Brown. Chemotaxis in escherichia coli analysed by three-dimensional tracking. *Nature*, 239(5374):500, 1972.

[76] Robert M Macnab and DE Koshland. The gradient-sensing mechanism in bacterial chemotaxis. *Proceedings of the National Academy of Sciences*, 69(9):2509–2512, 1972.

[77] Nikita Vladimirov and Victor Sourjik. Chemotaxis: how bacteria use memory. *Biological chemistry*, 390(11):1097–1104, 2009.

[78] Jeffery E Segall, Steven M Block, and Howard C Berg. Temporal comparisons in bacterial chemotaxis. *Proceedings of the National Academy of Sciences*, 83(23):8987–8991, 1986.

[79] Antonio Celani and Massimo Vergassola. Bacterial strategies for chemotaxis response. *Proceedings of the National Academy of Sciences*, 107(4):1391–1396, 2010.

[80] David B Dusenbery and Terry W Snell. A critical body size for use of pheromones in mate location. *Journal of chemical ecology*, 21(4):427–438, 1995.

[81] Howard C Berg and Edward M Purcell. Physics of chemoreception. *Biophysical journal*, 20(2):193–219, 1977.

[82] George A Jackson. Simulating chemosensory responses of marine microorganisms1. *Limnology and oceanography*, 32(6):1253–1266, 1987.

[83] Damon A Clark and Lars C Grant. The bacterial chemotactic response reflects a compromise between transient and steady-state behavior. *Proceedings of the National Academy of Sciences*, 102(26):9150–9155, 2005.

[84] Yevgeniy V Kalinin, Lili Jiang, Yuhai Tu, and Mingming Wu. Logarithmic sensing in escherichia coli bacterial chemotaxis. *Biophysical journal*, 96(6):2439–2448, 2009.

[85] Janos Tobias Locsei. Persistence of direction increases the drift velocity of run and tumble chemotaxis. *Journal of mathematical biology*, 55(1):41–60, 2007.

[86] Chuan Xue and Hans G Othmer. Multiscale models of taxis-driven patterning in bacterial populations. *SIAM journal on applied mathematics*, 70(1):133–167, 2009.

[87] George O'Toole, Heidi B Kaplan, and Roberto Kolter. Biofilm formation as microbial development. *Annual Reviews in Microbiology*, 54(1):49–79, 2000.

[88] Russell D Monds and George A O'Toole. The developmental model of microbial biofilms: ten years of a paradigm up for review. *Trends in microbiology*, 17(2):73–87, 2009.

[89] TR De Kievit. Quorum sensing in pseudomonas aeruginosa biofilms. *Environmental microbiology*, 11(2):279–288, 2009.

[90] Bonnie L Bassler and Richard Losick. Bacterially speaking. *Cell*, 125(2):237–246, 2006.

[91] Wai-Leung Ng and Bonnie L Bassler. Bacterial quorum-sensing network architectures. *Annual review of genetics*, 43:197–222, 2009.

[92] Kai Papenfort and Bonnie L Bassler. Quorum sensing signal–response systems in gram-negative bacteria. *Nature Reviews Microbiology*, 14(9):576, 2016.

[93] Tamás Vicsek and Anna Zafeiris. Collective motion. *Physics reports*, 517(3-4):71–140, 2012.

[94] Luis H Cisneros, Ricardo Cortez, Christopher Dombrowski, Raymond E Goldstein, and John O Kessler. Fluid dynamics of self-propelled microorganisms, from individuals to concentrated populations. In *Animal Locomotion*, pages 99–115. Springer, 2010.

[95] Peter Grunwald. *Industrial biocatalysis*. Pan Stanford, 2014.

[96] Matthias Theves, Johannes Taktikos, Vasily Zaburdaev, Holger Stark, and Carsten Beta. Random walk patterns of a soil bacterium in open and confined environments. *EPL (Europhysics Letters)*, 109(2):28007, 2015.

[97] Michael Raatz, Marius Hintsche, Marco Bahrs, Matthias Theves, and Carsten Beta. Swimming patterns of a polarly flagellated bacterium in environments of increasing complexity. *The European Physical Journal Special Topics*, 224(7):1185–1198, 2015.

[98] Marius Hintsche. *Locomotion of a bacterium with a polar bundle of flagella*. PhD thesis, Universität Potsdam, 2019.

[99] J.N. Kapur, P.K. Sahoo, and A.K.C Wong. A new method for gray-level picture thresholding using the entropy of the histogram. *Comput. Vis. Graph.*, 29:273–285, 1985.

[100] John C Crocker and David G Grier. Methods of digital video microscopy for colloidal studies. *J. Coll. Interfat. Sci.*, 179(1):298–310, 1996.

[101] Gabriel Rosser, Alexander G Fletcher, David A Wilkinson, Jennifer A de Beyer, Christian A Yates, Judith P Armitage, Philip K Maini, and Ruth E Baker. Novel methods for analysing bacterial tracks reveal persistence in rhodobacter sphaeroides. *PLoS computational biology*, 9(10):e1003276, 2013.

[102] Jean-Baptiste Masson, Guillaume Voisinne, Jerome Wong-Ng, Antonio Celani, and Massimo Vergassola. Noninvasive inference of the molecular chemotactic response using bacterial trajectories. *PNAS*, 109(5):1802–1807, 2012.

[103] Abraham Savitzky and Marcel JE Golay. Smoothing and differentiation of data by simplified least squares procedures. *Anal. Chem.*, 36(8):1627–1639, 1964.

[104] Zahra Alirezaeizanjani, Robert Großmann, Veronika Pfeifer, Marius Hintsche, and Carsten Beta. Chemotaxis strategies of bacteria with multiple run modes. *Science Advances*, 6(22):eaaz6153, 2020.

[105] Eugeni Belda, Ruben GA Van Heck, Maria José Lopez-Sanchez, Stéphane Cruveiller, Valérie Barbe, Claire Fraser, Hans-Peter Klenk, Jörn Petersen, Anne Morgat, Pablo I Nikel, et al. The revisited genome of pseudomonas putida KT2440 enlightens its value as a robust metabolic chassis. *Environ. Microbiol.*, 18(10):3403–3424, 2016.

[106] Robert M Macnab. Bacterial flagella rotating in bundles: a study in helical geometry. *Proceedings of the National Academy of Sciences*, 74(1):221–225, 1977.

[107] MunJu Kim, James C Bird, Annemarie J Van Parys, Kenneth S Breuer, and Thomas R Powers. A macroscopic scale model of bacterial flagellar bundling. *Proceedings of the National Academy of Sciences*, 100(26):15481–15485, 2003.

[108] Timothy B Doyle, Andrew C Hawkins, and Linda L McCarter. The complex flagellar torque generator of pseudomonas aeruginosa. *Journal of bacteriology*, 186(19):6341–6350, 2004.

[109] Anton Hartmann, Michael Schmid, Diederik Van Tuinen, and Gabriele Berg. Plant-driven selection of microbes. *Plant and Soil*, 321(1-2):235–257, 2009.

[110] Guanglai Li, Lick-Kong Tam, and Jay X Tang. Amplified effect of brownian motion in bacterial near-surface swimming. *Proceedings of the National Academy of Sciences*, 105(47):18355–18359, 2008.

[111] Mehdi Molaei, Michael Barry, Roman Stocker, and Jian Sheng. Failed escape: solid surfaces prevent tumbling of escherichia coli. *Physical review letters*, 113(6):068103, 2014.

[112] Yukio Magariyama, Shin-ya Masuda, Yasunari Takano, Toshio Ohtani, and Seishi Kudo. Difference between forward and backward swimming speeds of the single polar-flagellated bacterium, vibrio alginolyticus. *FEMS microbiology letters*, 205(2):343–347, 2001.

[113] Seishi Kudo, Norio Imai, Megumi Nishitoba, Shigeru Sugiyama, and Yukio Magariyama. Asymmetric swimming pattern of vibrio alginolyticus cells with single polar flagella. *FEMS microbiology letters*, 242(2):221–225, 2005.

[114] Tomonobu Goto, Kousou Nakata, Kensaku Baba, Masaharu Nishimura, and Yukio Magariyama. A fluid-dynamic interpretation of the asymmetric motion of singly flagellated bacteria swimming close to a boundary. *Biophysical journal*, 89(6):3771–3779, 2005.

[115] Silvio Bianchi, Filippo Saglimbeni, and Roberto Di Leonardo. Holographic imaging reveals the mechanism of wall entrapment in swimming bacteria. *Physical Review X*, 7(1):011010, 2017.

[116] Silvio Bianchi, Filippo Saglimbeni, Giacomo Frangipane, Dario Dell'Arciprete, and Roberto Di Leonardo. 3d dynamics of bacteria wall entrapment at a water–air interface. *Soft matter*, 15(16):3397–3406, 2019.

[117] μ-plate 96 well black. https://ibidi.com/multiwell-plates/21-plate-96-well.html. Accessed:2019-06-04.

[118] Stanislav Burov, SM Ali Tabei, Toan Huynh, Michael P Murrell, Louis H Philipson, Stuart A Rice, Margaret L Gardel, Norbert F Scherer, and Aaron R Dinner. Distribution of directional change as a signature of complex dynamics. *Proceedings of the National Academy of Sciences*, 110(49):19689–19694, 2013.

[119] Ikuro Kawagishi, Miho Imagawa, Yasuo Imae, Linda McCarter, and Michio Homma. The sodium-driven polar flagellar motor of marine vibrio as the mechanosensor that regulates lateral flagellar expression. *Molecular microbiology*, 20(4):693–699, 1996.

[120] Pamela Zengel, Anna Nguyen-Hoang, Christoph Schildhammer, Roman Zantl, Valentin Kahl, and Elias Horn. μ-slide chemotaxis: a new chamber for long-term chemotaxis studies. *BMC Cell Biol.*, 12(1):21, 2011.

[121] Maximilian Seyrich, Zahra Alirezaeizanjani, Carsten Beta, and Holger Stark. Statistical parameter inference of bacterial swimming strategies. *New Journal of Physics*, 20(10):103033, 2018.

[122] C Van Den Broeck. On the relation between white shot noise, gaussian white noise, and the dichotomic markov process. *Journal of Statistical Physics*, 31(3):467–483, 1983.

[123] Jessica Strefler, Werner Ebeling, Ewa Gudowska-Nowak, and Lutz Schimansky-Geier. Dynamics of individuals and swarms with shot noise induced by stochastic food supply. *The European Physical Journal B*, 72(4):597, 2009.

[124] Jonathan Saragosti, Vincent Calvez, Nikolaos Bournaveas, Benoıt Perthame, Axel Buguin, and Pascal Silberzan. Directional persistence of chemotactic bacteria in a traveling concentration wave. *PNAS*, 108(39):16235–16240, 2011.

[125] Oliver Pohl, Marius Hintsche, Zahra Alirezaeizanjani, Maximilian Seyrich, Carsten Beta, and Holger Stark. Inferring the chemotactic strategy of p. putida and e. coli using modified kramers-moyal coefficients. *PLoS Comput. Biol.*, 13(1):e1005329, 2017.

[126] Bradley Efron and Robert J Tibshirani. *An introduction to the bootstrap*. Chapman and Hall/CRC, 1994.

[127] Yehuda Vardi. Nonparametric estimation in renewal processes. *Ann. Statist.*, 10(3):772–785, 09 1982.

[128] Evelyn F Keller and Lee A Segel. Model for chemotaxis. *J. Theor. Biol.*, 30(2):225–234, 1971.

[129] Amin Omar, J Barry Wright, Gregory Schultz, Robert Burrell, and Patricia Nadworny. Microbial biofilms and chronic wounds. *Microorganisms*, 5(1):9, 2017.

[130] Hyun Koo, Raymond N Allan, Robert P Howlin, Paul Stoodley, and Luanne Hall-Stoodley. Targeting microbial biofilms: current and prospective therapeutic strategies. *Nature Reviews Microbiology*, 15(12):740, 2017.

[131] Merle E Olson, Howard Ceri, Douglas W Morck, Andre G Buret, and Ronald R Read. Biofilm bacteria: formation and comparative susceptibility to antibiotics. *Canadian journal of veterinary research*, 66(2):86, 2002.

[132] Hera Vlamakis, Claudio Aguilar, Richard Losick, and Roberto Kolter. Control of cell fate by the formation of an architecturally complex bacterial community. *Genes & development*, 22(7):945–953, 2008.

[133] Haoran Xu, Justas Dauparas, Debasish Das, Eric Lauga, and Yilin Wu. Self-organization of swimmers drives long-range fluid transport in bacterial colonies. *Nature communications*, 10(1):1792, 2019.

[134] Manuel Espinosa-Urgel and Juan-Luis Ramos. Cell density-dependent gene contributes to efficient seed colonization by pseudomonas putida kt2440. *Appl. Environ. Microbiol.*, 70(9):5190–5198, 2004.

[135] Christopher Dombrowski, Luis Cisneros, Sunita Chatkaew, Raymond E Goldstein, and John O Kessler. Self-concentration and large-scale coherence in bacterial dynamics. *Physical review letters*, 93(9):098103, 2004.

[136] Julius Adler. Chemotaxis in bacteria. *Science*, 153(3737):708–716, 1966.

[137] Remy Colin, Knut Drescher, and Victor Sourjik. Chemotactic behaviour of escherichia coli at high cell density. *Nature communications*, 10(1):1–11, 2019.

[138] Xie Chang-Li, Tang Hou-Kuhan, Song Zhau-Hua, Qu Song-Sheng, Liao Yao-Ting, and Liu Hai-Shui. Microcalorimetric study of bacterial growth. *Thermochimica Acta*, 123:33–41, 1988.

[139] μ-slide VI$^{0.1}$. https://ibidi.com/channel-slides/56–slide-vi-01.html. Accessed:2019-12-26.

[140] Younan Xia and George M Whitesides. Soft lithography. *Annual review of materials science*, 28(1):153–184, 1998.

[141] Matthias Theves. *Bacterial motility and growth in open and confined environments*. PhD thesis, Universität Potsdam, 2013.

[142] Lázaro Molina, Cayo Ramos, Estrella Duque, M Carmen Ronchel, Juan M García, Lene Wyke, and Juan L Ramos. Survival of pseudomonas putida kt2440 in soil and in the rhizosphere of plants under greenhouse and environmental conditions. *Soil Biology and Biochemistry*, 32(3):315–321, 2000.

[143] Christopher M Bishop et al. *Neural networks for pattern recognition*. Oxford university press, 1995.

[144] Ruggero La Rosa, Volker Behrends, Huw D Williams, Jacob G Bundy, and Fernando Rojo. Influence of the c rc regulator on the hierarchical use of carbon sources from a complete medium in p seudomonas. *Environmental microbiology*, 18(3):807–818, 2016.

[145] Maximilian Seyrich, Andrzej Palugniok, and Holger Stark. Traveling concentration pulses of bacteria in a generalized keller–segel model. *New Journal of Physics*, 21(10):103001, 2019.

[146] Edward L Kaplan and Paul Meier. Nonparametric estimation from incomplete observations. *Journal of the American statistical association*, 53(282):457–481, 1958.

[147] Richard A Redner and Homer F Walker. Mixture densities, maximum likelihood and the em algorithm. *SIAM review*, 26(2):195–239, 1984.